The Fluid Provenance and Ore Mineralisation History of the Ecton Copper Mine, Central England

Ryan Harris

Thesis submitted to the University of Ottawa
in partial fulfillment of the requirements for the
Master of Science in Earth Sciences

Department of Earth and Environmental Sciences
Faculty of Science
University of Ottawa

Abstract

Mississippi-Valley type (MVT) ore deposits are significant global sources of lead and zinc. These deposits are the result of relatively low temperature hydrothermal fluids precipitating ore minerals in cavities and veins, typically occurring in regionally-significant ore districts that contain multiple deposits (*e.g*. Pine Point, Canada; Irish Midlands, Ireland; and Viburnum Trend, USA). The MVT deposits of the South Pennine orefield, central England, are historically important, producing large amounts of lead, zinc, and fluoride, predominantly during the 19th and 20th centuries. Located in this orefield is Ecton Mine, with an extensive history of mining dating back to the Bronze Age. Between 1760 and 1820; the Deep Ecton mine produced over 100,000 tonnes of copper ore before its eventual closure and flooding. The copper ore, mainly chalcopyrite, formed in vertical cylindrical pipes, cross-cutting bedding in the host carbonates. Within the South Pennine orefield, the high abundance of copper makes Ecton anomalous. Many aspects of Ecton mineralization (such as fluid composition, emplacement temperature, and structural controls) remain unclear, particularly within the context of other deposits in the South Pennine orefield. Research on Ecton ore genesis is made difficult by a lack of useful study material; resources were totally exhausted and the site is formally recognized, and protected, as a historical landmark.

Working with samples from the Deep Ecton mine, obtained through various museum collections, petrographic, cathodoluminescence, SEM/EPMA, LA-ICP-MS, and sulfur isotope data are used to characterize the fluid provenance and mineralization processes leading to the formation of the Ecton orebody. Analysis of trace elements in calcite reveals that the mineralisation at Ecton was the result of a fluid mixing event, likely between a seawater-derived fluid and a metal-bearing hydrothermal fluid. The sulfur isotope data from this study (avg. -15.9‰) overlap with previously reported values for the South Pennine Orefield, and bacterial sulfate reduction is proposed as the mechanism of sulfur derivation. The samples also contain Ni-rich minerals like gersdorffite, and relatively Ni-rich pyrite (up to 17.5 wt.%), and element mapping shows chemical zoning of Cu, Ni and Co in single crystals of marcasite. These observations demonstrate that the mineralising fluid at Ecton, and possibly the South Pennine Orefield, was enriched in elements not found in abundance in typical MVT deposits. This study also finds that Ecton has characteristics that are comparable to Irish-type deposits (*e.g.* Cu-As-Ni-Co mineral assemblages, and structural controls), which challenges the classification of Ecton as a classic MVT deposit.

Table of Contents

Abstract ii
Acknowledgements iv
1. Introduction 1
2. Regional Geology 2
2.1 The South Pennine Orefield 3
2.2 Ecton Geology 7
3. Sample Descriptions 10
3.1 Optical Microscopy 12
4. Analytical Techniques 17
5. Results 19
5.1 Element Mapping and Backscatter Electron Imaging 19
5.2 Cathodoluminescence 22
5.3 Major Element Chemistry 23
5.4 Trace Element Chemistry 24
5.5 Sulfur Isotopes 30
6. Discussion 31
6.1 Geochemical characteristics of the Ecton mineralisation 31
6.2 Fluid mechanisms and provenance 37
6.3 Linking Localized Evidence to Large-Scale Processes 47
7. Conclusion 54
8. References 56
Appendix 65

Acknowledgements

Funding for this thesis was provided by the Canadian Museum of Nature, Mineral Sciences Division.

Firstly, I would like to thank my thesis supervisors, Brian O'Driscoll and Aaron Lussier, for their guidance and support throughout the progression of this thesis.

Thank you to Linsey Loughtman at the Manchester Museum for facilitating the provision and delivery of two samples used in this study, as well as Michael Bainbridge, Curator of Minerals at the Canadian Museum of Nature, for assistance with accessing the CMNMC sample used in this study. I would also like to thank Alain Mauviel for his assistance with preparing thin sections, and Glenn Poirier for his support in collecting EPMA data. Thank you also to Sam Morfin (uOttawa) and Dany Savard (LabMater) for their help in LA-ICP-MS data acquisition.

Finally, thank you to my family, friends, and partner for support throughout my entire academic career.

1. Introduction

Mississippi Valley-Type (MVT) deposits are a globally significant source of lead and zinc, with sediment-hosted Pb-Zn deposits having an estimated global mineral resource of 141 Mt (53% of global resources) of lead and 345 Mt (57% of global resources) (Mudd *et al.*, 2017). MVT deposits are typically epigenetic and hosted in carbonate platforms located in the foreland of orogenic belts (Wilkinson, 2014). Platforms that host MVT deposits are infiltrated by relatively low temperature (75° - 200°) hydrothermal fluids, derived from sedimentary brines, precipitating ore minerals like sphalerite and galena in cavities and veins (Leach *et al.*, 2010). Individual MVT deposits commonly occur in large quantities together and these groupings are known as districts, and can cover hundreds of square kilometers (e.g., Pine Point, Canada, Rhodes *et al.*, 1984; Irish Midlands, Ireland, Hitzman and Beaty, 1996; Upper Mississippi Valley, USA, Heyl *et al.*, 1959; Upper Silesia, Poland, Heijlen *et al.*, 2003). The characteristics of MVT deposits were extensively outlined by Leach *et al.* (2005) and are classified to a first order on the basis of tectonic setting, host rocks and timing of mineralization. However, many deposits exhibit nuances that have resulted in classification as sub-types or transitional deposits, e.g., sandstone-lead deposits (Bjørlykke and Sangster, 1981), distal Pb-Zn skarns (Samson *et al.*, 2008), Irish-type deposits (Russell, 1986), and fracture controlled Pb-Zn and fluorite-baryte deposits (Partey *et al.*, 2009).

The MVT deposits within the South Pennine Orefield, central England, are historically (Bronze Age – 1940) important locations for lead, zinc and fluorite mining (Ford and Quirk, 1995; Ford, 2000; Ford and Worley, 2016). The estimated production from the orefield was between 4 and 6 million tonnes of lead, with much of it being produced from Millclose Mine on the east side of the orefield until the mines closure in 1940 (Ford and Worley, 2016). The mineral veins are hosted within lower Carboniferous limestones and dolomites, and the carbonate sequences are commonly interbedded with layers of basalt flows and thin tuff units (Ford and Quirk, 1995). The limestones in the platform are folded, resulting from compressional forces exerted during the mid-Paleozoic Variscan Orogeny (Ford, 2000). These folds are primarily oriented E-W throughout the region, although N-S folds occur less commonly. The English Pennines (North Pennine Orefield and South Pennine Orefield) have long been classified as fluorite-type MVT deposits (Dunham, 1983*;* Leach *et al.*, 2010), but recent studies (Kraemer *et al.* 2019*;* Dempsey *et al.*, 2021) on the North Pennine Orefield have suggested that the Pb-Zn-Cu-F mineralisation is the result of a magmatic hydrothermal fluid and that the classification for other Pb-Zn districts worldwide could also be incorrect.

Located in the southwest of the South Pennine Orefield is Ecton Hill; a locality with multiple historic copper mines, predominantly worked during the 18th century, but with evidence

of mining during the bronze age or older (Timberlake, 2014). The largest mine, Deep Ecton, produced 100,000 tonnes of copper between 1760 and 1820 before the resource was exhausted and the mine was flooded after the pumping engines were turned off (Ford, 2000). The copper ore consists mostly of chalcopyrite that was precipitated in vertical pipes that crosscut the folded limestone bedding and that are roughly aligned with the direction of the Ecton anticline (Ford, 2000). Ecton is the only location in the South Pennine Orefield with significant amounts of copper and many questions about the petrogenesis of the deposit still remain. Due to the difficulty of accessing the pipe mineralisation, the structural controls that led to the emplacement of brecciated pipes of copper ore have been difficult to establish. Suggestions for the source of the fluid that formed Ecton have been made, namely from the Cheshire Basin to the west (Mostaghel and Ford, 1986*;* Masheder and Rankin, 1988), based on the sediment-hosted stratiform copper deposits that occur there, but little research has been done since the latter studies to substantiate this. Other questions that have not been thoroughly addressed include, the emplacement temperature of the mineralisation, and the contrast in mineralisation style and metal content compared to the rest of the South Pennine Orefield.

Through the use of petrographic observations, and analyses including cathodoluminescence, electron probe micro-analyzer (EPMA) and laser ablation-inductively coupled plasma-mass spectrometry (LA-ICP-MS) mineral chemistry, and sulfur isotopes, this study aims to characterize the mineralisation present at Ecton and provide insight into the formation of the regionally unique ore deposit and its relationship with the greater Pb-Zn mineralisation throughout the South Pennine Orefield. Element mapping of the sulfide minerals and trace element data of the host calcite reveals complex local fluid mechanisms and evidence of fluid mixing, while sulfur isotopes show a consistent overlap with the values of the sulfides throughout the rest of the orefield. This localized evidence is used to suggest genetic relationships with the regional mineralisation, as well as compare Ecton to Irish-type deposits, of which have similar mineral assemblages, structural controls, and enrichment of elements like Cu, Ni, Co and As.

2. Regional Geology

During the Carboniferous Period, Central and Northern England underwent back-arc extension, north of the developing Variscan subduction front. Located between the Southern Uplands Terrane of Scotland and the Wales – Brabant High, the Pennine Basin was a major rift province dominated by marine basins and carbonate platforms (Corfield *et al.*, 1996). Variscan inversion tectonics occurred in the Moscovian (315 – 307 Ma) when the tectonic regime changed from extensional to compressional, resulting in thrust faults throughout the foreland basin. This also resulted in uplift and erosion of the foreland (Corfield *et al.*, 1996).

2.1 The South Pennine Orefield

The South Pennine Orefield (**Fig. 1**) is a carbonate platform, occupying an area of approximately 200 km^2. It is composed of Visean stage (346.7 – 330.3 Ma) limestones, collectively known as the Peak Limestone Group (Ford and Worley, 2016), mostly located in Derbyshire, and partly in Staffordshire to the southwest.

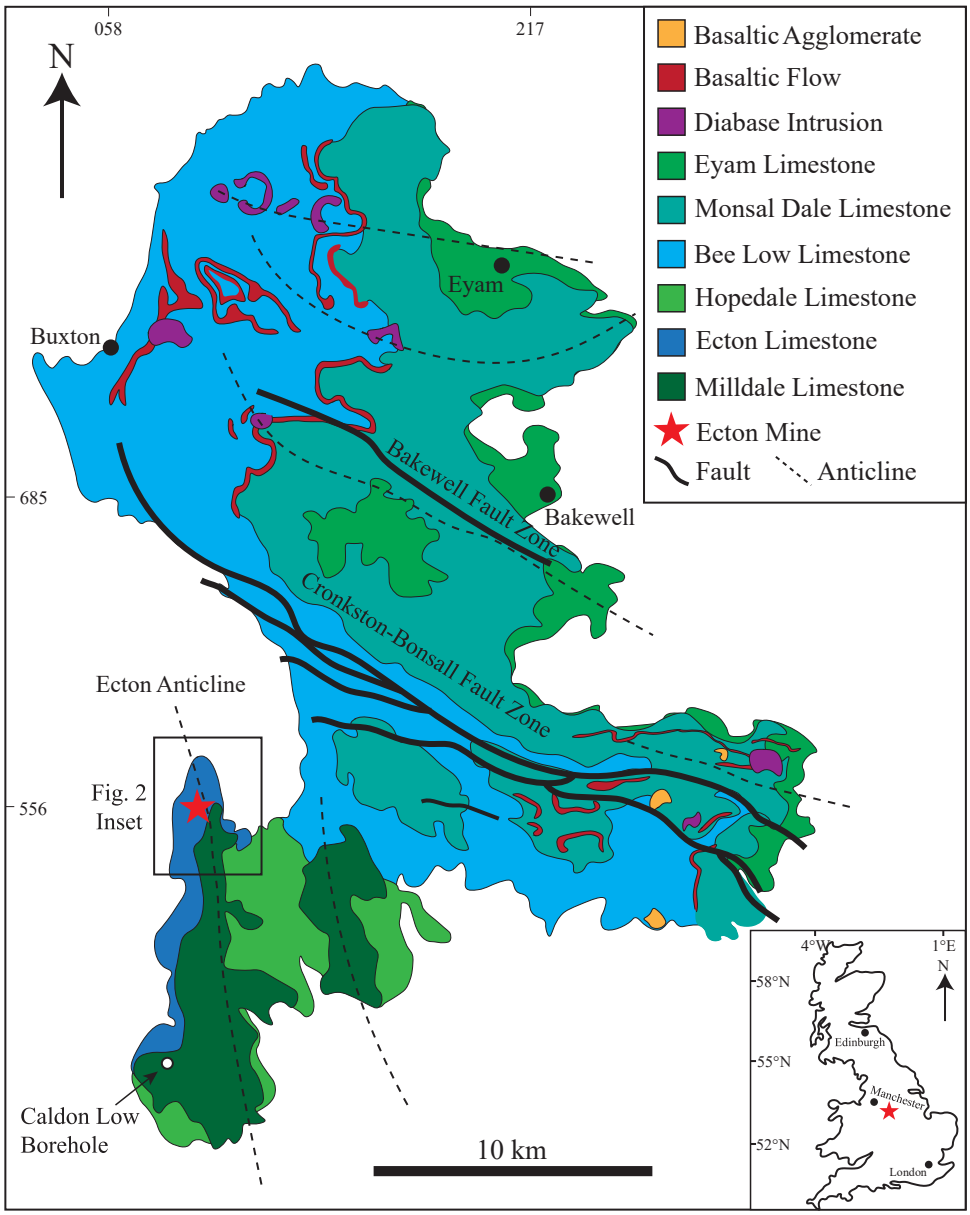

Figure 1: Geological map of the South Pennine Orefield. Based on *Ford and Worley, 2016; Quirk, 1987.* Legend in stratigraphic order. Grid numbers apply to British National Grid square SK.

Stratigraphy

The South Pennine Orefield is located on a geologic structure referred to as the Derbyshire Dome, consisting of two shallow water carbonate platforms, the Derbyshire Platform and the Staffordshire Platform (**Fig. 2A, C**). These two platforms are separated by the Widmerpool Gulf, a narrow carbonate ramp half-graben (Aitkenhead *et al.*, 2002).

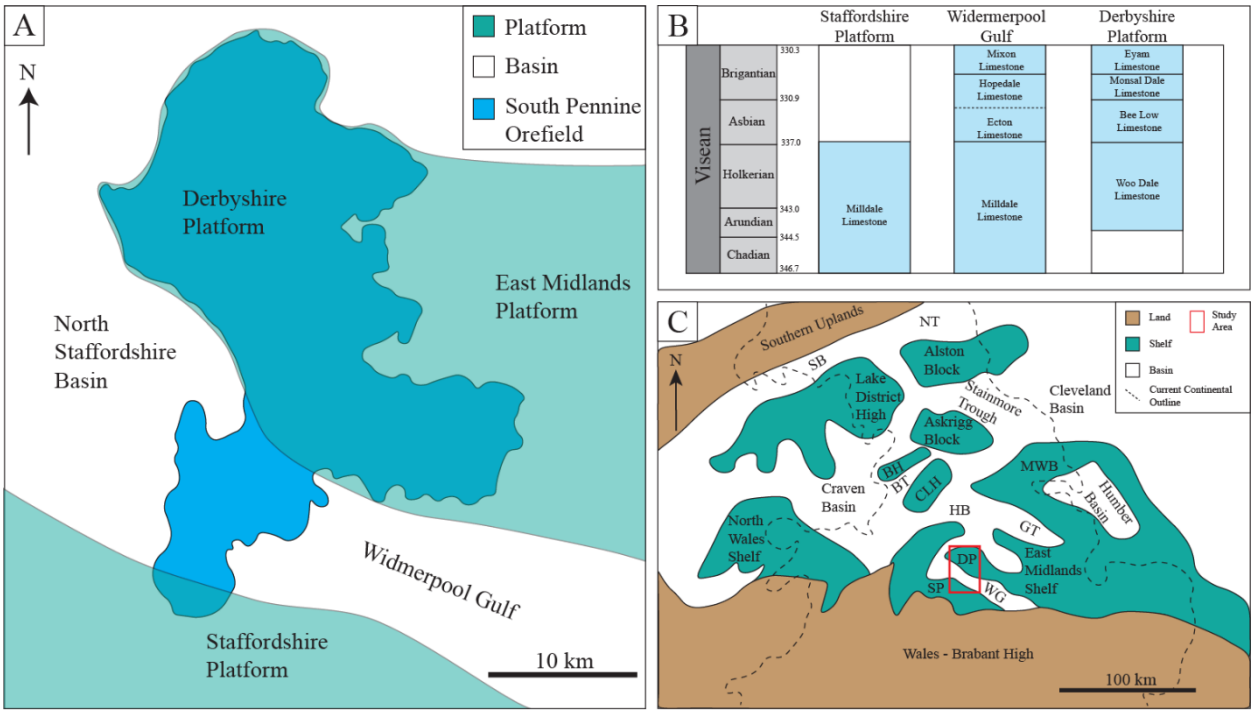

Figure 2: *(A)* Tectonostratigraphy of the South Pennine Orefield. Based on *Aitkenhead et al., 2002*. *(B)* Summary of stratigraphy of the Staffordshire Platform, Widmerpool Gulf, and Derbyshire Platform. Based on *Aitkenhead et al., 2002*. *(C)* Tectonostratigraphy of Carboniferous central England with outline of current coastline. BH – Bowland High; BT – Bowland Trough; CLH – Central Lancashire High; DP – Derbyshire Platform; GT – Gainsborough Trough; HB – Huddersfield Basin; MWB – Market Weighton Block; NT – Northumberland Trough; SB – Solway Basin; SP – Staffordshire Platform; WG – Widmerpool Gulf. Based on *Breislin et al., 2020*.

The oldest Derbyshire platform limestones are the Holkerian (343 – 337 Ma) age Woo Dale Limestone Formation, a massive, fine grained, 105 m thick limestone unit. Directly overlying this is the 75 m thick packstone and grainstone Bee Low Formation of Asbian (337 – 330.9 Ma) age. The next unit is the Brigantian (330.9 – 330.3 Ma) age Monsal Dale Limestone Formation; a 75 m thick wackestone and packstone unit with chert layers. The youngest carbonate unit is the Eyam Limestone Formation of Brigantian age. It comprises thinly bedded shelly limestones and shales with mud mounds. It reaches a maximum thickness of 100 m (Chisholm *et al.*, 1983; Breislin *et al.*, 2020). The platform also hosts the largest amount of dolostone of all the Pennine Basin platforms (approximately 50 km^2), with significant amounts occurring in the southeast of the platform. This dolomite occurs in two distinct bodies, the first elongated along the Cronkston-Bonsall Fault, and the second located along the southern platform margin (Breislin *et al.*, 2020).

Mineralisation

The South Pennine Orefield has historically been one of the most important mining districts for lead in the UK. An estimated 4 million tonnes of galena concentrate were produced between when mining began in the Bronze Age until operations at the last mine ceased in 1940, along with significant amounts zinc (<1 million tonnes) in the form of sphalerite (Ford and Worley, 2016). The mineralisation is present in multiple styles, the most common being vertical fissure veins. These structures, called rakes and scrins, commonly extend for over a kilometre in strike length and formed from the precipitation of the sulfide minerals in fractured wall rock. Flats and pipes are horizontal, stratabound or stratiform deposits that usually did not exceed 1 km in length and 100 m in width. These linear deposits are a series of mineral-lined or mineral-filled cavities formed by dissolution of the wall rock (Ford and Worley, 2016). Notably, the term 'pipe' used in the context of the South Pennine Orefield in general is different than the area of interest here, located in Staffordshire (Ecton), where pipe deposits are vertical features.

Some zonation occurs within the orefield with sphalerite generally occurring in greater abundances at depth. Although abundances of galena and sphalerite are difficult to compare, Mostaghel (1985) estimated a ratio of 10:1 in favour of galena but this ratio was deemed to be inaccurate by Ford and Worley (2016) based on Mostaghel mainly analyzing samples from near the surface. Fluorite is also most common on the eastern side of the orefield, and baryte occurring dominantly in a N-S trend through the center of the orefield. Calcite is the most dominant gangue mineral on the western side (Ford and Quirk, 1995).

Structure

The Carboniferous limestones lie on top of faulted basement blocks comprised of pre-Carboniferous metasedimentary rocks and volcanics (Ford and Worley, 2016). Much of the available information on the basement rocks of Derbyshire comes from three boreholes that penetrate the Carboniferous limestone, and the differences between them (Smith *et al.*, 1985). In particular, the Eyam borehole extends to a depth of over 1800 m before reaching mudstones believed to be of Ordovician age, whereas the Woo Dale borehole reaches the basement block after 500 m (Aitkenhead *et al.*, 2002*;* Smith *et al.*, 1985). Smith *et al.* (1985) suggested that the differences between these boreholes could be explained by there being two separate tilt blocks, both dipping to the southwest. These tilt blocks, the Eyam and Woo-Dale tilt blocks, are divided by the NW-SE trending Bakewell Fault Zone, and similarly the Cronkston-Bonsall Fault Zone separates another basement block on the southwest side of the orefield (Sheldrick *et al.*, 2025).

Folding and faulting affected the limestones throughout the Carboniferous, and regional stress regime changes caused the development of multiple structural orientations of faults and folds. From the late Tournaisian to the early Visean there was NE-SW extension resulting in NW-SE faults and fractures that would later be filled by mineralisation. During the late Visean, the stress field rotated counterclockwise, resulting in ENE-WSW strike-slip fractures and wrench faults. By the end of the Visean, the stress field continued to rotate, resulting in ENE-WSW compression and forming major folds, as well as resulting in uplift and erosion. In the

Serpukhovian, NW-SE extension caused thermal subsidence, resulting in burial of the orefield to a depth of 4 km and NW-SE reverse faults (Quirk, 1987; Ford and Worley, 2016).

Magmatism

Carboniferous magmatism is widespread throughout northern Europe, forming from a magmatic province that spanned through Scandinavia, the North Sea and Northern Germany (Wilson *et al.*, 2004; Kirstein *et al.*, 2006). Specifically in northern England, extensional tectonics north of the Variscan front caused fault-controlled basins and basaltic magmatism (Upton *et al.*, 2004). Some of the earliest examples of alkaline and sub-alkaline Carboniferous magmatism in the UK are found within the South Pennine Orefield, preserved as both basaltic flows and diabase (dolerite) sills. The youngest intrusion in the South Pennine Orefield is the Calton Hill Sill, dated using Ar^{40}-Ar^{39} to be 316.4 ± 3.7 Ma. The sill is a diabase with microphenocrysts of olivine and clinopyroxene, and contains a diverse assemblage of xenoliths, including olivine-rich spinel lherzolites, pyroxenites, and harzburgites (Sheldrick *et al.*, 2025). The oldest known magmatic units in the orefield are the basaltic lava flows (Lower Miller's Dale, Lower Matlock, Shacklow Wood), as well as the Tideswell Dale Sill and Waterswallows Sill. The basaltic units generally exhibit hypocrystalline texture and sericitic alteration of plagioclase. The Tideswell Dale Sill is a 20 m thick diabase, intruded into the Monsal Dale Limestone Formation. The Waterswallows Sill is an olivine-microphyric diabase intrusion and has been dated to be 328.6 ± 4.2 Ma (Sheldrick *et al.*, 2025).

Many of the magmatic units described above occur in the northern part of the South Pennine Orefield, around the Bakewell Fault (**Fig. 1**), and the thicker sedimentary package of the Eyam tilt block. The crustal scale Bakewell Fault, as well as the Cronkston-Bonsall Fault system, have been implicated as conduits for melt generated from decompression-melting of the mantle from a plume finger (Sheldrick *et al.*, 2025). These magmatic units were identified within the various mine workings of the South Pennine Orefield, and the basaltic units (a few meters in thickness) were historically called 'toadstones' while tuffaceous clay layers (a few centimeters in thickness) were called 'clay wayboards' (Ford and Quirk, 1995). The magmatic layers formed an impermeable layer in many of the Pb-Zn deposits, and the ore deposits preferentially form directly below these layers (Ford and Worley, 2016).

Carboniferous magmatism is also present within the North Pennine Orefield, located on the Alston Block and Askrigg Block (**Fig. 2C**). The Great Whin Sill (Johnson and Dunham, 2001) is a tholeiitic quartz-diabase intrusion emplaced during the late Carboniferous (297 ± 0.4 Ma). Recent work by Dempsey *et al.* (2021) has shown that Pb-Zn-Cu mineralisation within the North Pennine Orefield is coeval with the emplacement of this sill complex, and that the MVT classification of that orefield was incorrect. This conclusion was based on Re-Os isotopic evidence that the sulfide and fluorite mineralisation was linked to the primitive mantle source that formed the Great Whin Sill.

2.2 Ecton Geology

Ecton Copper Mine is located on the western side of the South Pennine Orefield. It is located on Ecton Hill (**Fig. 4A**), and situated in north-east Staffordshire, whilst the remainder of the orefield is located in Derbyshire. The Staffordshire limestones are stratigraphically related to the Derbyshire equivalents, but the former are mostly deep-water facies, being deposited in the carbonate ramp setting of the Widmerpool Gulf (**Fig. 2A**) (Aitkenhead *et al.*, 2002; Ford, 2000).

The Chadian (346.7 – 344.5 Ma) age Milldale Limestone Formation (equivalent to the Derbyshire 'Woo Dale Limestone Formation') is fine grained and contain numerous mud-mounds, also referred to as "knoll-reefs". The unit forms the core of the Ecton Anticline and is at least 700 m thick. Overlying the Milldale Limestone Formation are the Asbian (337 – 330.9 Ma) age Ecton Limestone Formation (equivalent to the Derbyshire 'Bee Low Limestone Formation'). They are thinly bedded alternating dark, fine-grained turbidite limestone with mudstone. There are sporadic chert nodules or bands, as well as cm-scale tuffaceous units. The unit is at least 225 m thick. The Brigantian (330.9 – 330.3 Ma) age Mixon Limestone Formation (equivalent to the Derbyshire 'Monsal Dale Limestone Formation') is a 200 m thick unit of limestone, interbedded with mudstone (Aitkenhead *et al.*, 2002; Ford, 2000).

The geology underlying the Milldale Limestone Formation is poorly understood, as there is no exposure and none of the mines were worked to a great enough depth (Ford, 2000). The Caldon Low Borehole, located 10km south of Ecton (**Fig. 1**), intercepted two units beneath the Milldale Limestone Formation; the Rue Hill Dolomites and the Redhouse Sandstones, although their full extent is not known (Aitkenhead *et al.*, 2002). Both of these units are believed to be of Courceyan age (358.8 – 346.7 Ma).

Ecton Hill is the focus of a N-S trending anticline that plunges to the north, and has a steeply dipping eastern limb (Ford, 2000). Due to compression from the south, the typical Variscan Orogeny regional fold pattern is E-W, making the Ecton anticline and other local folds regionally uncommon. The eastern limb of the anticline is bounded by a series of reverse faults that extend from a deep basement structure (**Fig. 4B**) (Corfield *et al.*, 1996). These reverse faults have been interpreted to be the result of the Variscan inversion. Diagrams from Critchley (1979) show that the limestone beds on the western limb are relatively flat-lying, and tight folds increase in proximity to the copper orebodies.

Mineralisation

There are three main styles of mineralisation present at Ecton: lodes, saddles and pipes (Ford, 2000). Saddles (**Fig. 3A**) are related to folds within limestone beds, forming mineralised bedding planes on either side of the axial plane, as well as joints forming along axial planes of the folds (Ford, 2000). Pipe deposits were the most significant source of ore, the largest being the Deep Ecton and Clayton pipes. These orebodies were cylindrical and nearly vertically oriented,

cross cutting the folded limestone beds, and roughly aligned in a N-S line on the eastern limb of the Ecton anticline (Ford, 2000).

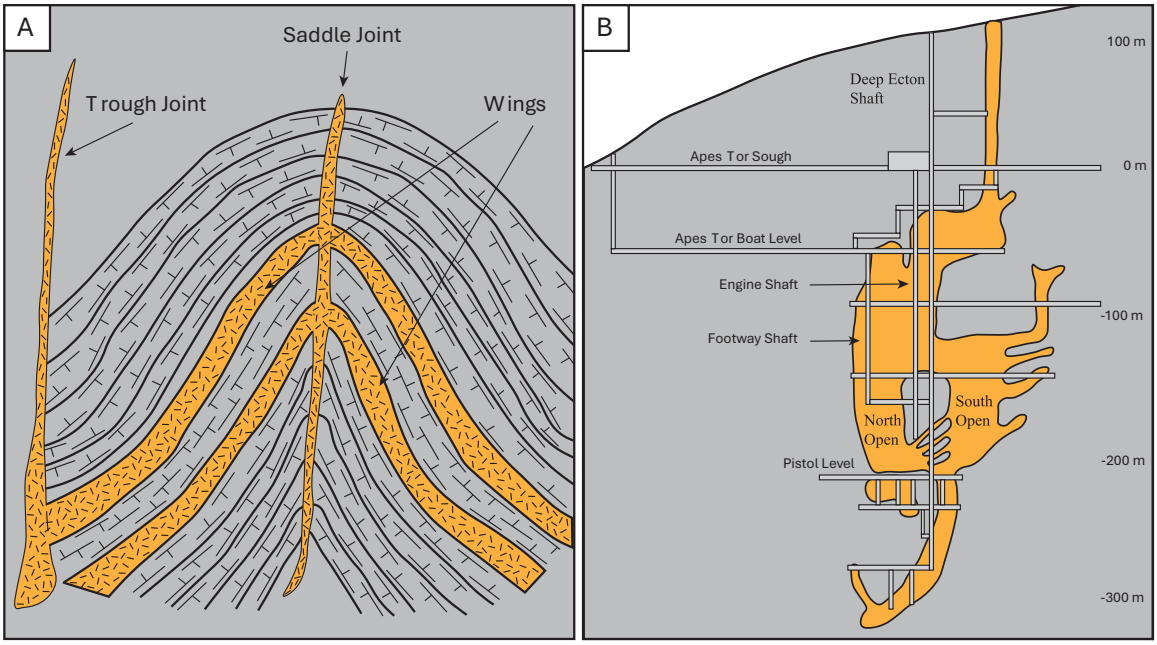

Figure 3: Schematic illustrations of the mineralisation styles present at Ecton Mine. *(A)* Saddle deposit with mineralised joints and wings. Based on *Watson, 1860*. *(B)* Schematic section of Ecton pipe and mine workings. Based on *Ford, 2004*.

The Deep Ecton pipe was the largest ore body and was worked to a depth of 300 m below adit level and 420 m below the surface of the hill (Ford, 2004). The pipe does not widen significantly until ~30 m below the surface of the hill and has very little outcrop at the surface (Ford, 2000). Although roughly cylindrical, the orebody had an irregular shape and reached a maximum width of 182 m. The pipes on Ecton Hill crosscut the folded limestone beds, and the mineralisation was primarily hosted by the Ecton Limestone unit, but the deepest workings extended into the Milldale Limestones as well (Ford, 2004). Due to the permanent flooding of the mine workings, detailed descriptions of the texture of the orebody have not been possible in the field or underground from the 20th Century onward but based on historical descriptions the pipes were likely breccias of calcite, limestone and copper ore (Ford, 2000).

The principal ore mineral at Ecton was chalcopyrite, although many other copper minerals occur, including native copper, bornite, cuprite, covellite, chalcocite and tenorite (Ford, 2000). Galena and sphalerite also occur at the Ecton mines, although in much smaller volumes than the copper phases, and display similar zonation patterns as the rest of the South Pennine Orefield, with galena occurring closer to the surface, and the amount of sphalerite increasing with depth (Ford and Worley, 2016). Millerite occurred as a rare sulfide mineral (Starkey, 2018). Oxidation products of copper can be found close to the surface of the hill including malachite, azurite, cerussite, smithsonite, aurichalcite and rosasite (Ford, 2000). The oxidized ores are likely

what led to the bronze age mining at Ecton, with these minerals being visible in the limestone outcrops on top of Ecton Hill. The occurrence of prehistoric and Bronze Age mining at Ecton is evidenced by near surface mine workings on top of the hill, as well as bone tools found in trenches and hollows (Timberlake, 2014).

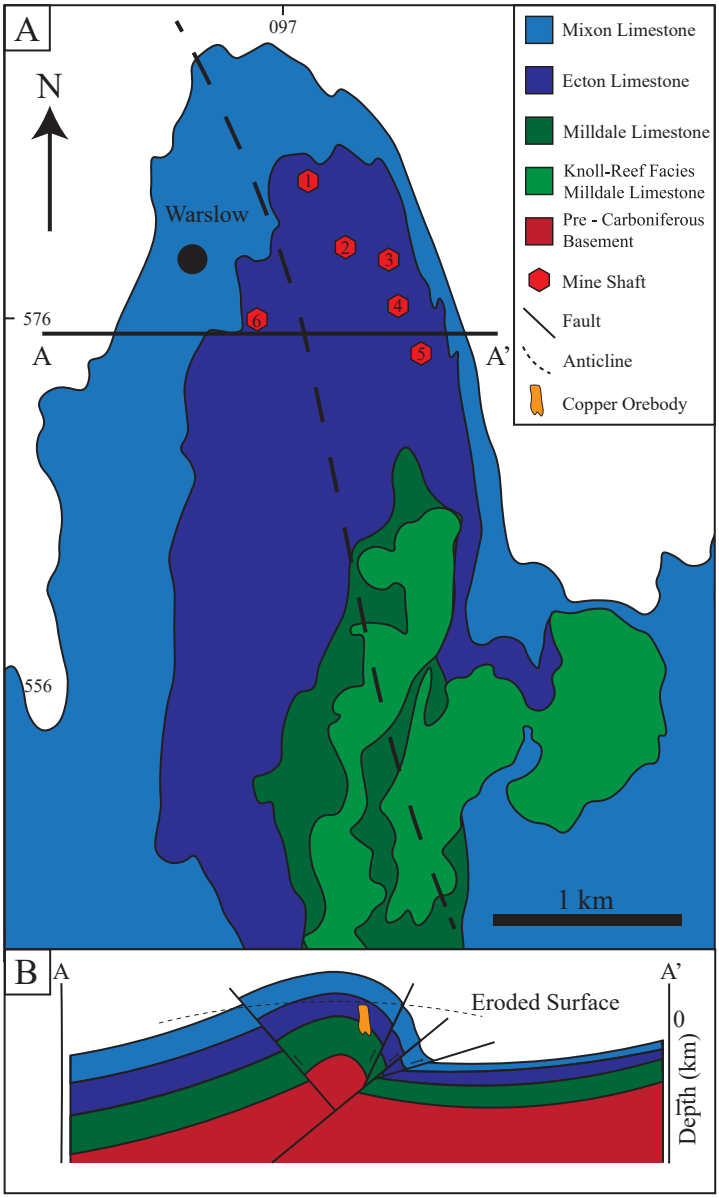

Figure 4: *(A)* Geological map of Ecton Hill with approximate locations of mines. 1) Deep Ecton Mine. 2) Clayton Mine. 3) Chadwick Mine. 4) Bag Mine. 5) Waterbank Mine. 6) Swainsley Mine. Based on *Ford, 2000; Aitkenhead 1971*. Grid numbers apply to British National Grid square SK05 *(B)* Cross-section of transect A-A'. Modified from *Corfield et al., 1996.*

3. Sample Descriptions

Due to the mineral resources at Ecton being effectively exhausted, in-situ study material is not possible to obtain. Much of the remaining material resides in museums or private collections but without relevant information regarding the location within the mine from which it originated. For this study, samples were obtained through the collections at Manchester Museum (#10270 and #2278), UK, and the Canadian Museum of Nature (CMNMC 35254).

Sample 1 (Manchester Museum - #10270)

This sample is a 5 cm long, 4 cm wide calcite crystal with well defined cleavage planes (**Fig. 5A-B**) and also contains multiple small pieces of calcite that have cleaved off the main crystal (**Fig. 5C-D**). The calcite crystal has abundant chalcopyrite inclusions within, which are restricted to discrete zones of mineralisation. Less commonly, there is also euhedral chalcopyrite encrusting the exterior of the calcite (**Fig. 5C**). The chalcopyrite grains have a maximum size of 1mm and have a brassy-yellow colour but grains on the exterior of the calcite can be iridescent.

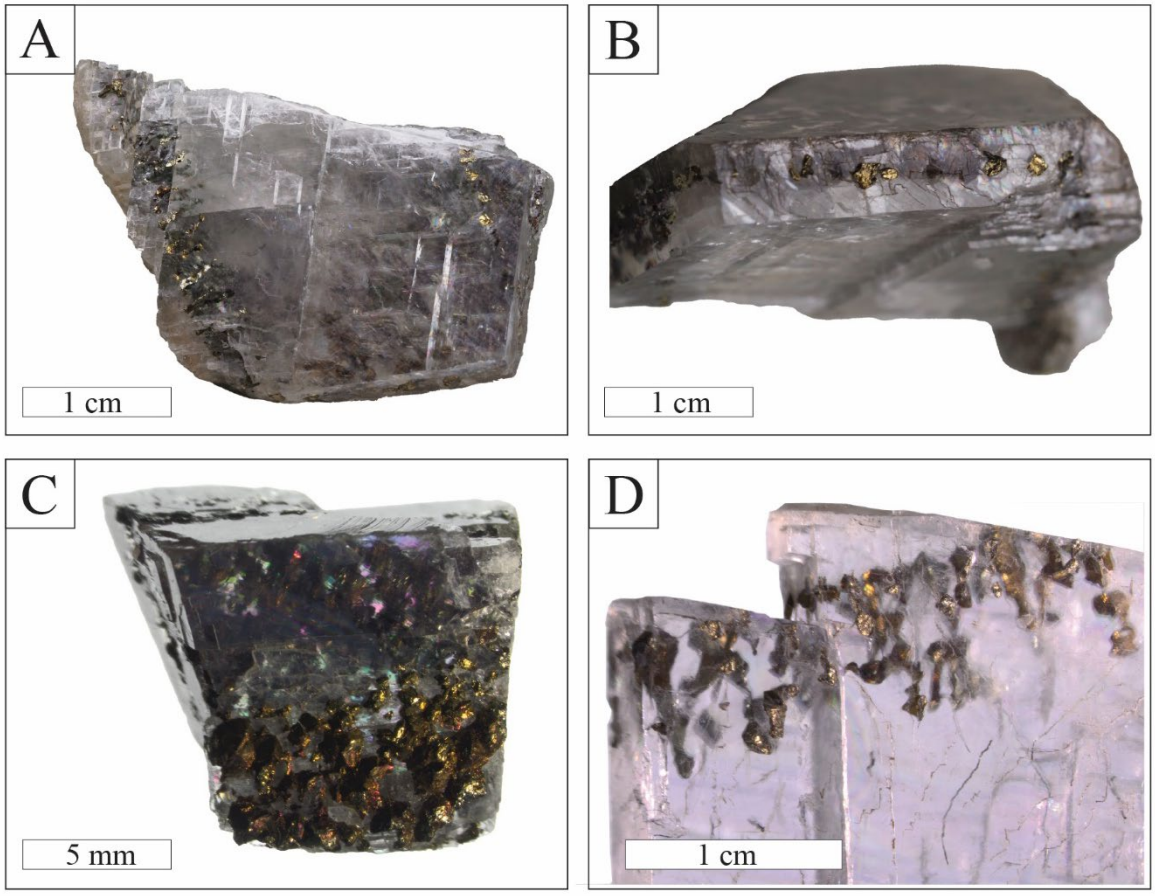

Figure 5: Photos of *Sample 1* from Manchester Museum. *(A)* Single calcite crystal with chalcopyrite inside calcite. *(B)* Top view of calcite crystal showing euhedral aligned chalcopyrite grains. *(C)* Small calcite piece cleaved off

main calcite crystal. Euhedral chalcopyrite grains encrusting the calcite. *(D)* Small calcite piece cleaved off main crystal. Euhedral chalcopyrite within the calcite in a narrow zone.

Sample 2 (Manchester Museum - #2278)

This sample contains two calcite pieces taken from a larger specimen at the Manchester Museum. The first is an 8 cm long, 5 cm wide euhedral group of scalenohedral calcite crystals (**Fig. 6A-B**). The second piece (**Fig. 6C-D**) is a 4 cm wide euhedral calcite scalenohedron (commonly called 'dogtooth calcite'). Both pieces are encrusted by chalcopyrite that ranges from micron-scale anhedral crystals to 3 mm wide euhedral crystals. The larger chalcopyrite crystals have a tetrahedral habit and have a brassy-yellow colour, but many crystals are also iridescent. Within the calcite crystals there is also fine subhedral to euhedral chalcopyrite with a brassy-yellow colour. This sample is an example of the most common style of Ecton copper mineralisation (*Starkey, 2018*).

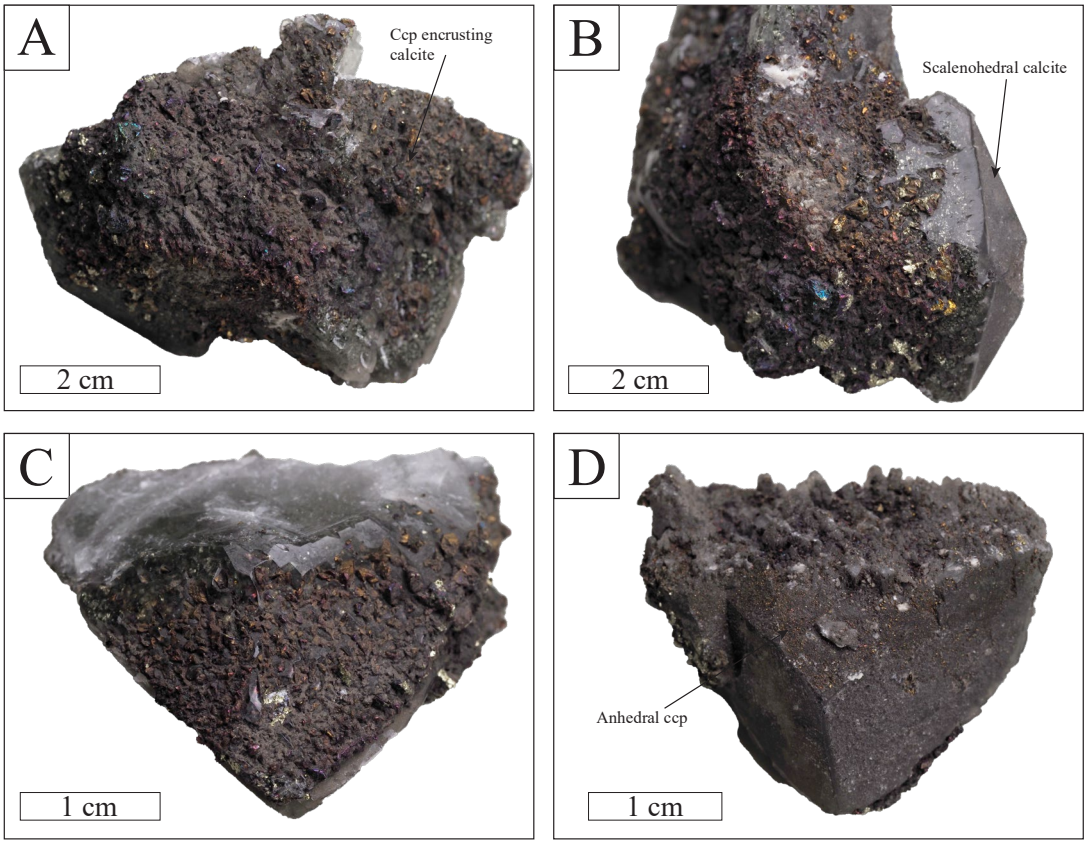

Figure 6: Photos of *Sample 2* from Manchester Museum. *(A)* Scalenohedral calcite crystals encrusted with large, iridescent, euhedral chalcopyrite. *(B)* Side view of *A*, showing large scalenohedral calcite crystal with brassy-yellow chalcopyrite inside the calcite. *(C)* Dogtooth calcite crystal with large iridescent chalcopyrite encrusting the calcite. *(D)* Reverse side of *C*, showing fine grained chalcopyrite encrusting three crystal faces of the calcite.

Sample 3 (Canadian Museum of Nature - CMNMN 35254)

This sample is a 4 cm long rhombohedral calcite crystal (**Fig. 7a**) showing exposed cleavage faces. Brassy-yellow chalcopyrite can be seen within the calcite, developed in elongated shapes. The lengthened portions of the chalcopyrite appear to have a bladed habit, being wider than they are thick and have a larger, euhedral portion on one end (**Fig. 7C**). The chalcopyrite has a distinct termination point within the calcite, marking a growth boundary as well as a direction of growth (**Fig. 7B**). Most of the chalcopyrite within the calcite follows the same growth direction, but a small group are perpendicular to the rest (**Fig. 7D**).

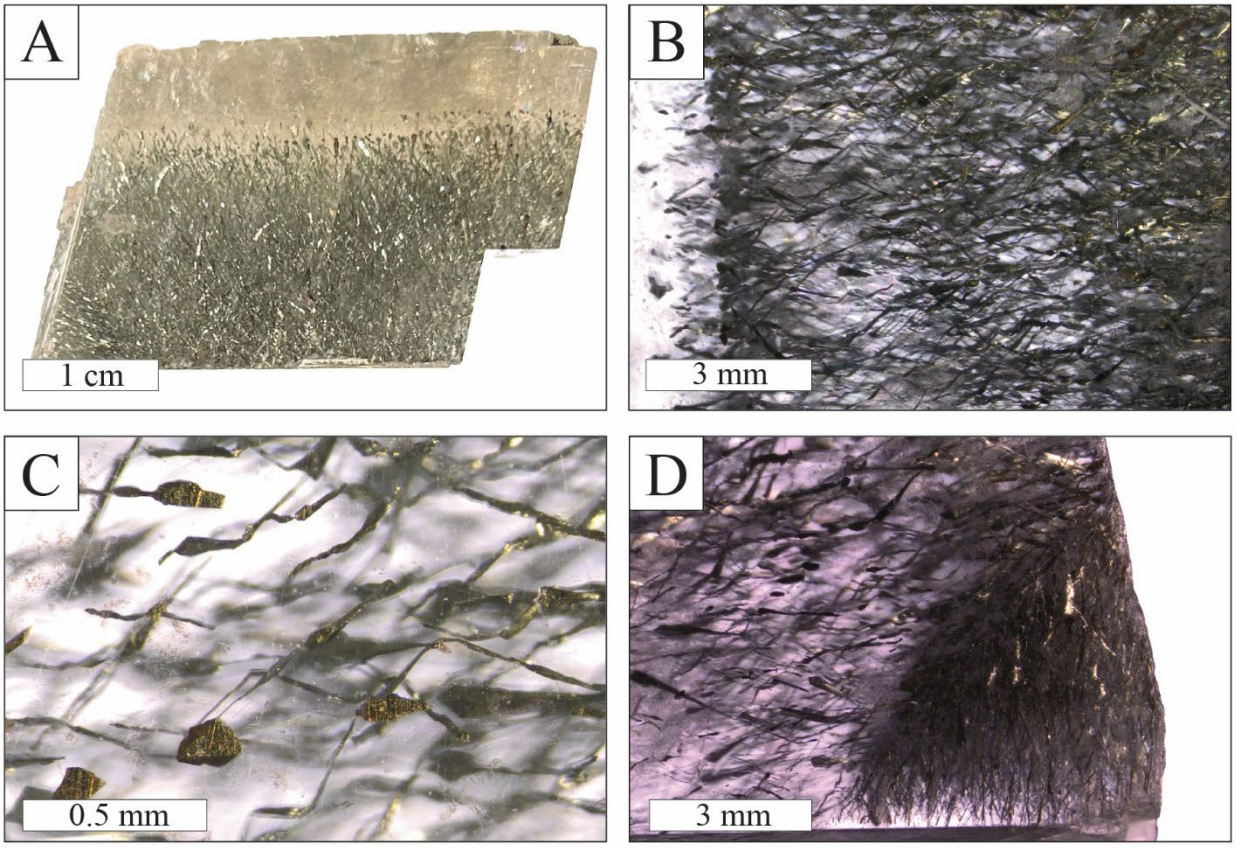

Figure 7: Photos of *Sample 3* from the Canadian Museum of Nature. *(A)* Rhombohedral calcite crystal with elongated chalcopyrite grains within the calcite. *(B)* Elongated chalcopyrite grains within calcite with clear termination point (left side of image). *(C)* Close-up image of *B* showing larger euhedral chalcopyrite at one end of the elongated, bladed chalcopyrite. *(D)* Elongated chalcopyrite grains with a differing orientation to the rest of the sample.

3.1 Optical Microscopy

Sample 1 (Manchester Museum - #10270)

This thin section (**Fig. 8A**) is mostly composed of calcite that is colourless in PPL. All of the calcite goes extinct at the same angle, indicating it is a single crystal. Chalcopyrite is the most abundant sulfide in this thin section, comprising approximately 5 mod.% of the sample. When viewed in reflected light, the chalcopyrite grains have a distinct orange colour and a wide range in size. The largest grain is 2500 µm in length and 1000 µm in width, while the smallest grains are equant and <10 µm in length. The grains have variable shapes, many being elongate with sharp boundaries, and others being approximately triangular. The chalcopyrite grains are restricted to a narrow zone within the calcite, shown by **Figure 8A**.

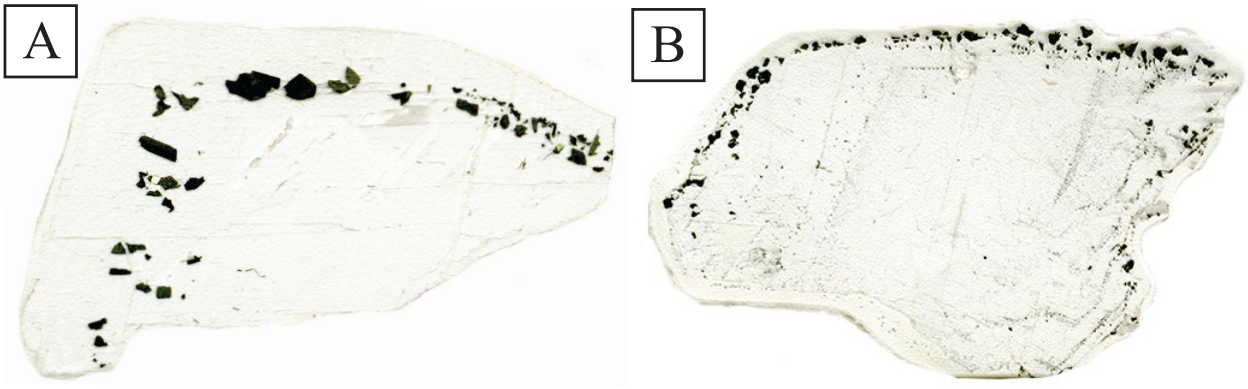

Figure 8: Thin sections made for optical microscopy. *(A)* Thin section made from *Sample 1* zoned calcite crystal **(Fig. 5A)**. *(B)* Thin section made from *Sample 2* scalenohedral calcite **(Fig. 6A)**.

Pyrite is observed very rarely in this sample and is the only other sulfide mineral present. These grains have a cream-yellow colour in reflected light and are commonly surrounded by chalcopyrite (**Fig. 9A-C**). The pyrite is typically anhedral and sub-rounded, ranging in length from 5 µm to 20 µm.

Barite is the least common mineral in this sample, observed as white, subhedral to euhedral grains surrounded by calcite. The grains are typically elongated, with lengths up to 100 µm and a width of 5 µm. Barite is also restricted to the mineralised zones in the calcite, occurring in close proximity to the larger chalcopyrite grains.

Sample 2 (Manchester Museum - #2278)

Sample 2 has a much more diverse mineral assemblage when viewed in thin section (**Fig. 8B**). Calcite is the dominant mineral (approximately 90 mod.%) and is colourless when viewed in PPL. In contrast to the single calcite crystal which makes up *Sample 1*, this sample is made of multiple calcite crystals. Of the sulfide minerals present in this sample, chalcopyrite is the most abundant (approximately 5 mod.%) and when viewed in reflected light, has an orange colour. The grains have a large range in size and shape, being equant or elongated, and the largest are on

the order of 800 µm long and 300 µm wide. The large chalcopyrite grains are restricted to the edges of the calcite (**Fig. 8B**), but there are small (5 µm – 50 µm) subrounded grains disseminated throughout the entirety of the calcite (**Fig. 10F**).

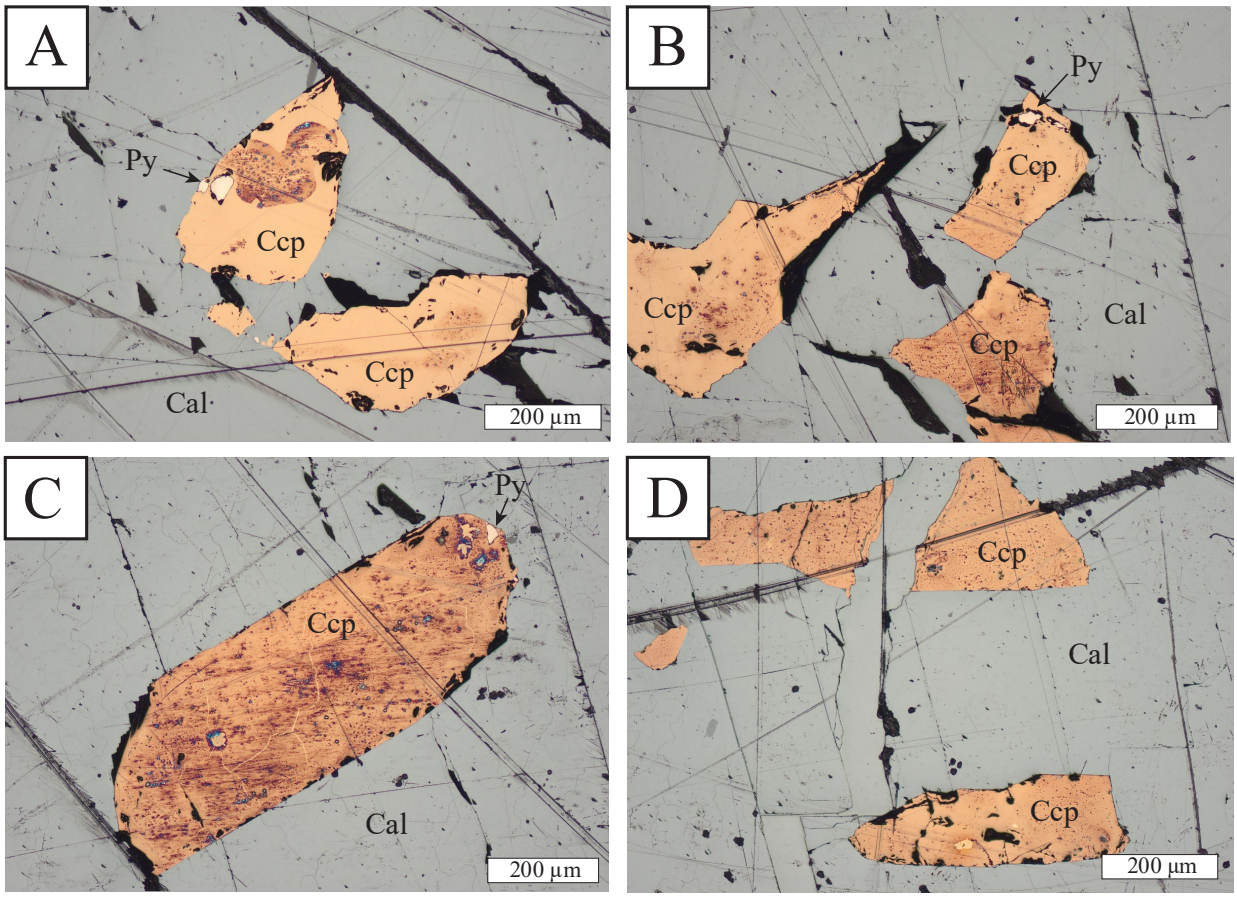

Figure 9: Reflected light photomicrographs of *Sample 1*. *(A)* Large triangular chalcopyrite (Ccp) grains hosted in calcite (Cal). Small subrounded pyrite (Py) within chalcopyrite. *(B)* Chalcopyrite grains of varying size within calcite. Small pyrite grain within chalcopyrite. *(C)* Large, elongated chalcopyrite within calcite. Small pyrite grain on edge of chalcopyrite. *(D)* Triangular and elongated chalcopyrite grains within calcite.

The second most abundant sulfide mineral is marcasite (less than 5 mod.%). In reflected light, marcasite is birefringent, ranging from a cream-yellow to grey colour. The grains occur as groups where multiple subhedral grains can be observed together (**Fig. 10B, C**). Marcasite is restricted to the same area as the large chalcopyrite grains around the edge of the calcite and has similar size with the largest grains being approximately 600 µm long and 400 µm wide.

Pyrite usually occurs as euhedral cubic grains, commonly in direct association with marcasite (**Fig. 10B**) or chalcopyrite (**Fig. 10D**). When observed in reflected light it has a cream-yellow colour and is isotropic.

There are two nickel-minerals present in this sample, firstly (and more abundantly) Ni-rich pyrite ($(Fe,Ni)S_2$). It occurs as euhedral, octahedral grey grains, up to 100 μm in width. These grains are observed to be in contact with, or surrounded by, marcasite (**Fig. 10A, F**). Gersdorffite (NiAsS) is observed rarely in this sample and occurs as small (10 μm wide) anhedral grains with a pale grey colour when viewed in reflected light (**Fig. 10C**). Gersdorffite is most commonly observed on the margins of larger marcasite or Ni-rich pyrite grains.

Galena is the least common sulfide mineral in this sample, observed as small, elongated, anhedral grains, between 5 μm and 20 μm in length. These grey grains are observed in contact with larger chalcopyrite and marcasite grains (**Fig. 10C**).

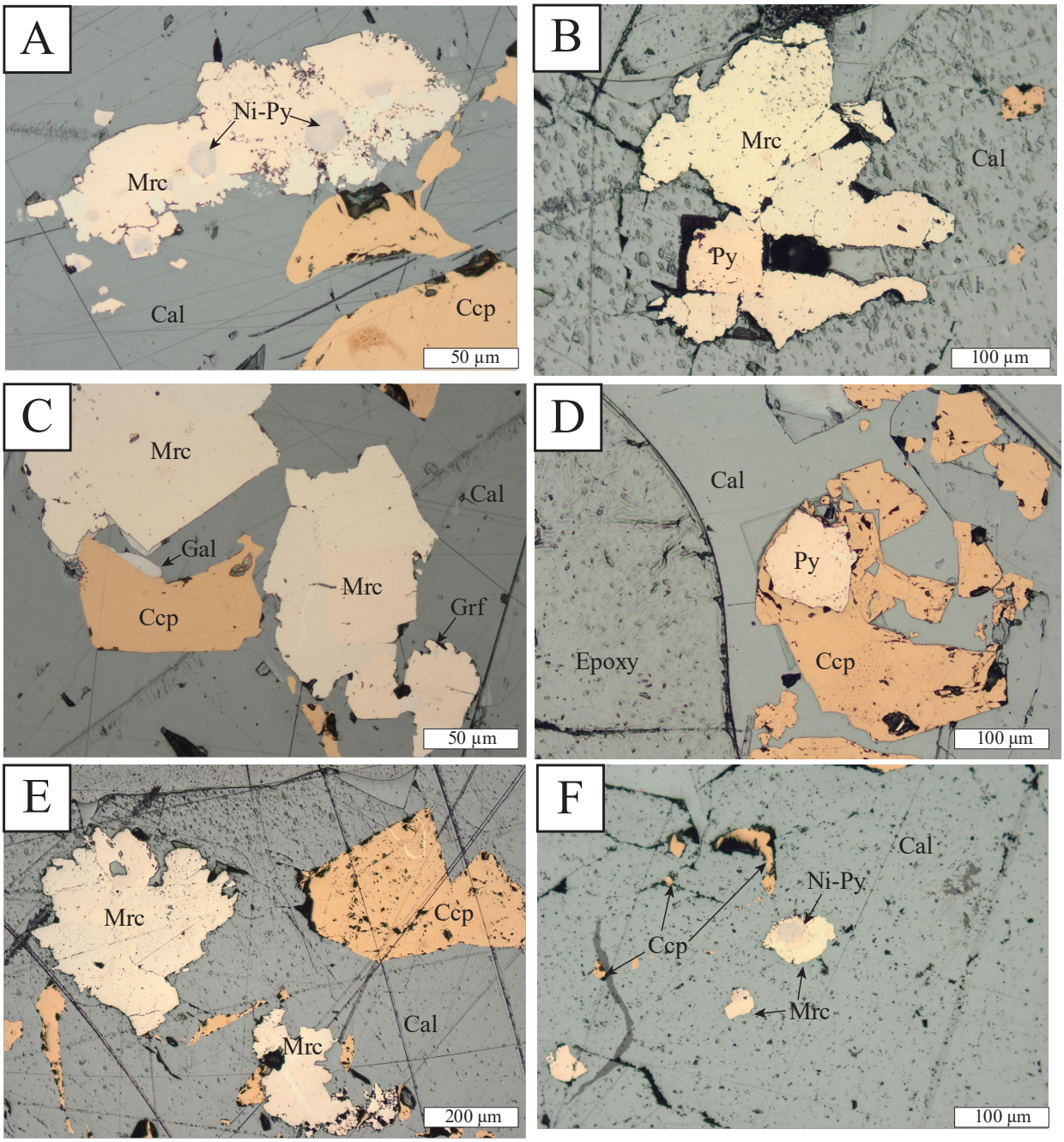

Figure 10: Reflected light photomicrographs of *Sample 2*. *(A)* Elongated cluster of marcasite (Mrc) grains with multiple Ni-rich pyrite (Ni-Py) within. *(B)* Large marcasite grains partially surrounding euhedral, cubic pyrite (Py). *(C)* Marcasite grain boundaries displayed by birefringence colours. Small gersdorffite (Grf) grains along edge of marcasite. Elongated galena (Gal) grains along grain boundaries of marcasite and chalcopyrite. *(D)* Large pyrite grain with irregular boundaries surrounded by chalcopyrite. *(E)* Large marcasite and chalcopyrite grains along the edge of calcite crystal. *(F)* Ni-rich pyrite grain surrounded by marcasite. Very small subrounded chalcopyrite grains representing disseminated chalcopyrite throughout the calcite.

4. Analytical Techniques

One polished thin section was made for each of *Sample 1* and *Sample 2*. These thin sections were used for petrographic observations using both transmitted and reflected light microscopy.

Electron microprobe analysis

Mineral chemical analyses were carried out using a JEOL-JXA 8230 Electron Microprobe at the University of Ottawa. The compositions of sulfide minerals were determined with a beam energy of 20 kV, a beam current of 40 nA, and a beam diameter of 2 μm. Elements were acquired using analyzing crystals LIFL for Fe, Co, Ni, and Cu, PETJ for Sb, S, Bi, Te, Pb, and Cd, and TAP for Se, As, and Zn. The electron microprobe was calibrated by the following standards: cochromite for Co, cubanite for Fe, S, and Cu, galena for Pb, GaAs for As, sphalerite for Zn, pentlandite for Ni, Bi_2Se_3 for Se and Bi, Sb_2Te_3 for Te and Sb, greenockite for Cd. The count time was 20 seconds for all elements, and off-peak count time was 20 seconds for all elements.

The compositions of calcite and barite were determined with a beam energy of 15 kV, a beam current of 20 nA, and a beam diameter of 10 μm. Elements were acquired using analyzing crystals LIF for Mn, LIFL for Fe, PETJ for Ca, Ba, Sr, and P, PETL for S, and TAP for Na, Al, Si, and Mg. The electron microprobe was calibrated by the following standards: albite for Na, apatite for P, barite for Ba, Celestine for S, sanidine for Al, Si, and K, tephroite for Mn, Smithsonian calcite for Ca, Smithsonian dolomite for Mg, Smithsonian siderite for Fe, and Smithsonian strontianite for Sr. The count time was 20 seconds for all elements, and off-peak count time was 20 seconds for all elements.

Quantitative element maps were collected for five separate areas (**Fig. 11**) on *Sample 2*, targeting S, As, Cu, Ni, Zn, Pb, Mg, Fe, Co, Se, Bi, Al, Mn, Cd, and Si. A beam current of 200 nA and voltage of 20 kV was used with a resolution of 2.5 μm per pixel.

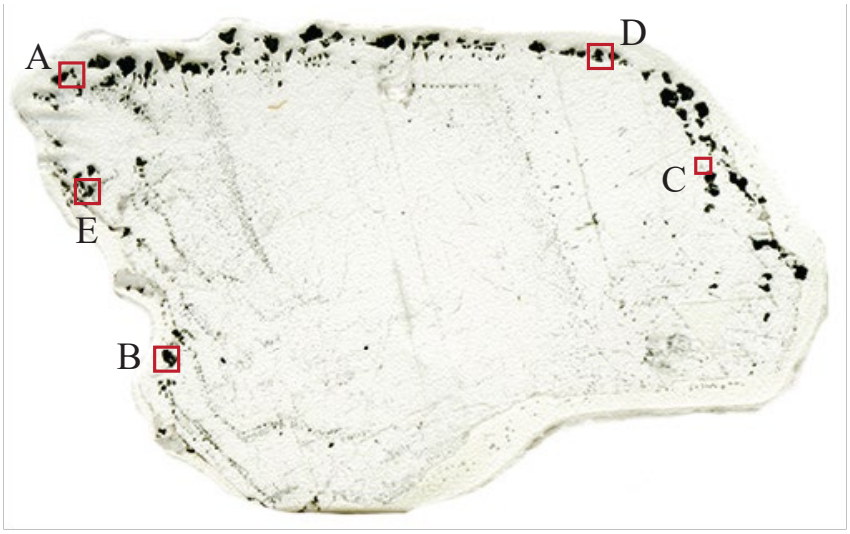

Figure 11: Spatial distribution of element map areas taken for *Sample 2*. A-E corresponds to **Figure 12** notation.

Cathodoluminescence

Cathodoluminescence images were collected on calcite from the polished thin section of *Sample 2*. This analysis was completed at the University of Ottawa using a QTL-Mk5-2 Cathodoluminescence Stage on an Olympus BX-51 Microscope and images were captured using a Nuance Multispectral imaging system.

Laser ablation-inductively coupled plasma mass spectrometry

Sulfide LA-ICP-MS:

In situ LA-ICP-MS analyses on sulfide minerals were carried out at LabMaTer (UQAC) using a 193 nm RESOlution laser ablation system (Applied Spectra, California) equipped with a S-155 double volume ablation cell (Laurin Technic), attached to an Agilent 7900 ICP-MS. A laser beam size of 55 µm in static spots mode was used, with a pulsing rate of 15 Hz and a fluence of 3 J/cm^2. The data were processed using the 3D-TE-DRS module (Paul *et al.*, 2023) in IOLITE v4 software (Paton *et al.*, 2011). The calibration was achieved by combining four reference material: the artificial sulfides pressed pellet USGS-MASS-1 (Wilson *et al.*, 2002) and UQAC-FeS-5 (Savard *et al.*, 2018) and the USGS basaltic glasses GSD-1g and GSE-1g (Jochum *et al.*, 2005). No internal standard was used to achieve fully quantitative results. Instead, normalization to 100% based on 34S, 57Fe, 65Cu, 60Ni and 66Zn was performed, which yield to high-quality results (Savard *et al.* 2023).

Calcite LA-ICP-MS:

In situ LA-ICP-MS analysis on calcite were carried out at the University of Ottawa Laser Ablation Lab using an Applied Spectra RESOlution-SE laser ablation system, attached to an Agilent 7700x ICP-MS. A laser beam size of 64um in static spots was used, with a pulsing rate of 10 Hz and a fluence of 6 J/cm^2. For continuous line analyses, the data was segmented into 2

second intervals with a scan rate of 32 μm/s, corresponding to a 64x64 μm pixel along the path. The data were reduced using Iolite 3D Trace Element DRS (Paton *et al.* 2011, Paul *et al.*, 2012). The calibration was achieved using reference material NIST612, except for Fe which used GSE1G. The check standards used were GSE1G, NIST610, and MACS3. An internal standard of measured CaO wt.% from microprobe data at the location of each line analysis was used to calibrate resultant values.

Sulfur isotopes

Six chalcopyrite grains were taken from each of *Sample 1* and *Sample 2* (total of 12 grains). These grains were plucked from both the exterior of the calcite crystals, and from within the interior of calcite crystals. Powdered samples were weighed into tin capsules with a target weight of 0.09 mg to collect 30 μg of S from the chalcopyrite. Samples are loaded into an Elemental Analyser (EA) Isotope Cube in S mode (Elementar, Germany) to be flash combusted at 1800˚C. Released gases were carried by helium through the EA where water was chemically removed and SO_2 separated from CO_2 and N_2 by a trap and purge column. SO_2 gas was carried into the Delta Q isotope ratio mass spectrometer (ThermoFinnigan, Germany) via a conflo IV interface for ^{34}S determination. Analytical precision is reported as ±0.3‰.

5. Results

5.1 Element Mapping and Backscatter Electron Imaging

Figure 12 shows element maps taken for five locations on the thin section for *Sample 2*. These images show varying pattens of zonation in multiple elements across different sulfide grains. The elements that most commonly display zonation in the sulfide minerals are Cu, Ni, Co, As, and Fe. Marcasite displays both oscillatory (**Fig. 12C, E**) and inverse (**Fig. 12A**) zonation of Cu and Ni. The oscillatory zoning shows concentric layers of increasing and decreasing element abundance within the crystal structure. The inverse zonation, where the core the of sulfide grain has lower concentrations of compatible elements than the surrounding rim, shows increased concentrations of Ni around the grain boundaries of the anhedral marcasite. This style of zonation is also displayed by As, at lower concentrations than Ni and Cu, where As is concentrated along the edges of marcasite crystals, or grain clusters. Pyrite also displays both oscillatory (**Fig. 12B**) and inverse (**Fig. 12D**) zonation of Cu, Ni, and As. The oscillatory zonation in pyrite is evident in both Cu and Ni, while inverse zonation is clearly defined by Ni, Cu, and As in euhedral pyrite grains. Sector zoning, where the sulfide is divided into sectors that are defined by increases in composition along crystal faces, is displayed by Ni-rich pyrite (**Fig. 12A, C**) where Co and Ni are elevated in distinct areas of the grain. Within the Ni-rich pyrite

grains, Ni and Fe display inverse zonation of each other (**Fig. 12A**) where Ni concentrations increase towards the outside of the grains and Fe increases towards the center.

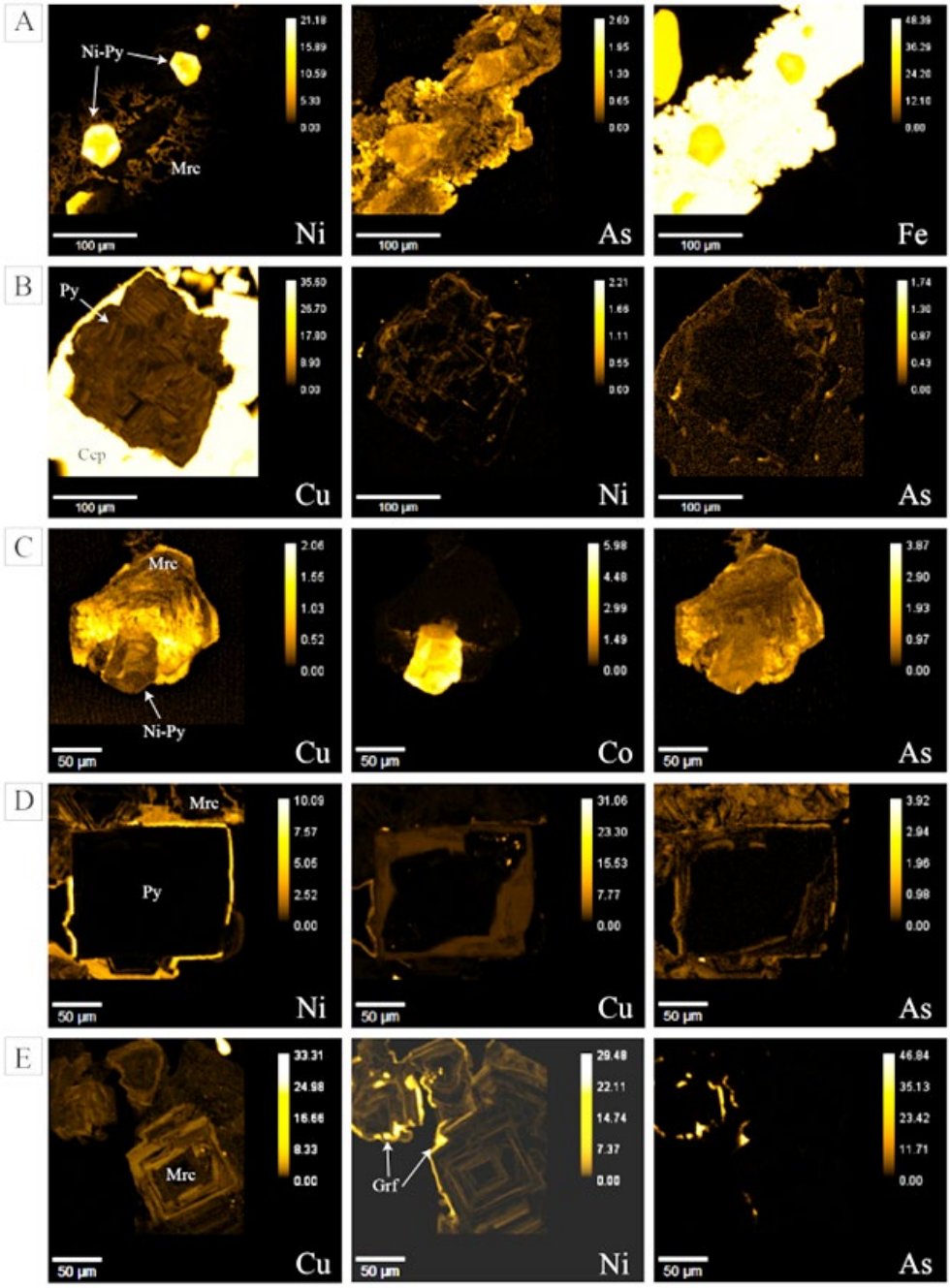

Figure 12: Element maps for five locations in the Ecton samples (in atomic wgt. % ?). *(A)* Euhedral Ni-rich pyrite grains completely surrounded by marcasite. Element maps of Ni, As, and Fe. *(B)* Pyrite grain completely surrounded by chalcopyrite. Element maps of Cu, Ni, and As. *(C)* Ni-rich pyrite grain partially surrounded by marcasite. Element maps of Cu, Co, and As. *(D)* Euhedral cubic pyrite grain with marcasite above and below. Element maps of Ni, Cu, and As. *(E)* Marcasite grains with gersdorffite along the grain boundaries. Element maps of Cu, Ni, and As.

Backscatter electron images (**Fig. 13**) of the sulfide minerals show the distribution of grains within the calcite. These images show the chalcopyrite and marcasite grains aligned in straight lines, which mark a boundary in the calcite crystal where sulfide growth stopped (**Fig. 13A**). These sulfides intersect at angles of 112° and 73° (**Fig. 13B**) which is close to the ideal growth angles of calcite (105° and 75° of the $\{10\bar{4}\}$ rhombohedral faces). The backscatter electron images also provide enhanced observations of small, anhedral gersdorffite grains, which can be observed along the grain boundaries of marcasite (**Fig. 13C**) and Ni-rich pyrite (**Fig. 13D**). Gersdorffite in the Ecton samples is only found along grain boundaries of these two sulfides, more commonly along Ni-rich pyrite grains.

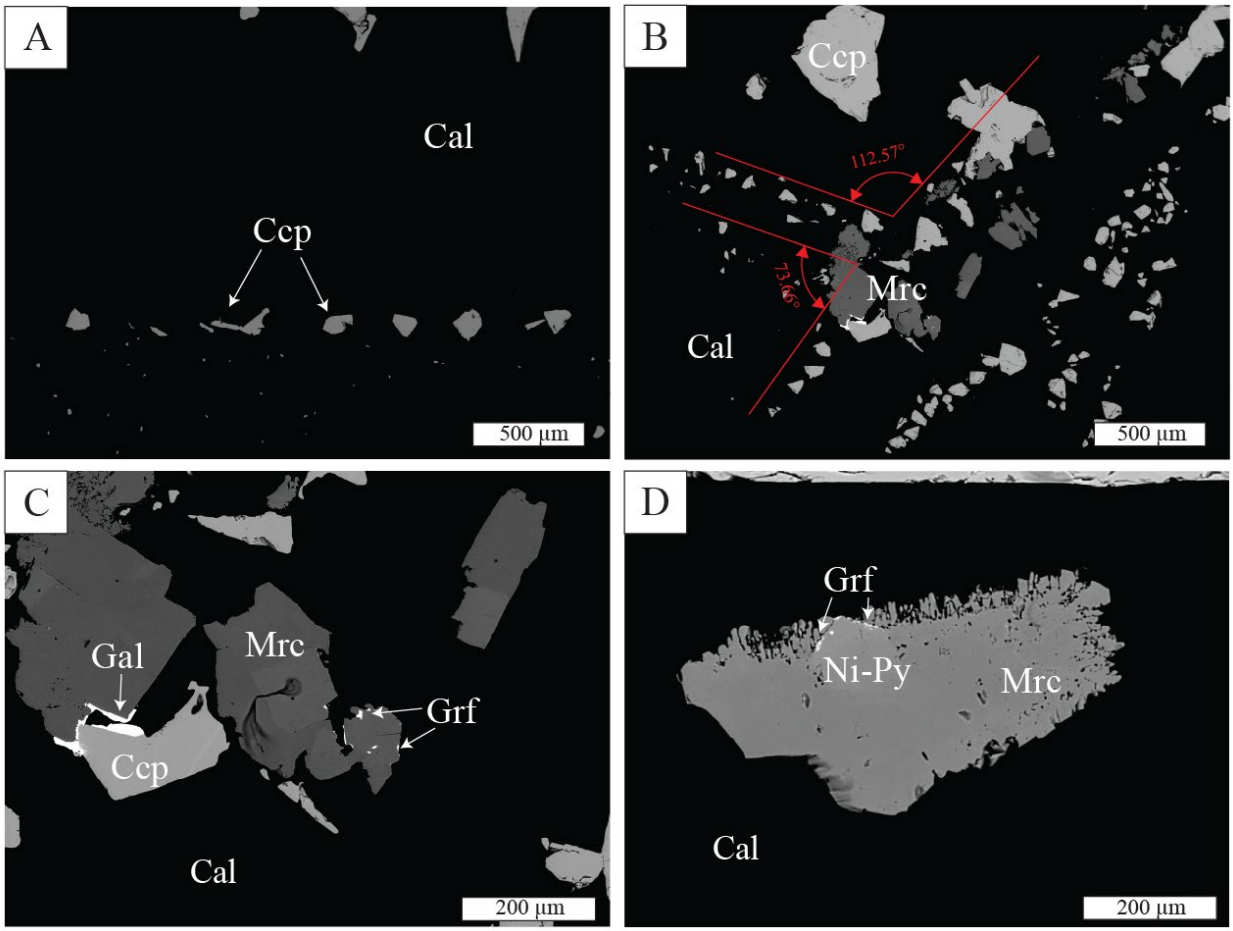

Figure 13: Backscatter electron images. *(A)* Aligned chalcopyrite (Ccp) grains with smaller disseminated chalcopyrite below, and zone of barren calcite (Cal) above. *(B)* Intersection of aligned chalcopyrite and marcasite (Mrc) grains with intersection angles. *(C)* Small gersdorffite (Grf) grains along the grain boundaries of marcasite. *(D)* Ni-rich pyrite (Ni-Py) grain partially surrounded by large marcasite grain. Gersdorffite grains along the outer edge of Ni-rich pyrite.

5.2 Cathodoluminescence

Cathodoluminescence images (**Fig. 14**) are used to interpret variation in calcite chemistry and crystal growth. This change (intensity of red colour) occurs at the edges of the calcite crystals. ICP-MS data shows this variation in colour intensity is observed to correlated with Fe abundance (Section 5.4). The width of the low Fe areas (bright red) is variable with a maximum of 400 µm (**Fig. 14D**) and a minimum of 50 µm (**Fig. 14A**). The cathodoluminescence images show the calcite growth faces, and an abrupt decrease in Fe abundance along this growth face. The sulfide minerals (predominantly chalcopyrite) occur in a line running approximately parallel to this face, and some sulfide grains cross the growth face (**Fig. 14B**), while others do not (**Fig. 14C**). Other chemical variations in the calcite across these zones will be discussed in the calcite trace element section (Section 5.4).

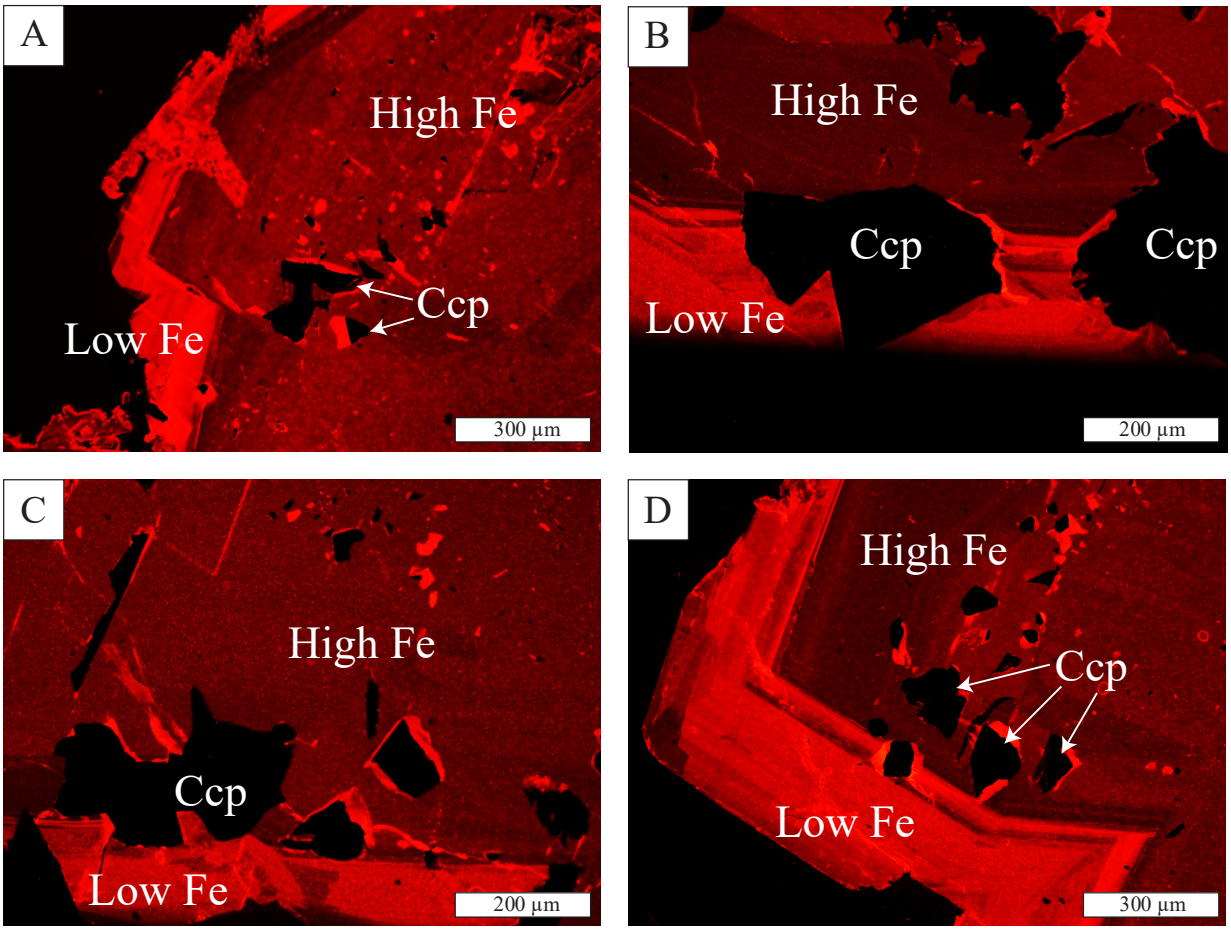

Figure 14: Cathodoluminescence images of calcite from sample 2. *(A)* Thin rim of brighter calcite beyond chalcopyrite grains. *(B)* Bright calcite surrounding chalcopyrite (Ccp) grains. *(C)* Thin rim of brighter calcite at the edge of chalcopyrite grains. *(D)* Corner of calcite crystal with bright red transition beyond chalcopyrite grains.

5.3 Major Element Chemistry

Sulfide Major Elements

Major element compositional data for all analyzed sulfide phases is presented in **Table 1.** Marcasite grains from both *Sample 1* and *Sample 2* were analysed, each with observable differences in bulk composition (**Fig. 15A)**. In *Sample 1*, marcasite has average Cu concentrations of 1.03 wt.% (range of 2.08 wt.% - 0.37 wt. %) and average Ni concentrations of 0.01 wt.% (range of 0.04 wt.% - 0.00 wt.%), whereas *Sample 2* marcasite has an average Cu concentration of 0.54 wt.% (range of 1.48 wt.% - 0.07 wt.%) and an average Ni concentration of 0.25 wt.% (range of 1.43 wt.% - 0.01 wt.%) (**Fig. 15A**). Ni-rich pyrite has large variations in concentrations of Ni, Co, Cu, and Fe (**Fig. 15B)**. Most notably, the maximum concentration of Ni is 18.66 wt.%, while the minimum concentration is 4.44 wt.%. High Co concentrations are present in the Ni-rich sulfides, specifically Ni-rich pyrite (range of 2.96 wt.% - 0.50 wt.%) and by gersdorffite where the average Ni and Co concentrations are 28.17 wt.% (range of 29.80 wt.% - 27.18 wt.%) and 4.22 wt.% (4.69 wt.% - 3.31 wt.%) respectively. Chalcopyrite is very homogeneous throughout both samples, with no notable variations in any major elements.

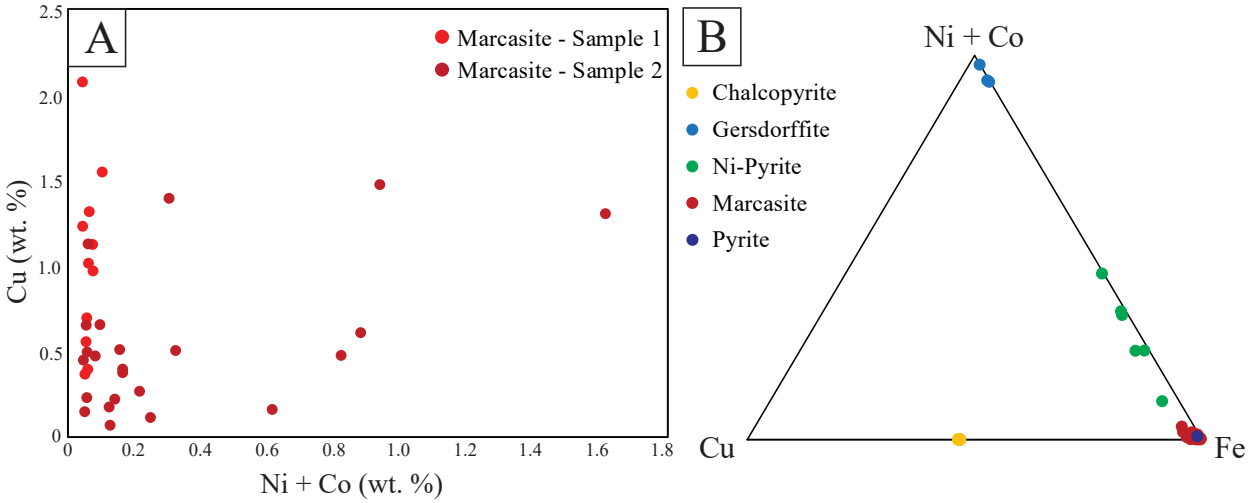

Figure 15: Major element plots for the Ecton sulfides. *(A)* Cu (wt. %) vs. Ni + Co (wt. %) diagram for marcasite from two samples. *(B)* Cu – Fe – (Ni + Co) ternary diagram for all investigated Ecton sulfide minerals.

Calcite and Baryte - Major Elements

Major element data for calcite and baryte are presented in **Table 1.** Overall, the major elements in calcite are compositionally equivalent between the two samples. There is some small

variability in Fe, Mg, and Mn within each sample, and these variations are related to the growth faces shown by the cathodoluminescence images (**Fig. 14**). Fe shows a maximum concentration of 0.46 wt.% and minimum concentration of 0.01 wt.%, Mn shows a maximum concentration of 0.40 wt.% and minimum concentration of 0.01 wt.%, and Mg shows a maximum concentration of 0.32 wt.% and minimum concentration of 0.04 wt.%. Barite in the Ecton samples have very high Sr concentrations (avg. 5.95 wt.%), substituting for Ba (avg. 59.25 wt.%).

5.4 Trace Element Chemistry

Sulfide trace elements

Average trace element data (**Table 2**) for the analysed sulfides from Ecton are plotted in **Figure 16A**. Marcasite, Ni-rich pyrite, and pyrite2 (defined below) have very similar geochemical trends, while chalcopyrite and pyrite1 share similar trends in many trace elements. This includes depletions in Co, As, and Tl, and higher concentrations in Ge and In.

Marcasite and variations of pyrite are plotted in **Figure 16B**. Based on these trace element values, three compositions of pyrite can be distinguished. Pyrite1 (**Fig. 10B**) shows depletion in most trace element abundances compared to the other pyrite variations and marcasite; however it shows enrichment in Zn (avg. 7.44 ppm), Ge (avg. 37.54 ppm), and In (avg. 0.91 ppm). Pyrite 2 (**Fig. 10D**) has a similar trace element trend as does marcasite, with the notable exceptions being enrichment in Cu, and depletion in Sn. Marcasite and Ni-rich pyrite also have high Cu concentrations, average of 3,773 ppm and 8,484 ppm respectively, but pyrite 2 exceeds these values with 22,317 ppm. Ni-rich pyrite (**Fig. 10A, F**) has the highest concentrations of Ni, Co and Se, 123,585 ppm, 17,413 ppm, and 318 ppm respectively, but also has the lowest concentration of In and Sn.

S/Se ratios are plotted in **Figure 16C**. An overall trend for the sulfides plotted shows that higher Co concentrations lead to a larger range in S/Se ratios. Chalcopyrite, with the lowest Co concentration, has a relatively narrow range between 20,850 and 113,730. Marcasite has a range of 2,811,146 to 15,321, while Ni-rich pyrite has a range of 59,824 to 977.

Table 1: Overview of select EPMA data for analysed minerals from Ecton samples (average values)

Mineral	Sample #	*n*	S (wt. %)	Bi (wt. %)	Zn (wt. %)	Te (wt. %)	Pb (wt. %)	Sb (wt. %)	Fe (wt. %)	Co (wt. %)	Ni (wt. %)	Cu (wt. %)	Se (wt. %)	As (wt. %)	Cd (wt. %)
Chalcopyrite	*1*	37	35.29 ± 0.17	0.04 ± 0.03	0.01 ± 0.02	0	0	0	30.42 ± 0.18	0.03 ± 0.01	0	34.88 ± 0.17	0	0	0
	2	25	35.55 ± 0.16	0.03 ± 0.03	0.00 ± 0.01	0	0	0	30.43 ± 0.24	0.03 ± 0.01	0	34.90 ± 0.19	0	0	0
Marcasite	*1*	11	53.50 ± 0.19	0.05 ± 0.04	0.01 ± 0.02	0	0	0	45.67 ± 0.54	0.06 ± 0.01	0.01 ± 0.01	1.03 ± 0.52	0	0.08 ± 0.13	0
	2	23	53.44 ± 0.46	0.05 ± 0.03	0.01 ± 0.01	0	0.01 ± 0.04	0.01 ± 0.01	45.70 ± 0.62	0.07 ± 0.04	0.25 ± 0.36	0.54 ± 0.41	0	0.29 ± 0.47	0
Pyrite1	*2*	2	53.77 ± 0.05	0.03 ± 0.02	0	0	0	0.01 ± 0.01	46.68 ± 0.20	0.05 ± 0.01	0	0.05 ± 0.04	0	0	0
Ni-rich Pyrite	*2*	6	53.33 ± 0.32	0.06 ± 0.04	0	0.01 ± 0.01	0.01 ± 0.03	0	34.41 ± 5.10	1.56 ± 0.89	11.94 ± 4.94	0.86 ± 0.62	0	0.49 ± 0.09	0
Galena	*1*	2	13.48 ± 0.01	0.20 ± 0.02	0	0.03 ± 0.02	85.69 ± 0.44	0.01 ± 0.01	0.01 ± 0.01	0	0	0	0	0	0
	2	2	13.60 ± 0.13	0.16 ± 0.05	0	0.02 ± 0.01	87.22 ± 0.27	0	0.54 ± 0.32	0	0	0.40 ± 0.09	0	0	0
Gersdorffite	*2*	3	15.18 ± 7.64	0.01 ± 0.02	0	0	0.02 ± 0.03	0.03 ± 0.03	1.71 ± 0.85	4.22 ± 0.79	28.17 ± 1.42	0.08 ± 0.06	0.04 ± 0.04	45.30 ± 3.37	0

			SiO_2 (wt.%)	Al_2O_3 (wt.%)	FeO (wt.%)	MnO (wt.%)	MgO (wt.%)	CaO (wt.%)	SrO (wt.%)	BaO (wt.%)	Na_2O (wt.%)	K_2O (wt.%)	P_2O_5 (wt.%)	SO_3 (wt.%)	CO_2 (wt.%)
Calcite	*1*	60	0.01 ± 0.01	0	0.11 ± 0.10	0.15 ± 0.09	0.15 ± 0.04	56.41 ± 0.45	0	0.01 ± 0.01	0.03 ± 0.06	0.02 ± 0.02	0.02 ± 0.02	0.01 ± 0.02	43.72 ± 0.10
	2	60	0.01 ± 0.02	0	0.15 ± 0.07	0.16 ± 0.05	0.19 ± 0.06	55.92 ± 0.41	0	0.01 ± 0.02	0	0.02 ± 0.01	0.02 ± 0.02	0.01 ± 0.01	43.82 ± 0.09
Baryte	*1*	7	0	0.06 ± 0.02	0.10 ± 0.06	0	0	0.86 ± 0.26	5.95 ± 0.62	59.25 ± 0.95	0.07 ± 0.02	0.03 ± 0.02	0	35.54 ± 0.14	0

Table 2: Overview of LA-ICP-MS data for analysed sulfides from Ecton samples (average)

Mineral	Sample #	*n*	Co (ppm)	Ni (ppm)	Cu (ppm)	Zn (ppm)	Ge (ppm)	As (ppm)	Se (ppm)	Ag (ppm)	In (ppm)	Sn (ppm)	Sb (ppm)	Tl (ppm)	Pb (ppm)
Chalcopyrite	*1*	22	0.49 ± 0.19	0.15 ± 0.12	346162.11 ± 8647.43	10.87 ± 5.74	324.99 ± 155.24	2.31 ± 3.26	8.28 ± 3.38	4.11 ± 1.21	0.71 ± 0.42	1.39 ± 0.70	6.02 ± 8.09	0.09 ± 0.06	1.22 ± 1.12
	2	16	0.50 ± 0.43	0.26 ± 0.31	354494.95 ± 7663.25	12.83 ± 6.22	100.93 ± 63.50	1.39 ± 1.81	6.83 ± 4.03	1.07 ± 0.75	1.07 ± 0.34	0.62 ± 0.50	11.06 ± 0.50	0.15 ± 0.18	7.05 ± 10.68
Marcasite	*2*	25	98.49 ± 98.40	1991.33 ± 1331.16	3773.40 ± 2433.03	8.56 ± 29.81	4.72 ± 8.57	2253.08 ± 1102.58	9.51 ± 8.65	28.50 ± 16.45	0.21 ± 0.18	0.60 ± 0.41	155.68 ± 102.19	5.14 ± 6.34	533.53 ± 317.96
Pyrite1	*2*	2	0.36 ± 0.12	8.03 ± 5.75	332.02 ± 29.68	7.44 ± 3.05	37.54 ± 7.07	3.06 ± 2.28	8.53 ± 0.48	1.30 ± 0.03	0.91 ± 0.03	0.62 ± 0.00	3.53 ± 0.84	0.31 ± 0.13	6.65 ± 0.86
Pyrite2	*2*	1	2.81	509.92	22317.20	0.76	2.56	137.80	5.30	7.18	0.97	0.01	59.23	8.03	82.80
Ni-rich Pyrite	*2*	4	17413.02 ± 6781.17	123585.93 ± 39523.45	8484.87 ± 2931.59	0.37 ± 0.46	2.04 ± 1.28	4779.30 ± 1153.74	318.90 ± 202.84	39.93 ± 6.43	0.02 ± 0.00	0.01 ± 0.00	51.17 ± 11.44	6.09 ± 0.36	421.00 ± 123.52

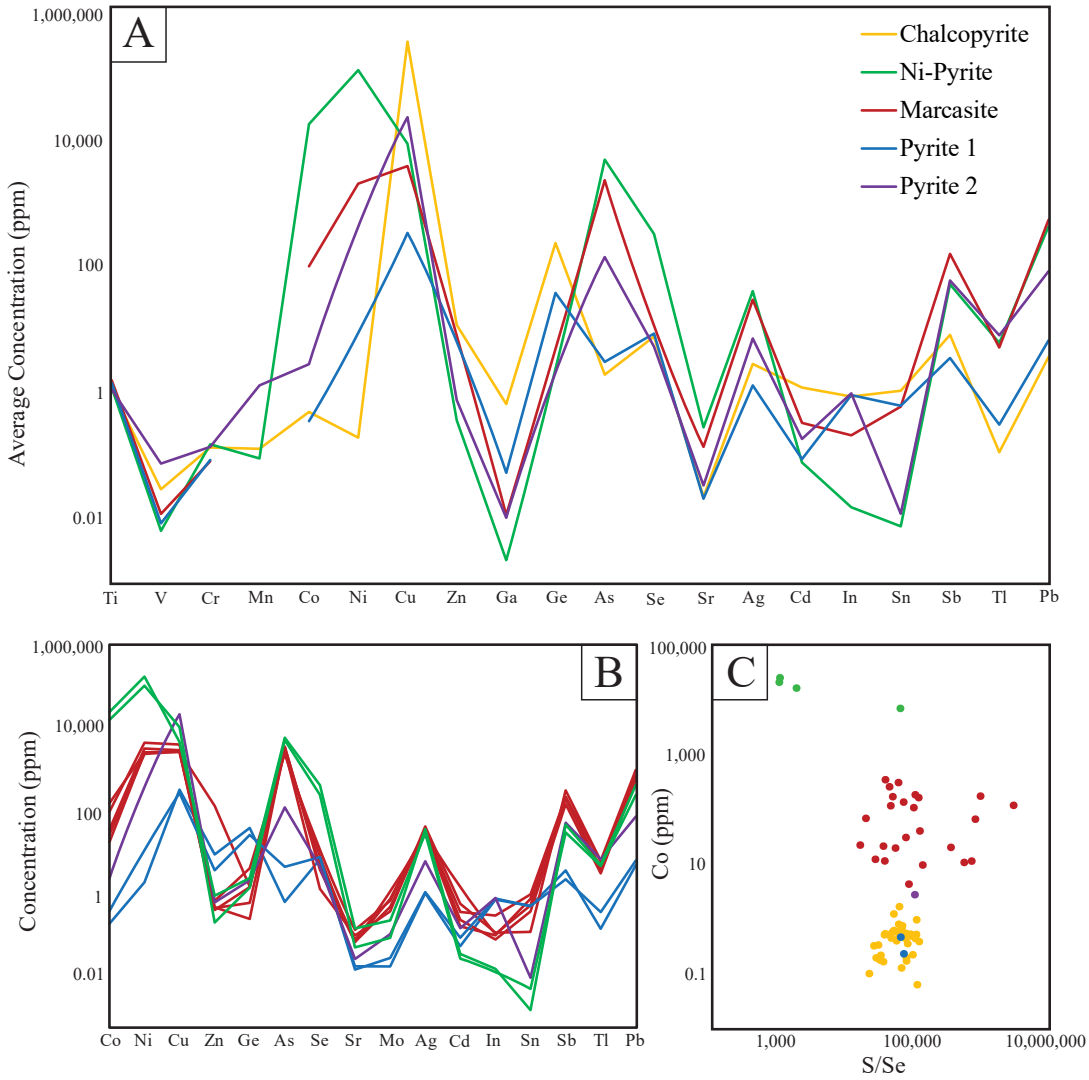

Figure 16: Trace element plots for the sulfides from Ecton. *(A)* Trace element average concentrations for sulfide minerals. *(B)* Selected trace element concentrations for all pyrite variations and marcasite. *(C)* Co (wt. %) vs. S/Se ratio for sulfide minerals. Legend in *(A)* applies to all panels.

Trace element abundances in calcite

Calcite trace element data, analysed as continuous line analyses, are shown in **Figure 17**. These plots show REE + Y chondrite normalized data along traverses through the calcite.

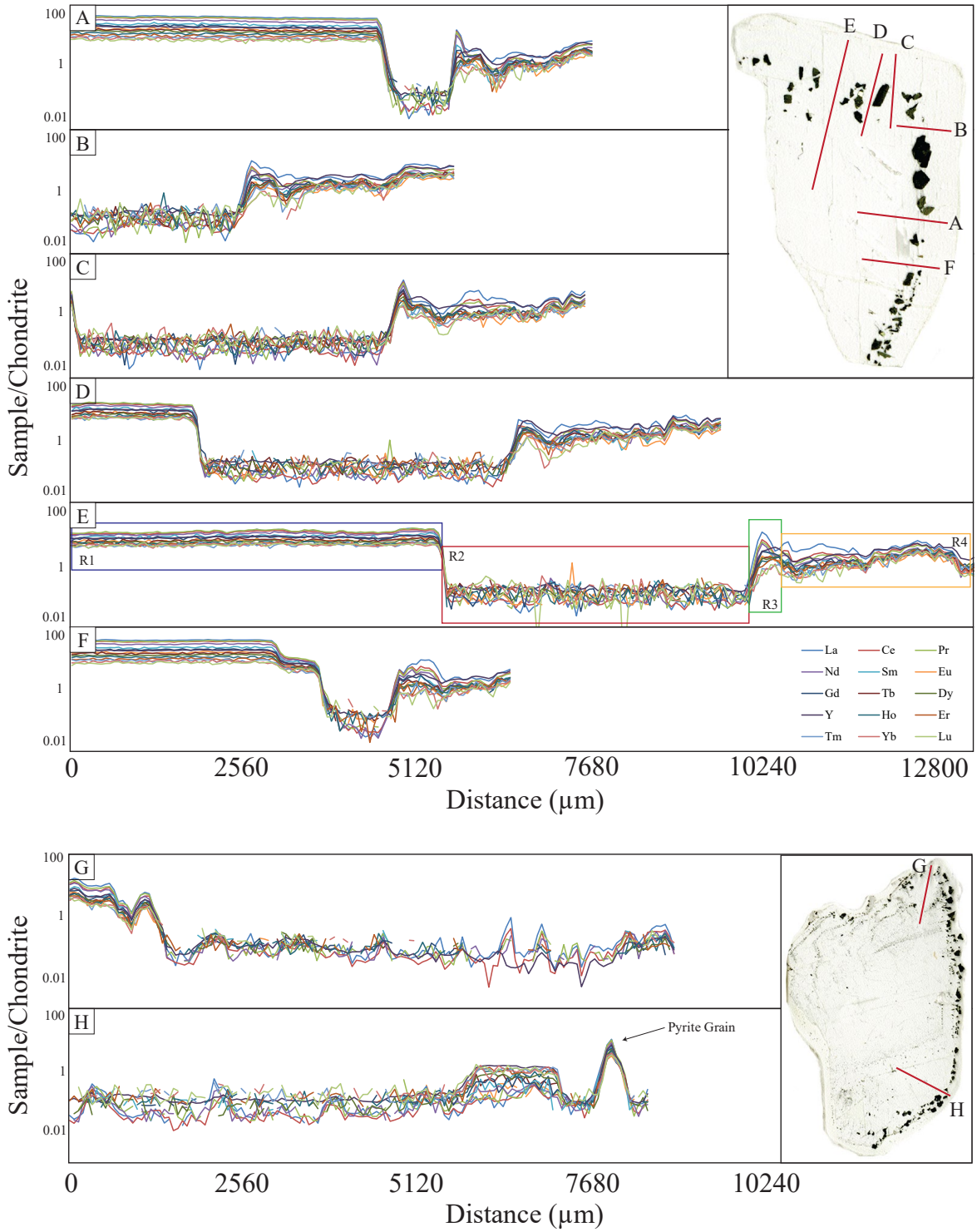

Figure 17: Continuous line analysis trace element data for REEY. Data are presented as traverses beginning at the outside of the thin section and moving towards the center. Boxes A-F correspond to traverses on thin section 1. Boxes 7-8 correspond to traverses on thin section 2. Legend applies to all data in figure. Chondrite values from *Taylor and McLennan, 1985*.

Chondrite-normalized REE + Y profiles for Sample 1 (Fig. **17A–F**) define four distinct zones of geochemical variation within the calcite crystal (R. A-R. D; **Fig. 17E**). Region A corresponds to the center of the calcite crystal and is characterized by elevated REE + Y concentrations. A decrease in these concentrations' marks Region B, the region of calcite hosting chalcopyrite grains, which displays the lowest REE + Y values of all four regions. Region C is the narrowest region, (~100–200 µm) and REE + Y concentrations initially increase before declining toward Region D. The region on the outermost part of the calcite, Region D, occurs exhibits the greatest variability in REE + Y concentrations. In contrast, Sample 2 (**Fig. 17G–H**) does not display this four-region pattern. REE + Y concentrations remain consistently depleted throughout the center of the calcite, with increases in concentration close to the calcite crystal edge.

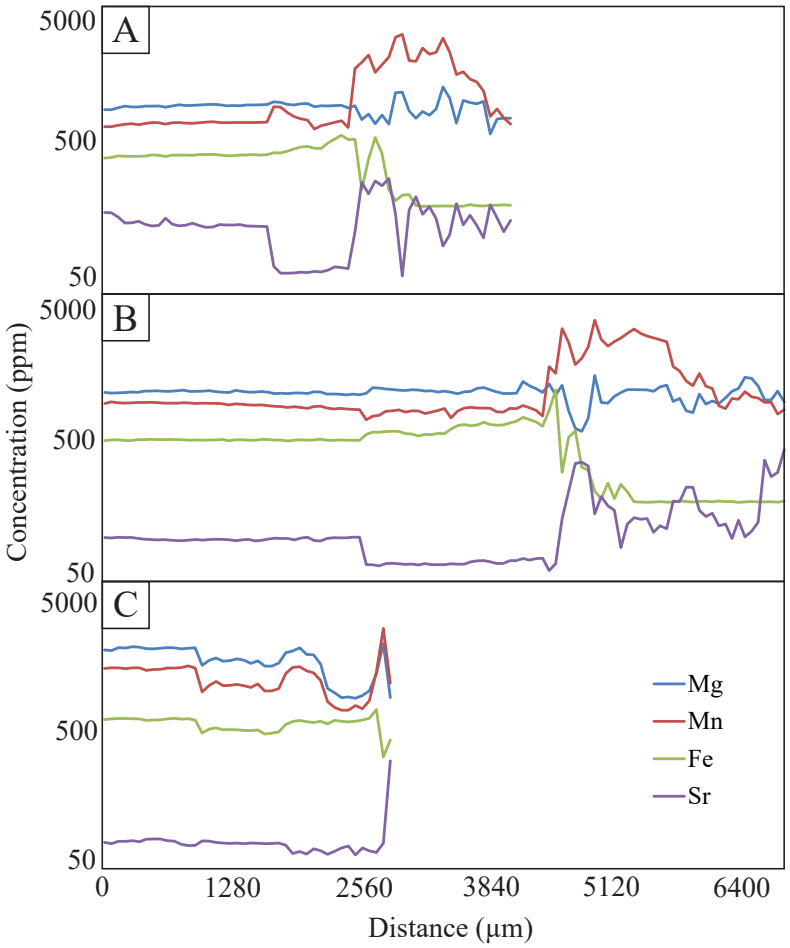

Figure 18: Trace element data plots for Mg, Mn, Fe, and Sr. Spots completed along line traverses. Line 1, 5, 8 referring to figure 9.

Analyses collected along three traverses (**Fig. 18A–C**) show that Mg, Mn, Fe, and Sr in Sample 1 follow trends comparable to the REE + Y data and can likewise be grouped into the same four regions. Region A, at the center of the calcite crystal, contains uniform concentrations of all four elements. In Region B, which hosts the chalcopyrite grains, Mg, Mn, and Fe remain similar to Region A, whereas Sr decreases (avg. 62 ppm). Region C is marked by pronounced increases in Fe (1066 ppm) and Sr (323 ppm) and a decrease in Mn. Both Fe and Sr show an initial minor increase, followed by depletion prior to their major increase. Region D displays substantial variability in concentrations of Mg, Mn, and Sr, while Fe remains consistently depleted (avg. 170 ppm), corresponding to the Fe-poor zone observed in cathodoluminescence (**Fig. 14**). Similarly with the REE + Y data, Sample 2 does not exhibit four distinct regions. Major-element concentrations remain uniform in the calcite interior, while the crystal edge shows sharp positive peaks followed by declining values. Fe displays an inverse relationship to Mn across all three analysis lines.

5.5 Sulfur Isotopes

Six chalcopyrite samples were taken from both *Sample 1* and *Sample 2* (**Fig. 19**). The chalcopyrite grains were taken from both the exterior of calcite crystals, as well as grains from the interior of the calcite. *Sample 2* has lighter $\delta^{34}S$ values with an average of -16.66‰, while *Sample 1* has an average of -15.32‰. Within each sample, there is variation based on the location that the chalcopyrite was sampled from. Grains taken from the exterior of the calcite of *Sample 1* have lighter values; three samples have an average of -15.55‰, versus three samples from the interior have an average of -15.09‰. The five samples from the exterior of *Sample 2* have an average of -16.76‰, while the one sample from the interior has a value of -16.13‰.

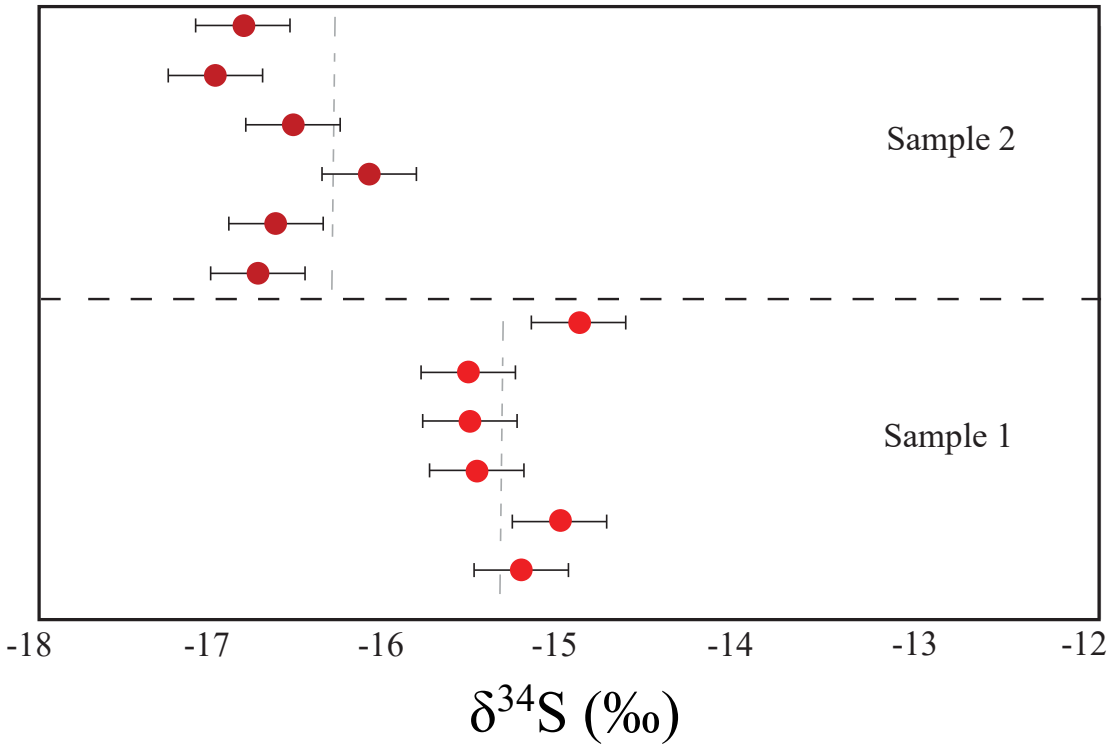

Figure 19: $\delta^{34}S$ values for chalcopyrite in the Ecton samples. Chalcopyrite grains separated by vertical dashed line, samples from the exterior on the left, and samples from the interior on the right.

6. Discussion

6.1 Geochemical characteristics of the Ecton mineralisation

Sample heterogeneity

Although the number of samples available for study from Ecton Mine is limited, the three samples used in this study display clear differences in mineral composition, texture and geochemistry. *Sample 2* contains the more diverse mineral assemblage and is the only sample that contains the Ni-, As-, and Pb-bearing phases. In addition to calcite, *Samples 1* predominantly comprises chalcopyrite, along with minor amounts of pyrite2. **Figure 20** shows the abundances of trace element concentrations in chalcopyrite from both *Sample 1* and *Sample 2*. Although many trace elements are of similar concentrations, there are differences in elements such as Mn, Ge, Ag, and Cd. *Sample 2* has higher concentrations of Mn (avg. 0.43 ppm *vs*. 0.09 ppm in *Sample 1*) and Ag (avg. 4.1 ppm *vs*. 1.1 ppm in *Sample 1*), while *Sample 1* has higher concentrations of Cd (avg. 1.9 ppm *vs*. 0.28 ppm in *Sample 2*) and Ge (avg. 325 ppm *vs.* 100 ppm in *Sample 2*). Texturally, both *Sample 1* and *Sample 2* have euhedral chalcopyrite grains

aligned parallel to the crystal face of the calcite crystal, but *Sample 2* has much smaller, anhedral chalcopyrite grains disseminated throughout calcite crystals.

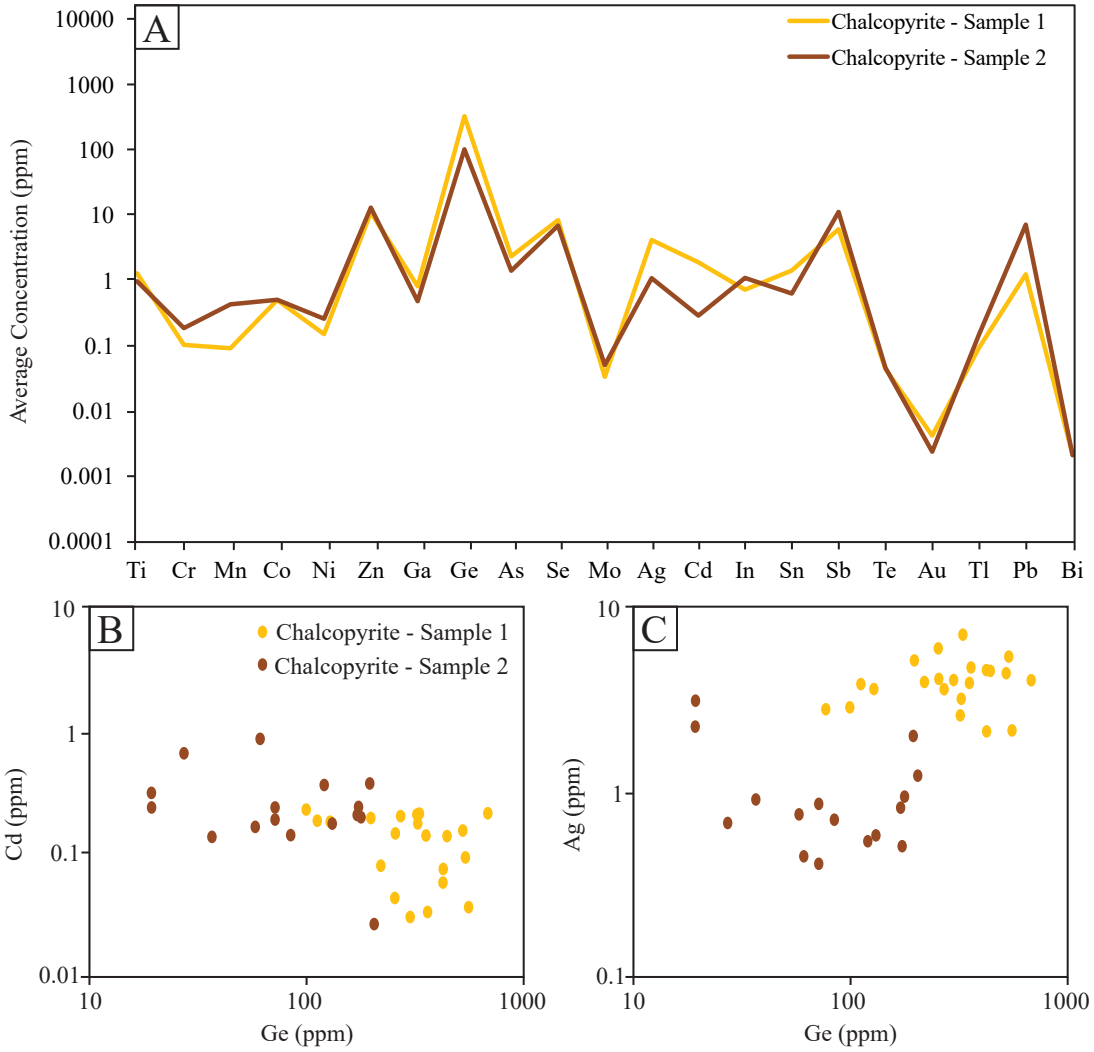

Figure 20: *(A)* Selected trace elements plot for the average concentrations (ppm) of chalcopyrite from *Sample 1* and *Sample 2*. *(B)* Binary plot of Cd (ppm) vs. Ge (ppm) for chalcopyrite from *Sample 1* and *Sample 2*. *(C)* Binary plot of Ag (ppm) vs. Ge (ppm) for chalcopyrite from *Sample 1* and *Sample 2*.

One possible explanation for the heterogeneity displayed by these samples is metal zonation within the Ecton deposit. Although the occurrence of metal zonation at Ecton is difficult to substantiate based on the limited number of samples in this study as well as the lack of *in-situ* material in general, some degree of zonation has already been shown in the South Pennine Orefield where sphalerite was documented as being more common at greater depth (Ford and Worley, 2016), as well on Ecton Hill where the Clayton Pipe was originally mined for lead

before encountering higher concentrations of copper and zinc ore at depth (Ford, 2000). Geochemical comparisons to global MVT deposits that exhibit zonation (e.g. Nayongzhi Deposit, Wei *et al.*, 2025; Lisheen Deposit, Frenzel *et al.*, 2025) can help provide useful insights, for example, the Nayongzhi Deposit in southwest China displays trace element variations in sphalerite related to the proximity of mineralisation to the feeder fault. This includes Mn, Fe, Cu, Ga, Ge and In decreasing in concentration with increased distance from the feeder, and Cd increasing in concentration with greater distance (Wei *et al.*, 2025). The chalcopyrite from Ecton has variations in some of these elements between the two samples, with *Sample 2* having higher concentrations of Mn whereas *Sample 1* has higher concentrations of Cd. Also notable is the higher abundance of Fe-sulfides in *Sample 2*, which could indicate higher concentrations of Fe in this sample, as well as the higher concentration of Cu mineralisation within this sample. These observations could suggest a spatial variation in the samples, with *Sample 2* being closer to the feeder fault of the hydrothermal fluid, and *Sample 1* being more distal.

Hydrothermal vs. magmatic mineralisation

Recent studies (Kraemer et al, 2019; Dempsey *et al.*, 2021) suggest mineralisation in the Alston Block in the nearby North Pennine Orefield is related to mantle-magmatism, in contrast to previous interpretations invoking F-rich fluid(s). Chalcopyrite geochemistry may differentiate between deposit types, with normalized Cd-Se-Ni ternary diagrams (**Fig. 21**) differentiating between fluid sources (Tang *et al.*, 2025). Ecton chalcopyrite is sufficiently rich in Se to make it difficult to distinguish between a magmatic or hydrothermal origin. Indeed, close examination of **Figure 21** shows the resulting data points plot in both hydrothermal and magmatic fields.

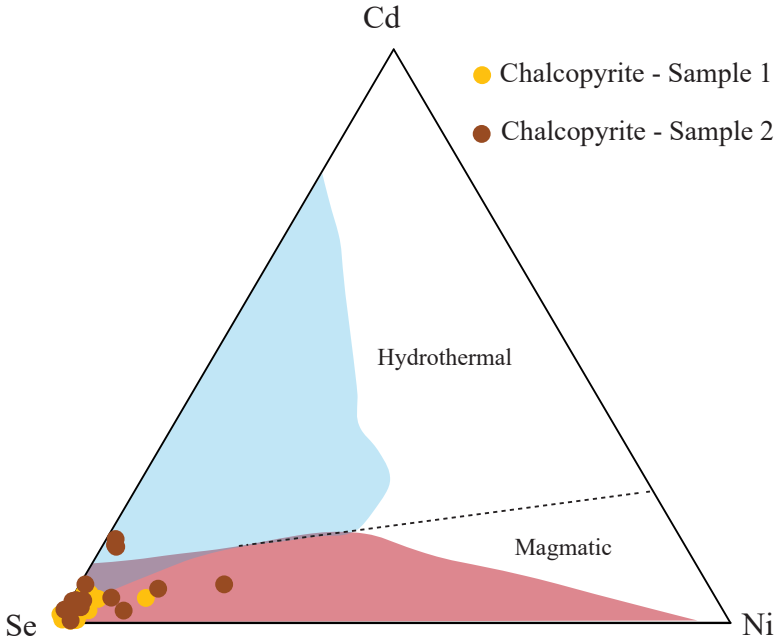

Figure 21: Cd-Se-Ni ternary diagram with global fields for magmatic and hydrothermal origins of chalcopyrite. Ecton chalcopyrite from both *Sample 1* and *Sample 2* plotted. Magmatic and hydrothermal fields from *Tang et al., 2025*.

Chalcopyrite from different deposit types displays a wide range of $\delta^{34}S$ values based on the source of the sulfur, potentially allowing differentiation of metal sources. Chalcopyrite from magma-related deposits commonly displays $\delta^{34}S$ values that reflect mantle-derived sulfur ($\delta^{34}S \sim 0‰$), with values varying with different styles of crustal contamination (Tang *et al.*, 2025). The $\delta^{34}S$ values for chalcopyrite from Ecton are comparatively light (avg. -16.7‰ and -15.3‰), so the sulfur is unlikely to be derived from a magmatic source.

The lack of evidence to support a magmatic origin for Ecton mineralisation, and the apparent lack of associated magmatic bodies suggest copper mineralisation resulted from hydrothermal fluids, and with sulfur derived from a sedimentary source.

Comparison of geochemical data to global deposits

Copper is typically a trace component in most MVT deposits (Leach *et al.*, 2010); however, it can occur in significant quantities in some districts (e.g. Irish Midlands, Hitzman and Beaty, 1996; Viburnum Trend, Cavender *et al.*, 2016). Within the South Pennine Orefield, however, the elevated abundances of copper observed at Ecton are unique. The reasons for this remain poorly understood. (e.g., Ford and Quirk, 1995; Ford, 2000).

Comparisons of Ecton chalcopyrite trace element compositions to those of six global copper ore deposit types show no clear correlation (**Fig. 22**). However, relative depletions in Cr, Mn, Cd, Ag, and Bi are ubiquitously observed.

The depletion of Bi in chalcopyrite is consistent with the observed occurrence of phases that preferentially incorporate Bi, such as sphalerite and galena. This relationship is also observed in chalcopyrite in zoned Cu-Pb-Zn ore at the Mount Isa deposit (Cave *et al.*, 2020). For Ecton samples, the low abundances and small grain sizes of galena precluded the collection of trace element data by LA-ICP-MS; however, analyses of galena by EMPA indicates an average of 0.18 wt.% Bi. The high and low abundances of Bi in galena and chalcopyrite (compared to concentrations in global deposit types), respectively, could be attributed to the co-crystallization of the two phases. Elements such as Co, Se, Ag, and Bi have been shown to be preferentially incorporated into galena (George *et al.*, 2016). The geochemical trends of the chalcopyrite from Ecton are inconsistent with magmatic-sulfide deposits (MSD) and volcanogenic massive sulfide deposits (VMS), both of which have higher concentrations of Cr, Co, Ni, and Te. Better agreement is observed between the chalcopyrite from Ecton and both iron-oxide-copper-gold (IOCG) and sediment-hosted stratiform copper (SSC) deposits. However, Ecton is mineralogically inconsistent with IOCG deposits, lacking iron oxides and gold. Ecton also contains marcasite, representing fluid temperatures that are typically lower than the hydrothermal

fluids that form IOCG deposits (Skirrow, 2022). SSC deposits are typically hosted in beds of reduced shale, siltstone, or sandstone whereas the copper mineralisation at Ecton is hosted by limestone. The copper could, however, be sourced in similarly to SSC deposits, as their metals are commonly stripped from red-bed sequences or basaltic rocks (Hayes *et al.*, 2010) and the source of copper at Ecton has not been determined. Based on the large differences in geochemical characteristics compared to global deposit types shown in **Figure 22** and lack of other supporting evidence, the copper at Ecton is considered unlikely to represent an IOCG, magmatic sulfide, porphyry-copper, VMS, SSC, or SEDEX deposit.

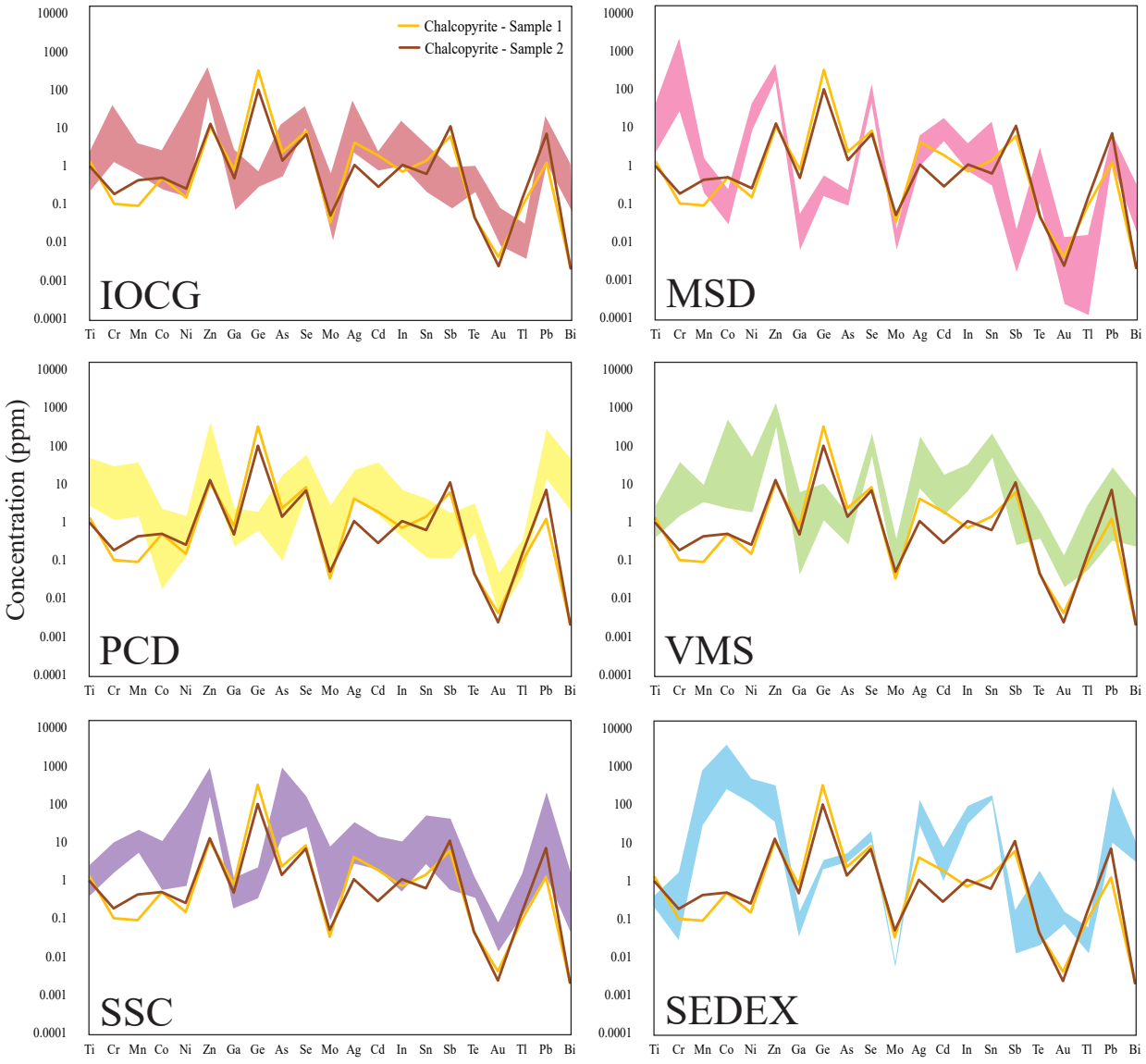

Figure 22: Selected trace elements plot for the average concentrations (ppm) of chalcopyrite from *Sample 1* and *Sample 2* with global fields for six ore deposit types that typically host large quantities of chalcopyrite. Global fields

from *Tang et al., 2025*. IOCG: Iron-oxide-copper-gold; MSD: Magmatic sulfide deposit; PCD: Porphyry copper deposit; VMS: Volcanogenic massive sulfide; SSC: Sediment-hosted stratiform copper; SEDEX: Sedimentary exhalative.

Ge enrichment of the Ecton chalcopyrite

The measured concentrations of Ge in chalcopyrite average 325 ppm (S.D. 1σ = 155.2, n = 22) in *Sample 1* (maximum of 677 ppm) and 100 ppm (S.D. 1σ = 63.5, n = 16) in *Sample 2* (maximum of 203 ppm). In deposits that have significant amounts of Ge, it is mined in the form of Ge-minerals; e.g. at the Kipushi (Intiomale and Oosterbosch, 1974) and Tsumeb (Lombaard *et al.*, 1986) deposits, or from sphalerite into which Ge preferentially substitutes (Niu *et al.*, 2026). The crystal structures of both sphalerite and chalcopyrite are based on tetrahedrally-coordinated cations. Thus, the substitution of Ge^{4+} into chalcopyrite may also occur (e.g. Barrigão Cu deposit; Bellisont *et al.*, 2019). Recent studies have shown Ge-enrichment of chalcopyrite in low-temperature hydrothermal deposits, such as at the Lisheen Irish-Type MVT deposit (Frenzel *et al.*, 2025) and the Kuperschiefer deposit (Foltyn *et al.*, 2025). **Figure 23** compares chalcopyrite from Ecton to the latter deposit.

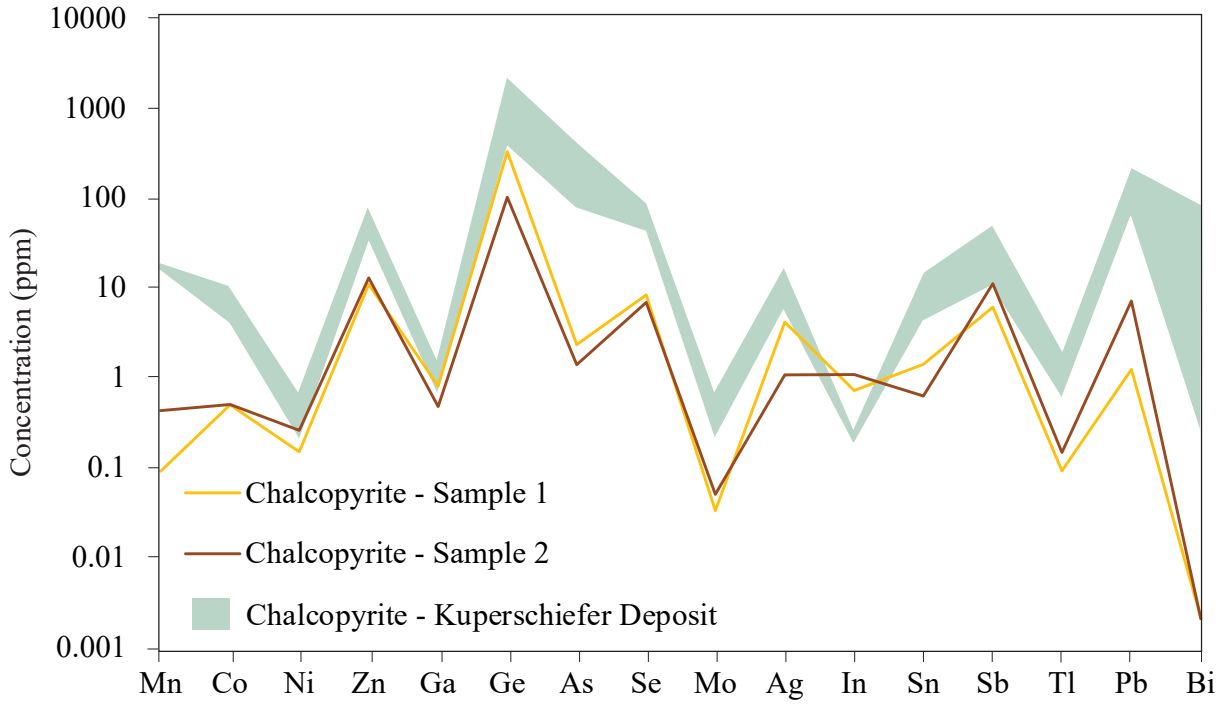

Figure 23: Selected trace element plot for the average concentrations (ppm) of chalcopyrite from *Sample 1* and *Sample 2* with field for the Kuperschiefer Deposit chalcopyrite from *Foltyn et al., 2025*.

Although the chemical structure of chalcopyrite allows for the substitution of Ge^{4+}, the enrichment is also dependent on the sulfur fugacity, where high or intermediate sulfur activity

leads to the formation of Ge-rich minerals, as well as the incorporation of Ge into sulfide phases like sphalerite and chalcopyrite (Foltyn *et al.*, 2025; Holl *et al.*, 2007). The high concentration of Ge in the chalcopyrite from Ecton suggests that there was at least an intermediate sulfidation state, allowing for increased concentration of Ge in the mineralising fluid. Furthermore, chalcopyrite is much more common in intermediate sulfidation systems than the low-sulfidation systems that characterise typical MVT deposits (Wang *et al.*, 2019).

Sulfide chemical zonation

Oscillatory chemical zonation of single crystals is commonly displayed by sulfides in hydrothermal deposits. Oscillatory zonation of As, Cu, Ni, and Co occur in *Sample 2* from Ecton in both marcasite (**Fig. 12C, E**) and pyrite2 (**Fig. 12B**). Qui and Zhou (2025) determined that oscillatory zonation cannot develop in turbulent hydrodynamic conditions and that episodic fluid changes would result in the suppression of oscillatory zonation in pyrite. Instead, zonation is attributed to local chemical disequilibrium at mineral-fluid interfaces (Qui and Zhou, 2025*)*. The turbulent hydrodynamic conditions of sedimentary environments also make oscillatory zonation of sedimentary pyrite uncommon (Qui and Zhou, 2025). The observation of oscillatory zonation of As, Cu, Ni, and Co in marcasite indicates that these elements were present in the hydrothermal fluid during the mineralisation process. In the samples from this study, pyrite1 is not observed to have oscillatory zonation, and instead has zonation of As, Cu, and Ni along its outer grain boundaries (**Fig. 12D**). The variance in zonation style could be due to several factors including, changes in the hydrodynamic conditions, fluid composition changes, or the timing of mineralisation of pyrite1 compared to the rest of the mineral assemblage. Given that pyrite1 is often observed partially surrounded by marcasite (**Fig. 10B**), it is more likely an early phase and possibly sedimentary.

The oscillatory zonation commonly observed in marcasite and pyrite2 probably relate to local chemical disequilibrium at the crystal growth face and not to episodic changes of the mineralizing fluid composition at the ore deposit scale. Marcasite is a common sulfide mineral throughout the South Pennine Orefield (Ford and Worley, 2016) and given the presence of galena and sphalerite at Ecton, it is reasonable to assume that the marcasite present at Ecton is a product of the same mineralising event as the larger orefield. This signifies that the hydrothermal fluid responsible for the mineralisation across the South Pennine Orefield contained these same elements that are concentrated in higher quantities at Ecton

6.2 Fluid mechanisms and provenance

Variations in regions of calcite

Minor amounts of rare earth elements may substitute for Ca^{2+} in the calcite crystal structure (Bau, 1991). Examination of REE abundances as a function of calcite growth in hydrothermal systems may allow the identification of ore stages, fluid mixing and petrogenesis (e.g. Liu *et al.*, 2020; Myint *et al.*, 2022; Wang *et al.*, 2020). The calcite crystals from Ecton lack evidence for dissolution or re-precipitation, suggesting that the growth of the crystals was linear. Chondrite-normalized, continuous line REEY (rare earth elements + Yttrium) analyses in Ecton calcite are shown in **Figure 24**: based on REEY abundances, four distinct regions are identified. These regions relate spatially to the chalcopyrite mineralising event and can broadly be divided as pre-, syn-, and post-mineralisation calcite growth. These regional variations are best displayed by the REEY patterns of the calcite in *Sample 1* and the following definitions are based on this sample. The heterogeneity of the REEY patterns shown in *Sample 2* (**Fig. 26**) are discussed as follows.

Region A: pre-mineralisation

This region is closest to the center of the calcite crystal and defined by the highest REEY concentrations and least variation in the calcite (**Fig. 24A**). Light rare earth elements (LREE) are enriched relative to HREE, with a distinctive positive Y anomaly and negative Eu anomaly. This region is inferred to be pre-mineralisation because there are no observable chalcopyrite grains here, and assuming simple core-to-margin growth of the calcite crystal, was formed before mineralisation.

Region B: syn-mineralisation

In Region B, HREE are enriched relative to LREE (*e.g.* high Yb/La ratio; **Fig. 25A**) and the lowest concentrations of REEY along the profile are observed. This region is syn-mineralisation with respect to chalcopyrite. In other hydrothermal deposits globally, the crystallization of syn-mineralization calcite can be identified by variations in REE concentrations and patterns (*e.g.* Wang *et al.*, 2020; Myint *et al.*, 2022), as seen with the transition between Region A and Region B. This has been explained as either: (1) multiple fluid sources during different stages of the system; (2) mixing of fluid during mineralisation; or (3) pressure-temperature changes causing variable partitioning of REE between the calcite and fluid. HREE enrichment in Region B is consistent with the mixing of the pre-mineralisation fluid, (enriched in LREE) with a REE-depleted hydrothermal fluid that carried the metals. This resulted in a diluted REE signature and HREE enrichment (as described by Sanchez *et al.*, 2010). The diluted REE signature in Region B is not due to incorporation of REE into the sulfide phases present in this region, as sulfides rarely incorporate significant amounts of REE. Although a full REE data set was not captured on the sulfides from Ecton, concentrations for La, Gd, and Yb corroborate that the sulfides did not incorporate significant amounts of REE during precipitation (**Table A10**).

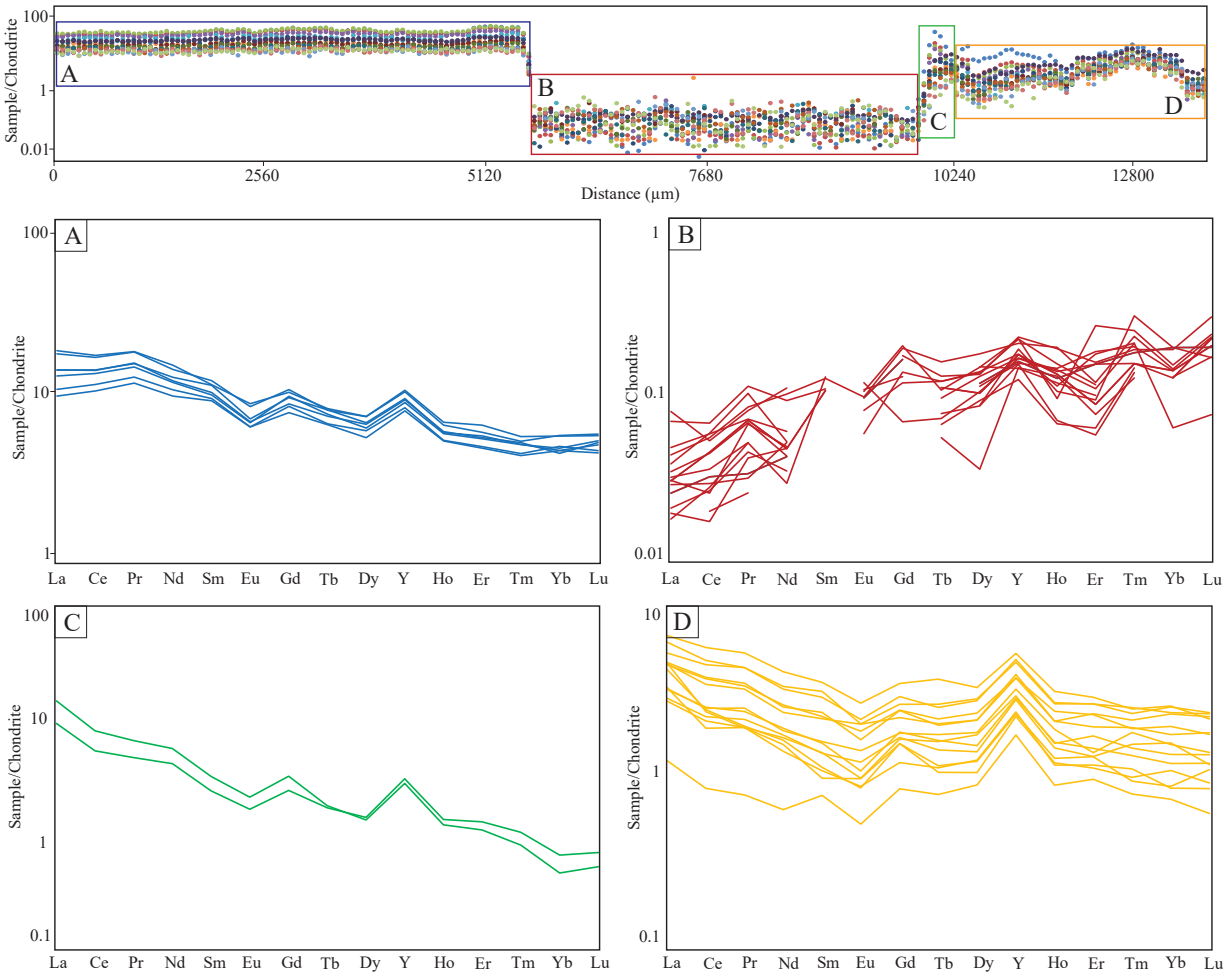

Figure 24: Chondrite normalized REEY trace element patterns for spot analyses along continuous line analysis in *Sample 1* calcite. Chondrite values from *Sun and McDonough, 1989.* Total REEY traverses (from **Fig. 17**) used as reference for Region A-C boundaries.

Regions C and D: post-mineralisation

Region C has the highest LREE enrichment relative to both HREE and MREE (middle rare earth elements; Sm, Eu, Gd, , Tb, Dy, and Y) (Low Yb/La ratio in **Fig. 25A**, and high La/Ho ratio in **Fig. 25B**). Region D is LREE-enriched relative to HREE (Yb/La ratio in **Fig. 25A**) and has lower concentrations of REE compared to the Region A calcite. Region D also has the least consistent and largest variation in REEY values (**Fig. 24D**). Both Regions C and D can be interpreted as post-mineralisation as no chalcopyrite is hosted here. Both Region C and Region D have positive Y and Gd anomalies, similar to what is exhibited by Region A. Positive Y and Gd anomalies are generally attributed to seawater interaction (*Bau, 1996; Jiu et al., 2025*) and the

presence of these anomalies in both pre- and post-mineralisation calcites suggest that the hydrothermal system at Ecton had a seawater component throughout the whole mineralisation process.

Y/Ho ratios

Under most conditions Y behaves similarly to Ho (Both have +3 equivalence charges and ionic radii of 0.898 Å and 0.897 Å, respectively (Gagne and Hawthorne, 2024). However, during hydrothermal processes, Y can be fractionated from Ho because the former more easily forms stable complexes with important hydrothermal ligands like F^-, and CO_3^{2-} (Bau and Dulski, 1995). This process allows for interpretation of geological processes associated with hydrothermal activity based on the deviation from typical chondritic Y/Ho values of ~28 (Bau and Dulski, 1999). The Y/Ho ratios from the pre-mineralisation Region A calcite have a very narrow range (35 – 39; **Fig. 25B**), while the syn-mineralisation Region B calcite has the widest range (23 – 54; **Fig. 25B**). The most likely process that caused the change from a very narrow Y/Ho ratio range to a much larger range is the mixing of multiple fluids, as demonstrated by Liu *et al.*, 2020. This suggestion would also explain the moderately wide range of Y/Ho ratios in the post-mineralisation calcite (38 – 60; **Fig. 25B**), resulting from the mixing of a narrow Y/Ho ratio fluid and a wide Y/Ho ratio fluid. The Yb/Ca ratio (**Fig. 25A**) also shows that Regions A, C and D fall within the hydrothermal field, whereas Region B falls within the sedimentary field. Given that Region B is the host calcite for the chalcopyrite mineralisation, it is possible that these elements were scavenged from large volumes of sediment in the basin, and this decoupling from the other calcite regions suggests mixing of multiple fluids during the mineralisation process.

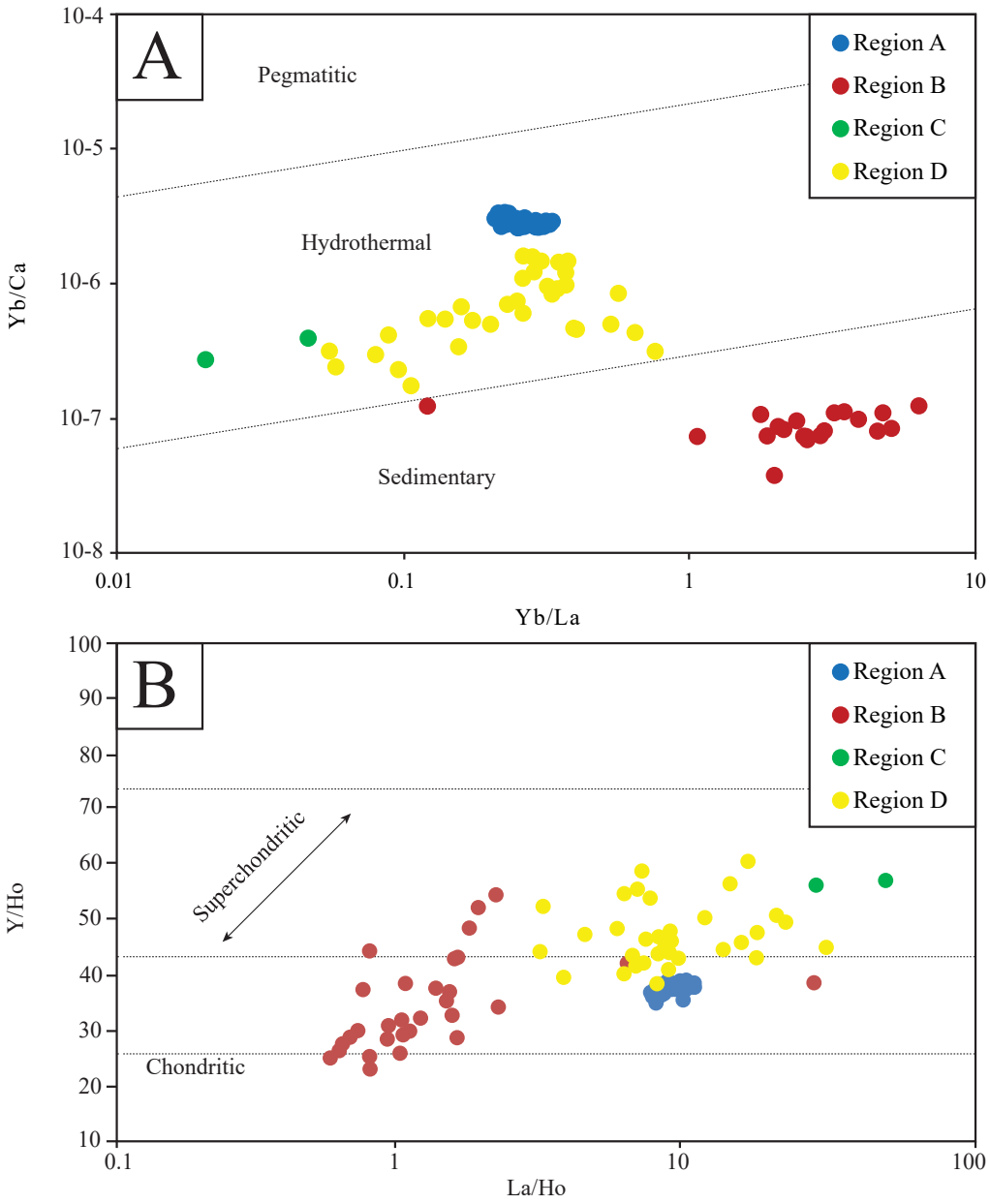

Figure 25: *(A)* Yb/Ca vs. Yb/La variation diagram of calcite regions from Ecton *Sample 1*. From *Liu et al., 2020*. *(B)* Y/Ho vs. La/Ho diagram of calcite regions from Ecton sample. From *Liu et al., 2020* and *Wang et al., 2020*. Superchondritic and chondritic values from *Bau and Dulski, 1999*.

Trace elements through calcite regions

Along with REE, common elements that are incorporated into the crystal structure of calcite are Fe, Mg, Mn, and Sr (**Table 3**) (*Reeder and Paquette, 1989*). These trace elements in

the calcite samples from Ecton conform similarly to the REEY concentrations and display the same regional variations, but there are some notable differences between them.

Sr has consistent concentrations through the pre-mineralisation region of calcite (avg. 94 ppm) but has a distinct decrease in concentration through the syn-mineralisation region (avg. 64 ppm) (**Fig. 18**). Studies have shown that Sr has higher partition coefficients in calcite when growth rates are high (Barker and Cox, 2010) and this change in concentration could be due to varying growth rates of the calcite crystals. Mn has lower partition coefficients at high growth rates, so the expected correlation would be to have higher Mn in the Region B. This pattern is not displayed through the first two regions of the calcite (**Fig. 18**) and so it is unlikely that the Sr concentration variation is due to growth rates of the calcite. Another explanation could be the presence of barite, which EPMA data shows having very high concentrations of Sr (avg. 5.95 wt.%). This would imply that the barite in Ecton is coeval with the chalcopyrite mineralisation; this interpretation can be corroborated by the fact that barite is most commonly found in close proximity to chalcopyrite grains.

The trace elements plotted in **Figure 18** show that through Region A and Region B there is very little variation in concentration (other than Sr, explained above), but the post-mineralisation calcite displays widely variable concentrations of these trace elements (**Fig. 18**). The trend displayed by Fe would support a fluid mixing model, where Fe in the pre-mineralisation fluid was incorporated into calcite, and following the mixing of the hydrothermal fluid carrying the metals that caused sulfide precipitation, the concentration slightly increased in calcite (avg. 477 ppm to avg. 608 ppm). The increase in Fe concentration in the post-mineralisation Region C (1066 ppm) occurs because of the abrupt end to the precipitation of sulfides, possibly due to pressure/temperature changes or the exhaustion of Cu/S in the fluid. Without the precipitation of sulfides, any Fe left in the fluid would be incorporated by calcite and would lead to the exhaustion of Fe in the remaining fluid (as seen in **Fig. 18**).

The variations in concentration of Sr, Mg, and Mn in the post-mineralisation Region C and D calcite are more difficult to explain, but the seemingly oscillatory nature of the concentrations (specifically Sr and Mg; **Fig. 18A**) may not reflect any external influence (Barker and Cox, 2010). A growth-entrapment model (Watson, 2004) could be invoked, explaining cyclical variations in trace element concentrations. This occurs at the crystal face by competition of crystal growth and ‘near-surface’ ion migration of a growing calcite crystal.

Variations in REE and trace element patterns between samples

The REEY patterns (**Fig. 26**) displayed by the calcite in *Sample 2* do not show the same pre-, syn-, and post-mineralisation regions as *Sample 1*. All three regions shown through the *Sample 2* calcite are HREE element enriched compared to LREE and could be interpreted as all being syn-mineralisation. This aligns with the petrographic observations of this sample, where

there is disseminated chalcopyrite throughout all the calcite. The chalcopyrite is also much more diffusely distributed throughout the calcite crystal, which might help explain the lack of a post-mineralisation trend shown by the REE patterns. The pattern of the calcite closest to the crystal edge (**Fig. 26C**) shows slightly more elevated LREE than the inner two regions and could indicate increased mixing input from the pre-mineralisation fluid (likely seawater derived) that is shown by the pre- and post-mineralisation patterns from *Sample 1*. Overall, the comparisons of these two samples support a fluid mixing model of a metal-bearing mineralising fluid and a seawater-derived fluid. The differences in these samples also support a change in mineralisation timing, or spatial differences of the metal distribution within the deposit which could support zonation within the Ecton orebody.

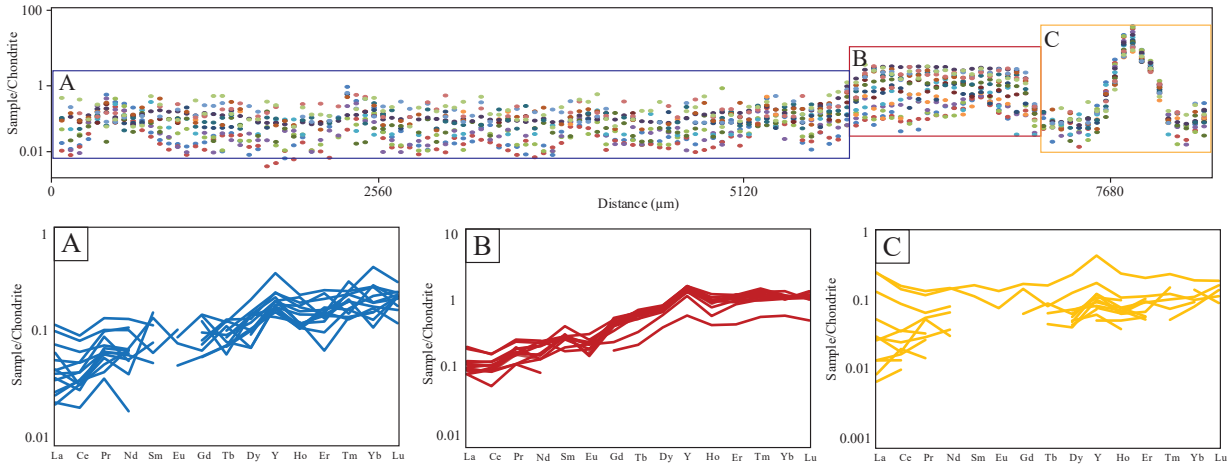

Figure 26: Chondrite normalized REEY trace element patterns for spot analyses along continuous line analysis in *Sample 2* calcite. Chondrite values from *Sun and McDonough, 1989.* Total REEY traverses (from **Fig. 17**) used as reference for Region A-C boundaries.

Sulfur isotopes

The most common source of sulfur in MVT deposits is from the reduction of seawater sulfate that is trapped in local host rocks, with very little input from external regional sources (*Liu et al., 2025*). H_2S is widely generated in geological environments from the reduction of sulfate through two main mechanisms: bacterial sulfate reduction (BSR) or thermochemical sulfate reduction (TSR). Both of these mechanisms have been shown to operate in diagenetic low and high-temperature environments (*Machel, 2001*). BSR occurs in shallow environments with temperature ranges from 0 - 80°. Above these temperatures, sulfate-reducing microbes are rare. TSR occurs over the temperature range of 100° - 180° and at greater depths, with hydrocarbons being the primary reductant (*Machel, 2001*). Global MVT deposits show a wide range in $\delta^{34}S$ values (**Fig. 27A**), with lighter values commonly attributed to BSR (*Leach et al., 2005; Leach et al., 2010*). Deposits with light values require steep thermal gradients to allow for the low-temperature BSR process to occur near the site of mineralisation (*Leach et al., 2005*).

Conversely, TSR results in heavier $\delta^{34}S$ values that fall within -15‰ of the isotope value for the seawater that the sulfur was derived from during formation of the deposit (*Leach et al., 2005; Wilkinson 2014*). The wide range of $\delta^{34}S$ commonly observed in MVT deposits is consistent with the operation of both of these mechanisms, although *Wilkinson (2014)* notes that removing deposits whose associations with the typical genetic model of MVT deposits are debated (*e.g.* Irish-Type and Alpine-Type), means that occurrences of MVT deposits with $\delta^{34}S$ values below 0 are very uncommon (**Fig. 27A**).

Multiple sulfur isotope studies have been carried out across the South Pennine Orefield (Coomer and Ford, 1975; Robinson and Ineson, 1979; Christoula, 1993) and their results, summarised in **Figure 27B**, show a broad $\delta^{34}S$ range consistent with BSR. The presence of hydrocarbons is well documented both in the wider orefield (Ford and Worley, 2016) and at Ecton (Ford, 2000), which would have provided the organic material capable of driving either BSR or TSR. Heavy sulfate $\delta^{34}S$ values from barite at Ecton (+21.1‰ - +24.9‰) align with an origin from Carboniferous seawater, and although these values exceed the typical Carboniferous range (15‰ - 20‰; Claypool *et al.*, 1980), Christoula (1993) suggested that clay-mediated fractionation could preferentially trap isotopically light sulfur, resulting in the heavier $\delta^{34}S$ values from barite seen at Ecton (as reported by Ohmoto and Rye, 1979). Strong evidence for BSR at Ecton comes from the very light $\delta^{34}S$ values reported by Christoula (1993) for sulfides (−17‰ to −7.1‰), characteristic of open-system BSR (Wilkinson, 2014). Additional support is provided by vitrinite reflectance values of hydrocarbons in the South Pennine Orefield (0.53 - 0.57%; Green, 2005), which fall within the upper range for BSR and are far too low to permit TSR (Machel, 2001). Although Christoula (1993) argued that mineralisation temperatures at Ecton were too high for bacterial activity, deposits with steep thermal gradients (such as the Upper Silesia deposit) demonstrate that BSR can still operate under such conditions (Leach *et al.*, 2005). Christoula (1993) also documented substantial $\delta^{34}S$ variability among chalcopyrite samples, ranging from −15.1‰ to −7.1‰.

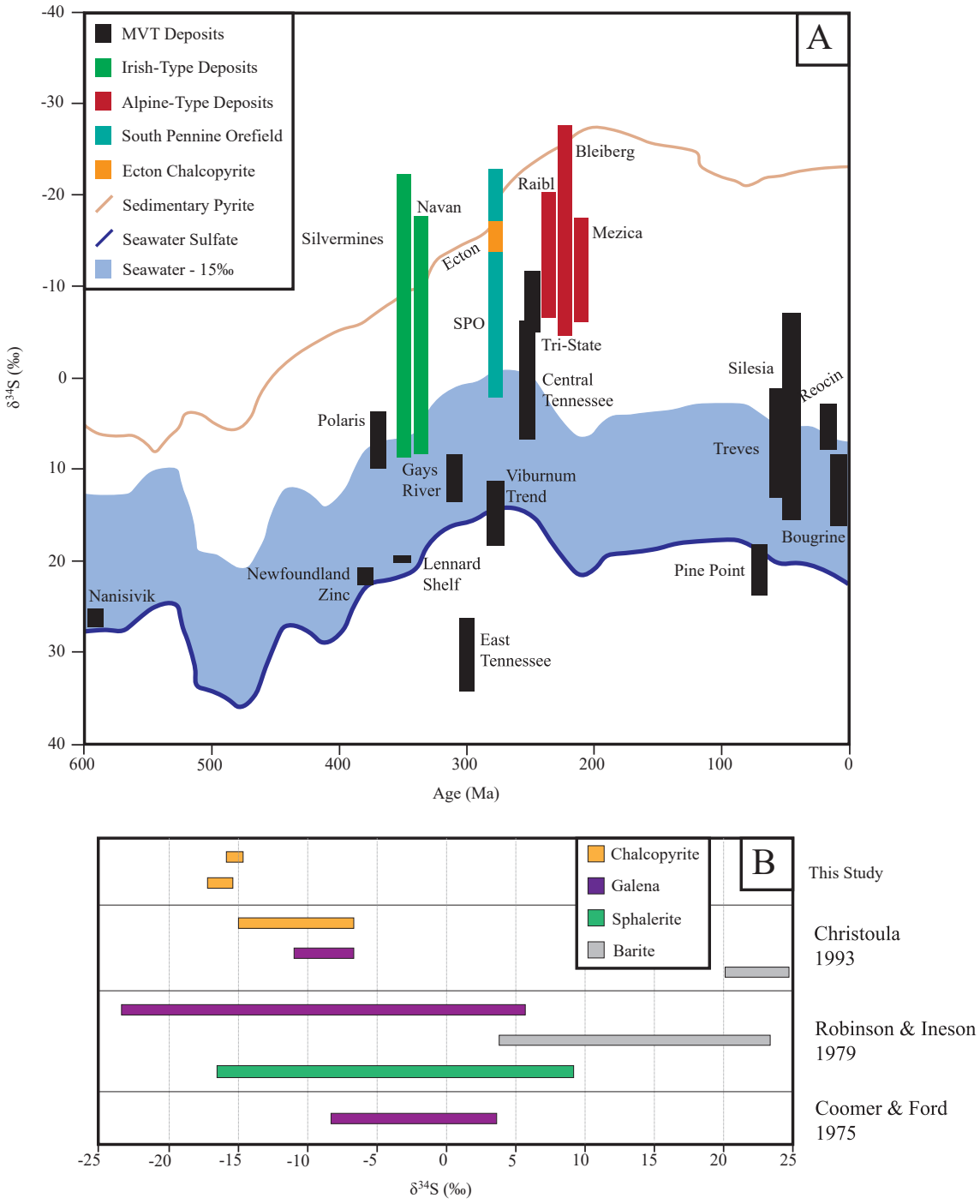

Figure 27: *(A)* Diagram of $\delta^{34}S$ of sulfides vs. age of mineralisation of select MVT deposits. From *Wilkinson, 2014*. Blue background denotes $\delta^{34}S$ values typically derived from TSR. Range of $\delta^{34}S$ values for the South Pennine Orefield (SPO) from authors in *B.* Age of Ecton mineralisation (280 Ma) from *Ford and Worley, 2016*. $\delta^{34}S$ values for Ecton chalcopyrite from this study. *(B)* Summary diagram of historical and present $\delta^{34}S$ isotopic studies from the South Pennine Orefield (*Robinson and Ineson, 1979; Coomer and Ford, 1975*) and Ecton (This study and *Christoula, 1993*).

The sulfur isotope values obtained in the present study fall well within the established $\delta^{34}S$ range for sulfides in the South Pennine Orefield and agree with the lightest values recorded at Ecton (**Fig. 27B**). This indicates that Ecton mineralisation likely formed through similar processes of seawater sulfate reduction. The new data presented here reinforce BSR as the dominant mechanism of sulfate reduction, consistent with the very light $\delta^{34}S$ values characteristic of open-system conditions (Wilkinson, 2014). Relatively limited heterogeneity is observed between the chalcopyrite samples analysed here: *Sample 1* has an average $\delta^{34}S$ value of −15.3‰ (± 0.3‰), while *Sample 2* averages −16.7‰ (± 0.3‰). Although the differences are small compared to the large range of $\delta^{34}S$ values across the South Pennine Orefield, when combined with values from Christoula (1993) they indicate disequilibrium in the mineralisation process at Ecton. Two processes may explain the $\delta^{34}S$ variability observed across both studies: [1] Spatial zonation within the deposit may have influenced isotopic signatures, with deeper samples (closer to hydrothermal fluid sources) recording lighter $\delta^{34}S$ values, and more distal mineralisation resulting in heavier $\delta^{34}S$ values. This interpretation is supported by the sample taken from the Salt's Level (adit level) (−11.4‰) from Christoula (1993), which is isotopically heavier than the samples analysed in this study and originates from the upper part of the deposit; [2] Differences in mineralisation processes identified by variations in ore texture may also play a role. Christoula (1993) identified three distinct chalcopyrite textures: massive chalcopyrite (−7.1‰), veinlet-hosted chalcopyrite (−11.4‰), and chalcopyrite inclusions in calcite (−15.1‰ to −14.8‰). The samples analysed in the current study correspond most closely to the chalcopyrite inclusions in calcite texture, both in isotopic composition and in mineralogical description, although it is unclear if a similar Fe-Ni-As mineral assemblage was observed in the samples used by Christoula (1993). Together, these findings strengthen the interpretation that the chalcopyrite at Ecton formed through BSR and that the observed isotopic variability reflects a combination of spatial controls and formation processes resulting in textural differences within the deposit, albeit the limited number of samples both in this study and Christoula (1993) makes it difficult to substantiate either of these hypotheses further.

Varying $\delta^{34}S$ values corresponding to different ore textures can also be found in the Navan Pb-Zn deposit (Anderson *et al.*, 1998) where large ranges in $\delta^{34}S$ values are clearly defined by specific textures of the sulfides throughout the deposit (e.g. coarsely bladed vs. rhythmic bands vs. dendritic). The $\delta^{34}S$ ranges at Navan are much larger than found at Ecton, and two different sulfur sources from two fluids have been invoked to explain the variation of the former. Despite there being no conclusive evidence for Ecton requiring two separate sulfur sources, a mechanism similar to Navan could be inferred where $\delta^{34}S$ values are controlled by differences in mineralisation processes and timing, but separate sulfur sources from the mixing of fluids cannot be ruled out.

6.3 Linking Localized Evidence to Large-Scale Processes

Emplacement of brecciated pipes

The vertical brecciated pipe mineralisation at Ecton makes the deposit unique within the South Pennine Orefield, and the processes that led to this mode of occurrence have been one of the primary questions surrounding Ecton. However, the lack of access to *in situ* mineralisation present in deeper parts of the Ecton mine precludes both the field observations and comprehensive sampling required to constrain pipe emplacement history. The historical descriptions of the ore body identify them as breccias that crosscut the folded limestones of the Ecton and Milldale Formations and the roughly N-S alignment of pipes along the axial plane of the Ecton Anticline suggests a structural control (Banks, 1776).

Two mechanisms for the formation of the Ecton breccia pipes appear possible: solution collapse and hydraulic fracturing.

Solution collapse: Ford (2000) suggested solution-collapse caused the formation of the vertical pipes. Solution-collapse breccias form by the collapse of caves within limestone units. The resulting porous breccia becomes a conduit for base-metal-bearing hydrothermal fluids. Sulfides precipitate as metals react with sulfur reduced from seawater sulfate. This origin is possible for the Ecton pipe breccias as paleokarsts are widespread throughout the South Pennine Orefield and are hosts to much of the Pb-Zn mineralisation on the eastern side of the orefield, although typically the karst-filling deposits to the east are stratiform or stratabound with the limestone units whereas Ecton would represent a karst-filling deposit that demonstrably crosscuts sedimentary units (Ford and Worley, 2016). Deformation and fracturing in the steeply dipping eastern limb of the Ecton Anticline (as described by Ford (2000)) may have resulted in increased porosity and fluid flow, thus facilitating the formation of karst features in alignment with the axial plane.

Hydraulic fracturing: The trace element data resulting from this study are consistent with pipe formation by hydraulic fracturing from high-pressure hydrothermal fluids. Breccia pipes commonly form from this mechanism in porphyry copper deposits, where overpressured fluids derived from hydrothermal process associated with the underlying magma chamber cause vertical brecciation in the overlying rock (*e.g.* Mammoth breccia pipe, Anderson *et al.*, 2009). There is no known magma chamber below Ecton, but high-pressure fluids can occur in a variety of geological settings, including MVT deposits, where compression from orogenic events can cause the migration of deep basinal fluids within the foreland basin (Leach *et al.*, 2010).

Furthermore, the volatilization of compounds in solution containing Ge (e.g. $GeCl_4$) during fracturing may concentrate Ge (along with other volatiles like As), in the low-pressure fractures. Ge (and As enrichment in chalcopyrite occurs in the studied Ecton samples. Similar Ge and As enrichment are observed in in the Kupferschiefer deposit, where vertical veinlets of

chalcopyrite, formed by high pressure fluids, contained considerably higher concentrations of Ge and As compared to the lower pressure horizontal veinlets (Foltyn *et al.* 2025). Foltyn *et al.* (2025) also suggested that there is a link between Ge enrichment in ore deposits and their host rocks being high-pressure breccias or faults, due to the frequency with which they occur together (e.g. Tsumeb and Kipushi), and this relationship is also observed at Ecton, as demonstrated in the new sulfide trace element data presented here.

Though both methods of breccia pipe emplacement were possibly in operation at Ecton, limited sample material and lack of in situ data preclude any definitive determination. It is important to note that, even if access to deeper regions of the mine were possible, mining activity likely completely removed all breccia material.

Genetic relationship of the copper and lead-zinc mineralisation

The occurrence of Cu at the Ecton mine is unique in the SPO. Many details with respect to the emplacement timeline and relationship to proximal instances of Pb-Zn mineralisation remain poorly understood. Significant copper enrichments in global MVT deposits are rare, though the Bushy Creek Mine, Viburnum Trend (Evans, 1977; Cavender *et al.*, 2016; Shelton *et al.*, 2020) is a notable exception. This deposit was formed by multiple early Cu-Zn-Ni-Co fluids that precipitated sulfides in stratigraphically lower units, before the main Pb-Zn mineralisation typical of the Viburnum trend occurred. Fluid inclusion studies show that the fluids that formed the early sulfides were geochemically distinct from the later generation of fluids that formed the Pb-Zn mineralisation, and distinct $\delta^{34}S$ values identify separate H_2S reservoirs for sulfide precipitation (Shelton *et al.*, 2020). These geochemical and isotopic differences are not observed at Ecton, where $\delta^{34}S$ values of galena and chalcopyrite at Ecton are very similar (**Fig. 27B**), and Christoula (1993) found that the fluid inclusions from Ecton are almost indistinguishable in terms of homogenization temperature and salinity from the rest of the South Pennine Orefield, once again suggesting a common fluid source. Christoula (1993) hypothesised that the copper-bearing hydrothermal fluid forming the Ecton deposit could be the same as the fluid that formed the Pb-Zn mineralisation.

The current study also the occurrence of Cu, Ni, Co, and As in marcasite, indicating these elements were present in the fluid at the time of precipitation, and the depletion of Bi in chalcopyrite suggests that the Cu-Fe-Ni-As minerals were coeval with each other (**Fig. 28**).

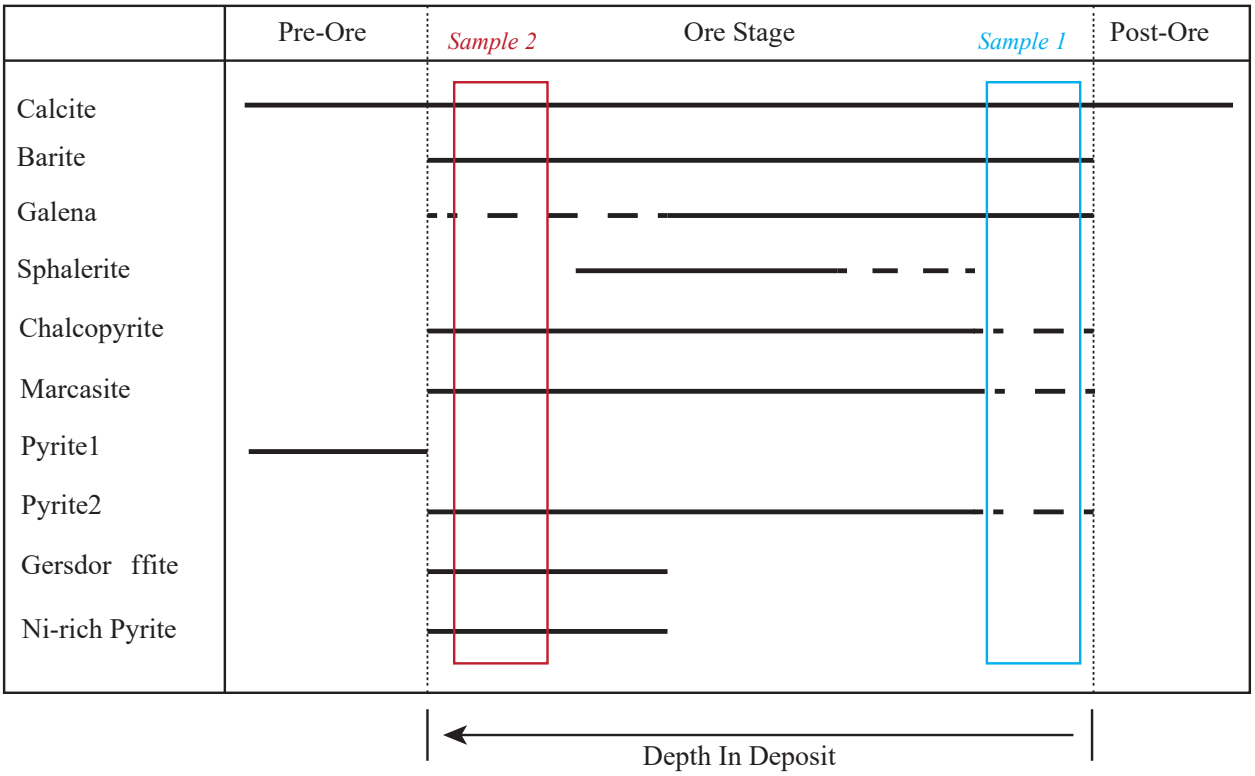

Figure 28: Paragenesis diagram for the Ecton Copper Deposit. Based on observations made in this study and genetic relationships of mineralisation of the South Pennine Orefield from *Ford and Worley 2016; Ford, 2000.* Sample 1 and Sample 2 from this study, with observed mineral assemblages.

The physically isolated occurrence of Ecton could represent a regional zonation of Cu-Ni-As minerals within the South Pennine Orefield. The Irish-Type Lisheen deposit has cogenetic Pb-Zn and Cu-Ni-As mineralisation (Frenzel *et al.*, 2025), and the Cu-Ni-As mineralisation is strongly zoned horizontally. This zonation has been interpreted as a function of proximity to the feeder faults for the hydrothermal fluid entering the hanging wall and a marked decrease outwards in concentrations of these metals is observed (Torremans, 2018). A similar relationship between Pb-Zn and Cu-Ni-As mineralisation in the South Pennine Orefield could explain the isolated occurrence of copper, where Ecton represents the only exposed feeder zone for the cogenetic mineralisation. Using this model, smaller-scale vertical zonation at Ecton would also explain the occurrence of Ni-As minerals at greater depths, whereas Pb-Zn are enriched above. The paragenetic interpretation shown in **Figure 28** shows how the fluid possibly precipitated Ni-As minerals at greater depths (*i.e.* paragenetically first) before the eventual depletion of these metals in the mineralising fluid. The Pb-Zn mineralisation occurs at higher stratigraphic levels.

Source of copper

A definitive explanation for the source of copper at Ecton remains elusive. Three viable hypotheses exist in the literature.

[1] Masheder and Rankin (1988) suggest a fluid unrelated to the South Pennine Orefield Pb-Zn mineralisation that was derived from the Cheshire Basin, located 25 km west of Ecton, which hosts red-bed copper deposits (*e.g*. Alderley Edge) (Naylor *et al.*, 1989). However, the host rocks and copper deposits of the Cheshire Basin are of Triassic age (Warrington, 2012), much younger than the Carboniferous host rocks of Ecton and mineralisation of the South Pennine Orefield. The proposed relationship between Ecton and the Cheshire Basin were discounted by Christoula (1993) based on Cl-Br data from fluid inclusions at Ecton being inconsistent with the fluid compositions in the Cheshire Basin. The Cheshire Basin mineralisation is thought to have derived sulfur from Triassic evaporites through TSR, which is inconsistent with the BSR of Carboniferous seawater at Ecton, proposed in this study.

[2] The copper could have been sourced from the magmatic units that are present within the South Pennine Orefield. Multiple diabase sills (Calton Hill, Tideswell Dale Sill, Waterswallows Sill, Pot-Luck Sill) and basalt flows (Bonsall Basalt, Shacklow Wood Lava, Lower Miller's Dale Lava, Haddonfield Lower Lava) have been dated between 328.6 ± 4.2 Ma and 316.4 ± 3.7 Ma. The magmatism is associated with deep-seated normal faults which facilitated ascension to the surface during the regional maximum extension (Sheldrick *et al.*, 2025). The timing of mineralisation of the South Pennine Orefield is not well understood due to the difficulty of dating sulfide minerals, but dating of clay minerals has been used to determine the approximate age. The clay minerals formed by hydrothermal fluids altering the basalt units and yielded a maximum age of Early Permian (280 Ma), but Ford and Worley (2016) suggest an approximate age of late Namurian to early Westphalian (broadly 320 Ma – 312 Ma). Both methods of dating suggest mineralisation ages that post-date the emplacement of mafic bodies in the orefield, allowing for hydrothermal fluids to source copper from them. Compatible element plots of the diabase and basalt units show depletions of copper concentration which has been attributed to metal-remobilization, attributed to interaction with hydrothermal fluids (Figure 7 *in* Sheldrick *et al.*, 2025).

[3] Christoula (1993) suggested that the Ecton copper was sourced from the Redhouse Sandstone Formation, evidenced by the occurrence of chalcopyrite in that unit and its proximity to Ecton. The Redhouse Sandstone Formation lies on top of the pre-Carboniferous basement (Aitkenhead *et al.*, 2002) and is described as a reddish-brown, pebbly sandstone interbedded with mudstone, siltstone and conglomerates. The occurrence of this unit is only known through the Caldon Low Borehole, 10 km south of Ecton (**Fig. 1**), which intercepts it at a depth of ~365 m, until the termination of the borehole at 535 m (British Geological Survey – Borehole SK04NE36, 1977). Chalcopyrite occurs in the Redhouse Sandstone Formation as disseminated grains in the matrix of the sandstone, as well as hosted in carbonate veins and fractures. Notably, small amounts of azurite and hematite also occur. The Redhouse Sandstone Formation is comparable to the Old Red Sandstone Formation (Kendall, 2017) found across Britain and

Ireland (and likely of the same facies), based both on their age and lithology (Cornwell *et al.*, 1995). The Old Red Sandstone is an important unit in the Irish-Type deposits of the Midlands Basin, Ireland, not acting as a source of copper in these deposits, but as a sink where fluids migrating through the sandstone precipitate Cu, Co, and Ag due to the unit being a redox boundary (Wilkinson, 2023). If the same connection is made between the Redhouse Sandstone Formation and the Ecton copper deposit, it would mean that the sandstone unit is not a source of copper, but rather a trap where much of the copper mineralisation was precipitated before reaching closer to the surface. This also indicates that the copper-rich fluid was present at least 10 km from Ecton and may not be a local occurrence of copper mineralisation. The presence of large amounts of copper mineralisation in the limestone units at Ecton could simply be associated with the thinning of the Redhouse Sandstone Formation (or the lack of its presence) beneath these limestones to the north. It could also be due to the fault-system at Ecton acting as a hydrothermal conduit, allowing the Cu-rich fluid to travel vertically through the Redhouse Sandstone Formation. Either of these scenarios would allow more copper to remain in the migrating fluids passing through the sandstone. This relationship also occurs in the Irish orefield, where thinning of the Old Red Sandstone Formation, and significant faults and fracture systems, marks notably less interaction with the mineralising fluids (Wilkinson, 2023). This could also have implications for the larger South Pennine Orefield, where copper could have been present in the mineralising fluid in much larger quantities but was precipitated at depth due to interaction with either the Redhouse Sandstone Formation or a similar boundary, although this sandstone unit has never been proven at depth on the eastern side of the orefield. This would result in the formation of Pb-Zn rich deposits at higher stratigraphic levels (Frenzel *et al.*, 2025), as seen in the numerous deposits in the South Pennine Orefield, and the Cu-rich mineralisation being disseminated across a large volume of rock at greater depths.

Ecton genetic model and comparisons

The findings of this study are consistent with the copper mineralisation at Ecton being related to, and cogenetic with, the MVT Pb-Zn mineralisation of the South Pennine Orefield, making it an example of locally-copper enriched MVT mineralisation. Ecton also displays distinct similarities to Irish-Type deposits where the concentrations of Cu-Ni-As are typically higher, and in some cases present in economic quantities. The characteristics of the Ecton deposit are compared to both Irish-Type and MVT deposits in **Table 3**.

Irish-Type deposits are defined by multiple characteristics that distinguish them from typical MVT deposits. These include: (1) the primary mineralogy is sphalerite and galena, often with considerable amounts of Fe-sulfides and variable amounts of chalcopyrite and tennantite; (2) they occur along, or adjacent to, normal faults acting as conduits for hydrothermal fluid; (3) they form from the mixing of hot, metal-bearing, sulfur-poor fluids with sulfur-rich fluids

derived from Carboniferous seawater; and (4) they display a complex range of sulfide textures (Hitzman and Beaty, 1996).

The South Pennine Orefield main ore minerals are galena and sphalerite, with varying amounts of marcasite or pyrite. Ecton is the largest occurrence of chalcopyrite within the SPO, but also hosts galena, sphalerite and marcasite. Although Ecton is not associated with known normal faulting, a structural control on mineralisation is evident (**Fig. 3**), both from the Ecton anticline and the reverse fault system underlying this fold. Fluid mixing is evident by the variations in calcite trace element compositions presented in this study, with an initial sulfur-rich fluid originating from the derivation of H_2S through BSR of Carboniferous seawater, resulting in similar $\delta^{34}S$ values as Irish-Type deposits (**Fig. 27B**).

Table 3: Comparison of Characteristics of Ecton, Irish-Type, and MVT Deposits

	Ecton	Irish-Type	MVT
Host rocks	Turbidite limestone (Ecton Limestone Formation)	Non-argillaceous carbonates with minor siliciclastics	Mainly dolostone and limestone
Structural Controls	Orebodies parallel to Ecton anticline. Unknown relationship with underlying fault system	Synsedimentary faults and associated breccias and faults	Normal, wrench, and transtensional faults with associated breccias and fractures
Ore body controls	Hosted in breccias with undetermined origin	Stratabound lenses in preferred sedimentary horizons. Sedimentary and hydrothermal breccias. May be underlain by feeder zone	Commonly stratabound or pipes. Veins, and dissolutions breccias
Ore Mineralogy	Chalcopyrite, Marcasite, Pyrite, Galena, Sphalerite, Ni-Rich Pyrite, Gersdorffite	Sphalerite, Galena, Pyrite, Marcasite, Chalcopyrite	Sphalerite, Galena, Pyrite, Marcasite
Ore Texture	Inclusions in calcite, veinlet-hosted, and massive	Highly variable but predominantly massive	Coarsely crystalline to fine-grained. Massive to disseminated
Fluid Temperature	Low (90°)	Low to moderate (70° - 280°)	Low (90° - 150°)
Sulfur Isotopes	Negative. BSR derived sulfur in second fluid	Negative. BSR derived sulfur in second fluid	Positive. TSR derived sulfur in host rock or second fluid
Mineralisation Timing	Epigenetic	Mostly during diagenesis or syngenetic	Epigenetic

Table based on *Wilkinson, 2014*. Data from *Leach et al., 2005; Christoula, 1993; Ford and Worley, 2016*

Frenzel *et al.*, (2025) suggests copper enrichment in Irish-Type deposits requires fluids to reach in excess of 200 °C to carry the metals in solution. No evidence exists to suggest elevated fluid temperatures within the Ecton system: previous fluid inclusion studies in calcite indicate a maximum homogenization temperature of 90 °C (Christoula, 1993). However, from the fluid mixing model suggested here, it is not clear if this maximum temperature is representative of the metal-bearing fluid that carried the copper, or rather the seawater-derived fluid that resulted in the pre- and post-mineralisation calcite. It is also possible that the existence of Ecton is evidence that the mineralising fluids of Irish-Type deposits do not need to reach such high temperatures, and that mobilisation of significant copper is possible at lower temperatures typical of MVT fluids (*e.g.,* via low temperature mobilisation of Cu by chloride complexes; Zhong *et al.*, 2015). Using the data from fluid inclusions, Christoula (1993) determined that the mineralising fluid for both the Pb-Zn and Cu mineralisation was Na-Ca-Cl rich brines, which would substantiate Cu mobilisation via chloride complexes. The close spatial association with the Redhouse Sandstone is also notable, especially combined with the fault-system at Ecton which would allow for the metal-bearing fluids to bypass this sandstone unit. In the Irish-Type deposits this unit is interpreted as a trap for copper in solution, and similarly requires faults as conduits for hydrothermal fluids to precipitate copper above the Old Red Sandstone (Wilkinson, 2023; Doran *et al.*, 2025).

Based on the data presented, Ecton represents a feeder zone from which hydrothermal fluids ascended through the limestone sequences, and similar to the Lisheen Deposit (Torremans *et al.*, 2018; Frenzel *et al.*, 2025), precipitated copper-dominant ore proximal to the fault system underlying Ecton Hill (**Fig. 4B, Fig. 29**). The breccia-hosted nature of the copper ore at Ecton could represent a unique scenario where these fluids were able to reach higher stratigraphic levels due to either the presence of a sedimentary solution-collapse breccia located above the fault system, or hydrothermal brecciation of the highly deformed and folded limestone sequences at Ecton at the time of mineralisation. Given the strong structural control on mineralisation throughout the South Pennine Orefield, where ore fluids re-opened pre-existing faults by hydraulic fracturing (Mostaghel, 1985), it is possible that there are similar feeder zones with copper mineralisation throughout the orefield and would likely be present at greater depths than worked in the Pb-Zn mines. The basement structure of the South Pennine Orefield could also have a strong control on the vertical location of this copper mineralisation because the orefield is divided onto multiple tilt blocks, with the Bakewell Fault Zone dividing a much thicker sedimentary package to the east, from the thinner sequence to the west (**Fig. 29**) (Aitkenhead *et al.*, 2002; Sheldrick *et al.*, 2025). Larger amounts of erosion on the eastern side of the orefield, as well as the thinner limestone sequence could explain why the copper mineralisation at Ecton is close to the surface. A similar comparison could be to the Gortdrum Cu-Ag deposit in Ireland, which represents a near-surface feeder zone of the Irish-Type deposits where the overlying Pb-Zn mineralisation was eroded away (Dunlevy *et al.*, 2023)

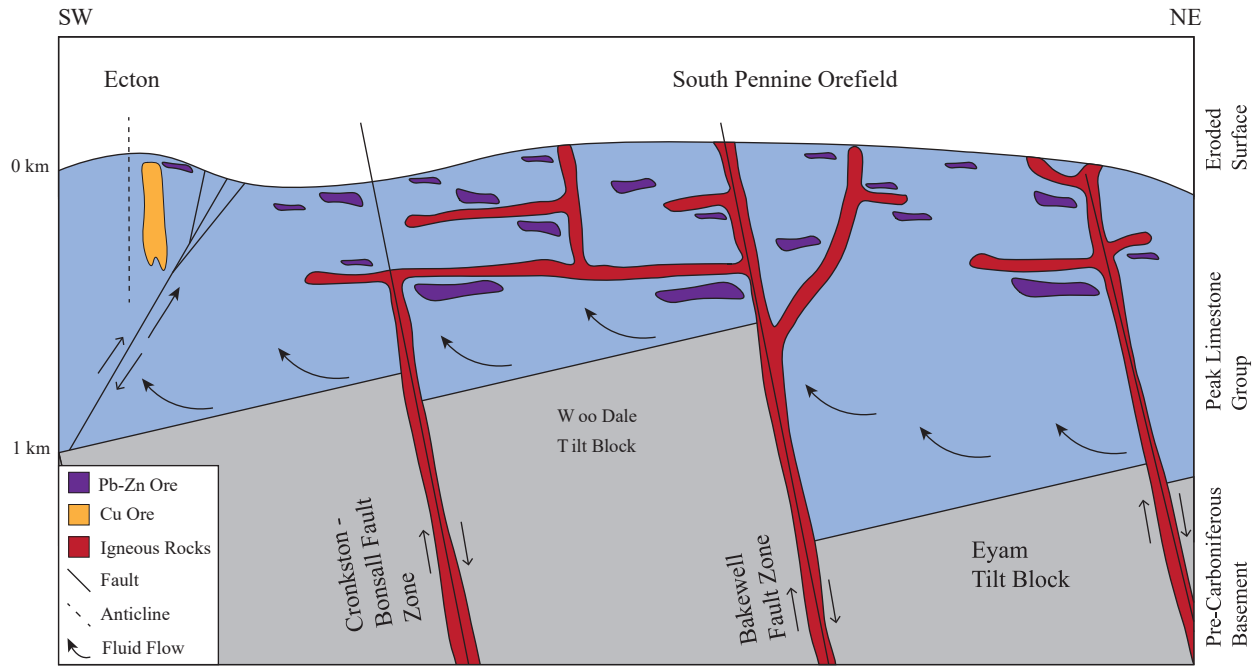

Figure 29: Schematic cross-section of the South Pennine Orefield, showing known mineralisation and relationships with magmatic units and basement structure. Based on *Corfield, 1996; Ford and Worley, 2016; Sheldrick et al., 2025*.

7. Conclusion

Mississippi Valley-Type deposits are a major global source of Pb and Zn, although some localities contain significant quantities of Cu mineralisation. The uncommon occurrence of this Cu enrichment in the low-temperature, carbonate-hosted deposits has been explained in multiple ways, including multiple fluid events, remobilization, or that it can occur alongside the main Pb-Zn mineralisation under the right conditions.

Through the use of mineralogical, geochemical, and isotopic evidence, this study has determined:

[1]: Based on calcite trace element, a fluid mixing model is proposed for the formation of the Ecton Copper Deposit. Variations in REE + Y concentrations, along Y/Ho ratios, across calcite growth regions indicate a fluid mixing event, likely between a Carboniferous seawater-derived fluid and a metal-bearing hydrothermal fluid.

[2]: Isotopic data presented here show that Ecton derived the sulfur required for sulfide precipitation through bacterial sulfide reduction of Carboniferous seawater. The $\delta^{34}S$ values from Ecton fall within the range of values previously determined throughout the South Pennine

Orefield, and that this range is more comparable to Irish-type deposits than to typical MVT deposits globally.

[3]: The geochemical data show that the Ecton Copper Deposit is a hydrothermal, carbonate-hosted Cu deposit that diverges from some of the typical characteristics of MVT deposits (*e.g.* high Cu content, association of Ni-Co-As mineral assemblages, derivation of sulfur through BSR) but also demonstrates consistency in the processes that were occurring with the Pb-Zn mineralisation across the South Pennine Orefield (*e.g.* $\delta^{34}S$ values).

[4]: Sample heterogeneity between *Sample 1* and *Sample 2* (mineralogical, textural, geochemical, and isotopic) could reflect spatial controls within the deposit and proximity to the hydrothermal feeder zone. Metal zonation is displayed throughout the South Pennine Orefield, although the lack of *in situ* material from Ecton prohibits further investigation of the true extent of localised deposit-scale zonation.

[5]: Although Ecton shows some characteristics of typical MVT deposits, the abundant copper mineralisation, strong structural control by faults and fold axes, BSR derived sulfur, and the proximity to the Redhouse Sandstone Formation suggests that Ecton may be closely related to Irish-type deposits. This challenges the classification of Ecton, and perhaps the South Pennine Orefield, as an MVT deposit, although further investigation would be required throughout the orefield to determine if other Ecton-type deposits occur at greater depths beneath the Pb-Zn mineralisation.

8. References

Aitkenhead, N. (1971). The National Grid Geological Map, SHEET SK 05 NE. *British Geological Survey.*

Aitkenhead, N., Barclay, W.J., Brandon, A., Chadwick, R.A., Chisholm, J.I., Cooper, A.H., and Johnson, E.W. (2002) British regional geology: the Pennines and adjacent areas (Fourth edition). *British Geological Survey.*

Anderson, E., Atkinson, W.W., Marsh, T., and Iriondo, A. (2009). Geology and geochemistry of the Mammoth breccia pipe, Copper Creek mining district, southeastern Arizona: Evidence for a magmatic-hydrothermal origin. *Mineralium Deposita*, **44**(2), 151-170.

Anderson, I.K., Ashton, J.H., Boyce, A.J., Fallick, A.E., and Russell, M.J. (1998). Ore depositional processes in the Navan Zn-Pb deposit, Ireland. *Economic Geology*, **93**(5), 535-563.

Banks, J. (1767). MS journal, Cambridge University Library, Add. Mss 6294. Reprinted in *Journal Staffordshire Industrial Archaeology Society*, **2**, 1-20 (1971).

Barker, S.L.L., and Cox, S.F. (2010). Oscillatory zoning and trace element incorporation in hydrothermal minerals: insights from calcite growth experiments. *Geofluids*, **11**, 48-56.

Bau, M. (1991). Rare-earth element mobility during hydrothermal and metamorphic fluid-rock interaction and the significance of the oxidation state of europium. *Chemical Geology,* **93**, 219-230.

Bau, M. (1996). Controls on the fractionation of isovalent trace elements in magmatic and aqueous systems: evidence from Y/Ho, Zr/Hf, and lanthanide tetrad effect. *Contributions to Mineralogy and Petrology*, **123**, 323-333.

Bau, M., and Dulski, P. (1995). Comparative study of yttrium and rare-earth element behaviours in fluorine-rich hydrothermal fluids. *Contributions to Mineralogy and Petrology*, **119**, 213-223.

Bau, M., and Dulski, P. (1999). Comparing yttrium and rare earths in hydrothermal fluids from the Mid-Atlantic Ridge: implications for Y and REE behaviour during near-vent mixing and for the Y/Ho ratio of Proterozoic seawater. *Chemical Geology*, **155**(1-2), 77-90.

Belissont, R., Munoz, M., Boiron, M., Luais, B., and Mathon, O. (2019) Germanium Crystal Chemistry in Cu-Bearing Sulfides from Micro-XRF Mapping and Micro-XANES Spectroscopy. *Minerals,* **9**, 227.

Bjørlykke, A., and Sangster, D.F. (1981) An overview and sandstone lead deposits and their relationship to red-bed copper and carbonate-hosted lead-zinc deposits. *In* B.J. Skinner

(Eds.), *Economic Geology Seventy-fifth Anniversary Volume* (p. 179-213). Economic Geology Publishing Company.

Breislin, C.J., Banks, V.J., Crowley, S.F., Marshall, J.D., Millar, I., Riding, J.B., and Hollis, C.E. (2020). Mechanisms controlling the localisation of fault-controlled hydrothermal dolomitisation, Derbyshire Platform, UK. *Journal of Sedimentary Research*, **90**(9), 1156-1174.

Cave, B., Lilly, R., and Barovich, K. (2020). Textural and geochemical analysis of chalcopyrite, galena and sphalerite across the Mount Isa Cu to Pb-Zn transition: Implications for a zoned Cu-Pb-Zn system. *Ore Geology Reviews*, **124**, 103647.

Cavender, B.D., Shelton, K.L., and Schiffbauer, J.D. (2016). An atypical orebody in the Brushy Creek Mine, Viburnum Trend, MVT District, Missouri: Early Cu-(Ni-Co)-Zn rich ores at the Lamotte sandstones/Bonneterre dolomite contact. *Economic Geology*, **111**(1), 259-269.

Chisholm, J., Mitchell, M., Strank, A., Cox, F., and Harrison, D. (1983). A revision of the stratigraphy of the Asbian and Brigantian limestones west of Matlock. *Institute of Geological Sciences*, **83**, 1724.

Christoula, M. (1993). Fluid Inclusion Geochemistry of Selected Epigenetic, Low Temperature Mineralization in the U.K. *Imperial College London*.

Claypool, G.E., Holser, W.T., Kaplan, I.R., and Zak, I. (1980). Age curves of sulfur and oxygen isotopes in marine sulfate and their mutual interpretation. *Chemical Geology*, **28**(3-4), 199-260.

Coomer, P.G., and Ford, T.D. (1975). Lead and Sulphur Isotope Ratios of Some Galena Specimens from the South Pennines and North Midlands. *Mercian Geology*, **5**(4), 291-304.

Corfield, S.M.00, Gawthorpe, R.L., Gage, M., Fraser, A.J., and Besly, B.M. (1996). Inversion tectonics of the Variscan foreland of the British Isles. *Journal of the Geological Society*, **153**, 17-32.

Cornwell, J.D., Busby, J.P., Colman, T.B., and Norton, G.E. (1995). Exploration for carbonate-hosted base-metal mineralisation near Ashbourne, Derbyshire. *Mineral Reconnaissance Programme Report, British Geological Survey, No. 139*.

Critchley, M. (1979). A geological outline of the Ecton copper mines, Staffordshire. *Bulletin of the Peak District Mines Historical Society*, **7**(4), 177-191.

Dempsey, E.D., Holdsworth, R.E., Selby, D., Bird, A., Young, B., and Le Cornu, C. (2021). A revised age, structural model and origin for the North Pennine Orefield in the Alston

Block, northern England: intrusion (Whin Sill)-related base metal (Cu–Pb–Zn–F) mineralization. *Journal of the Geological Society*, **178**.

Doran, A.L., Hollis, S.P., Menuge, J.F., Lyons, C., Piercey, S.J., Boyce, A.J., Slezak, P., Torremans, K., and Guven, J. (2025). Evidence for metal sources, fluid-mixing processes, and S isotope recycling within the feeder zone of an Irish type Zn-Pb deposit. *Ore Geology Reviews*, **182**, 106660.

Dunham, K.C. (1983). Ore genesis in the English Pennines: a fluoritic subtype. *International Conference on MVT lead-zinc deposits: Missouri, University of Missouri-Rolla*.

Dunlevy, E., Torremans, K., Holdstock, M., and Hitzman, M. (2023). A new look at the Gortdrum copper deposit, Co. Tipperary, Ireland. *In* C.J. Andrew, M.W. Hitzman, and G. Stanley (Eds.) *Irish-type Deposits around the world* (p. 363-370). Irish Association for Economic Geology, Dublin.

Evans, L.L. (1977). Geology of the Brushy Creek Mine, Viburnum Trend, Southeast Missouri. *Economic Geology*, **72**(3), 381-390.

Foltyn, K., Wegrzynek, D., Erlandsson, V.B., Gugala, E., Kozub-Budzyn, G.A., Melcher, F., Szczerbowska-Boruchowska, M., and Piestrzynski, A. (2025). Geochemical and mineralogical investigation of germanium-rich chalcopyrite veins from the Cu-Ag Kupferschiefer deposit, Poland. *Ore Geology Reviews*, **181**, 106636.

Ford, T.D. (2000). Geology of the Ecton and Other North-East Staffordshire Mines. *Mining History: The Bulletin of the Peak District Mines Historical Society*, **14**(4), 1-22.

Ford, T.D. (2004). Ecton Copper Deposits, Staffordshire. *Mercian Geologist*, **16**(1), 62-64.

Ford, T.D., and Quirk, D.G. (1995). Mineralization of the South Pennines. *Geology Today*, **11**, 77-182.

Ford, T.D., and Worley, N.E. (2016). Mineralization of the South Pennine Orefield, UK – A Review. *Proceedings of the Yorkshire Geological Society*, **61**, 55-86.

Frenzel, M**.**, Röhner, M., Cook, N.J., Gilbert, S., Ciobanu, C.L., and Güven, J.F. (2025) Mineralogy, mineral chemistry, and genesis of Cu-Ni-As-rich ores at Lisheen, Ireland. *Miner Deposita,* **60**, 113–143.

George, L.L., Cook, N.J., Crowe, B.B.P., and Ciobanu, C.L. (2018). Trace elements in hydrothermal calcite. *Mineralogical Magazine*, **82**(1), 59-88.

Green, P.F. (2005). Burial and exhumation histories of Carboniferous rocks of the Southern North Sea and onshore UK, with particular emphasis on post-Carboniferous events. *In* Collinson, J.D., Evans, D.J., Holliday, D.W. and Jones, N.S. (Eds.) *Carboniferous*

Hydrocarbon Resources: The Southern North Sea and Surrounding Areas, **7** (p. 25-34). Yorkshire Geological Society Occasional Publication Series.

Hawthorne, F.C., and Gagne, O.C. (2024). New ion radii for oxides and oxysalts, fluorides, chlorides and nitrides. *Acta Cryst.*, **B80**, 326-339.

Hayes, T.S., Cox, D.P., Piatak, N.M., and Seal II, R.R. (2015). Sediment-hosted stratabound copper deposit model. *U.S. Geological Survey Scientific Investigations Report 2010-5070-M.*

Heijlen, W., Muchez, P., Banks, D.A., Schneider, J., Kucha, H., and Keppens, E. (2003). Carbonate-Hosted Zn-Pb Deposits in Upper Silesia, Poland: Origin and Evolution of Mineralizing Fluids and Constraints on Genetic Models. *Economic Geology,* **98**(5), 911-932.

Heyl, A.V., Agnew, A.F., Lyons, E.J., Behre, C.H., and Flint, A. (1959). The Geology of the Upper Mississippi Valley Zinc-Lead District. *U.S. Geological Survey Professional Paper 309*.

Hitzman, M.W., and Beaty D.W. (1996). The Irish Zn-Pb-(Ba) Orefield. *In* D.F. Sangster, G.M. Anderson, G. Garven, R.D. Hagni, K.L Shelton, R.M Coveney Jr., J.M. Gregg, and S.E. Kesler (Eds.), *Carbonate-Hosted Lead-Zinc Deposits: 75th Anniversary Volume*. Special Publications of The Society of Economic Geologists.

Holl, R., Kling, M., and Schroll, E. (2007). Metallogenesis of germanium – A review. *Ore Geology Reviews,* **30**, 145-180.

Intiomale, M.M., and Oosterbosch, R. (1974). Géologie et géochimie du gisement de Kipushi, Zaire. *In* Publications spéciales, Gisements stratiformes et provinces cuprifères - Centenaire de la Société Géologique de Belgique*. Annales de la Société géologique de Belgique.*123-164.

Jiu, B., Jin, Z., Hao, H., Wang, Z., Huang, W., Shang, Z., Liu, R., Li, Y., Huang, L., Qin, B., Huang, Z., Long, L., Zhang, W., and Wang, Y. (2025). Modes of occurrence of rare earth elements and yttrium in the subbituminous coal of the Jungar Coalfield, Ordos Basin, North China. *International Journal of Coal Geology*, **305**, 104785.

Jochum, K.P., Willbold, M., Raczek, I., Stoll, B., and Herwig, K. (2005). Chemical Characterisation of the USGS Reference Glasses GSA-1G, GSC-1G, GSD-1G, GSE-1G, BCR-2G, BHVO-2G and BIR-1G Using EPMA, ID-TIMS, ID-ICP-MS and LA-ICP-MS. *Geostandards and Geoanalytical Research*, **29**(3), 285-302.

Johnson, G.A.L., and Dunham, K.C. (2001). Emplacement of the Great Whin Dolerite Complex and the Little Whin Sill in relation to the structure of northern England. *Proceedings of the Yorkshire Geological Society*, **53**, 177-186.

Kendall, R.S. (2017). The Old Red Sandstone of Britain and Ireland – a review. *Proceedings of the Geologists' Association*, **128**(3), 409-421.

Kirstein, L.A., Davies, G.R., Heeremans, M. (2006). The petrogenesis of Carboniferous-Permin dyke and sill intrusions across northern Europe. *Contributions to Mineralogy and Petrology*, **152**, 721-742.

Kraemer, D., Viehmann, S., Banks, D., Sumoondur, A.D., Koeberl, C., and Bau, M. (2019). Regional variations in fluid formation and metal sources in MVT mineralization in the Pennine Orefield, UK: Implications from rare earth element and yttrium distribution, Sr-Nd isotopes and fluid inclusion compositions of hydrothermal vein fluorites. *Ore Geology Reviews,* **107**, 960-972.

Leach, D.L., Sangster, D.F., Kelley, K.D., Large, R.R., Garven, G., Allen, C.R., Gutzmer, J., and Walters, S. (2005). Sediment-hosted lead-zinc deposits: A global perspective. *In* Economic Geology: One hundredth anniversary volume (p. 561-608). Society of Economic Geologists.

Leach, D.L., Taylor, R.D., Fey, D.L., Diehl, S.F., and Saltus, R.W. (2010). A Deposit Model for Mississippi Valley-Type Lead-Zinc Ores. *In* Mineral Deposit Models for Resource Assessment: U.S. Geological Survey Scientific Investigations Report 2010-5070-A (p. 1-52).

Liu, G., Yuan, F., Deng, Y., Wang, F., White, N.C., Huizenga, J.M., Li, Y., Li, X., and Zhou, T. (2020). Ore-fluid geochemistry of the Hehuashan Pb-Zn deposit in the Tongling ore district, Anhui province, China: Evidence from REE and C-H-O isotopes of calcite. *Ore Geology Reviews*, **117**, 103279.

Liu, Y., Hou, Z., Yue, L., Zhuang, L., and Ma, W. (2025). Local sulfur sources control the development of Mississippi Valley-type Pb-Zn deposits worldwide. *Global and Planetary Change*, **225**, 105105.

Lombaard, A.F., Günzel, A., Innes, J., and Krüger, T.L. (1986). The Tsumeb lead-copper-zinc-silver deposit, Southwest Africa/Namibia. *In* C.R. Anhaeusser and S. Maske (Eds.), *Mineral Deposits of Southern Africa*, **2** (p. 1161-1187). Geological Society of South Africa.

Machel, H.G. (2001). Bacterial and thermochemical sulfate reduction in diagenetic settings – old and new insights. *Sedimentary Geology*, **140**(1-2), 143-175.

Masheder, R., and Rankin, R.H. (1988). Fluid Inclusion Studies on the Ecton Hill Copper Deposits, North Staffordshire. *Mineralogical Magazine*, **52**(367), 473-482.

Mostaghel, M.A. (1985). Classification of the South Pennine Orefield. *Mercian Geologist*, **10**(1), 27-38.

Mostaghel, M.A., and Ford, T.D. (1986). A Sedimentary Basin Evolution Model for Ore Genesis in the South Pennine Orefield. *Mercian Geologist*, **10**(3), 209-224.

Mudd, G.M., Jowitt, S.M., and Werner, T.T. (2017). The world's lead-zinc mineral resources: Scarcity, data, issues and opportunities. *Ore Geology Reviews,* **80**, 1160-1190.

Myint, A.Z., Wagner, T., and Fusswinkel, T. (2022). Calcite trace element geochemistry of Au deposits in the Singu-Tabeikkyin Gold District, Myanmar: Implications for the sources of ore-forming fluids. *Ore Geology Reviews*, **145**, 104892.

Naylor, H., Turner, P., Vaughan, D.J., Boyce, A.J. and Fallick, A.E. (1989). Genetic studies of red bed mineralization in the Triassic of the Cheshire Basin, northwest England. *Journal of the Geological Society of London,* **146**, 685–699.

Niu, P., Wei, H., Zhang, M., and Jiang, S. (2026). Mechanisms of germanium substitution into sphalerite constrained from thermodynamic calculations: Implications for germanium enrichment in Pb–Zn deposits. *Geochimica et Cosmochimica Acta*, **412**, 209-220.

Ohmoto, H., and Rye, R.O. (1979). Isotopes of Sulphur and Carbon. *In* H.L. Barnes (Eds.) *Geochemistry of Hydrothermal Ore Deposits (2nd Edition)* (p. 509-567). Wiley & Sons, New York.

Paton, C., Hellstrom, J., Paul, B., Woodhead, J., and Hergt, J. (2011). Iolite: Freeware for the visualisation and processing of mass spectrometric data. *Journal of Analytical Atomic Spectrometry*, **26**(12), 2508-2518.

Partey, F., Lev, S., Casey, R., Widom, E., Lueth, V.W., and Rakovan, J. (2009) Source of fluorine and petrogenesis of the Rio Grande rift-type barite-fluorite-galena deposits. *Economic Geology,* **104**, 505-520.

Paul, B., Paton, C., Norris, A., Woodhead, J., Hellstrom, J., Hergt, J., and Greig, A. (2012) CellSpace: A module for creating spatially registered laser ablation images within the Iolite freeware environment. *Journal of Analytical Atomic Spectrometry*, **27**(4), 700.

Paul, B., Petrus, J., Savard, D., Woodhead, J., Hergt, J., Greig, A., Paton, C., and Rayner, P. (2023). Time resolved trace element calibration strategies for LA-ICP-MS. *Journal of Analytical Atomic Spectrometry*, **38**(10), 1995-2006.

Qui, W.J., and Zhou, M. (2025). Self-organizational origin of oscillatory zoning in pyrite: A coupled diffusion-reaction model and pH-dependent As adsorption feedback mechanism. *Geochimica et Cosmochimica Acta*, **403**, 94-111.

Quirk, D.G. (1987). Structure and Genesis of the South Pennine Orefield. *University of Leicester*.

Quirk, D.G. (1993). The origin of the Peak District Orefield. *Bulletin of the Peak District Mines Historical Society*, **12**, 1-15.

Reeder, R.J., and Paquette, J. (1989). Sector zoning in natural and synthetic calcites. *Sedimentary Geology*, **65**(3-4), 239-247.

Rhodes, D., Lantos, E.A., Lantos, J.A., Webb, R.J., and Owens, D.C. (1984). Pine Point Orebodies and Their Relationship to the Stratigraphy, Structure, Dolomitization, and Karstification of the Middle Devonian Barrier Complex. *Economic Geology,* **79**, 991-1055.

Robinson, B.W., and Ineson, P.R. (1979). Sulphur, oxygen and carbon isotope investigations of lead-zinc-baryte-fluorite-calcite mineralization, Derbyshire. *Transactions of the Institute of Mining and Metallurgy*, **B88**, 107-117.

Russell, M.J. (1986). Extension and convection: A genetic model for the Irish carboniferous base metal and barite deposits. *In* Andrew, C.J., Crowe, R.W.A., Finlay, S., Pennell, W.M., and Pyne, J.F. (Eds.) *Geology and genesis of mineral deposits in Ireland* (p. 545-554). Irish Association of Economic Geology, Dublin.

Samson, I.M., Williams-Jones, A.E., Ault, K.M., Gagnon, J.E., and Fryer, B.J. (2008). Source of fluids forming distal Zn-Pb-Ag skarns: Evidence from laser ablation-inductively coupled plasma-mass spectrometry analysis of fluid inclusions from El Mochito, Honduras. *Geology,* **36**(12), 947-950.

Sanchez, V., Cardellach, E., Corbella, M., Vindel, E., Martin-Crespo, T., Boyce, A.J. (2010). Variability in fluid sources in the fluorite deposits from Asturias (N Spain): Further evidence from REE, radiogenic (Sr, Sm, Nd) and Stable (S, C, O) isotope data. *Ore Geology Reviews*, **37**(2), 87-100.

Savard, D., Bouchard-Boivin, B., Barnes, S.J., & Garbe-Schönberg, D. (2018). UQAC-FeS: A new series of base metal sulfide quality control reference material for LA-ICP-MS analysis. In *Proceedings of the 10th International Conference on the Analysis of Geological and Environmental Materials, Sydney, Australia* (p. 8-13).

Savard, D., Dare, S., Bédard, L.P., and Barnes, S.J. (2023). A new mapping protocol for laser ablation (with fast-funnel) coupled to a time-of-flight mass spectrometer (LA-FF-ICP-ToF-MS) for the rapid, simultaneous quantification of multiple minerals. *Geostandards and Geoanalytical Research*, **47**(2), 243-265.

Sheldrick, T.C., Hahn, G., Antoshechkina, P.M., Norry, M.J., Egan, S.S., Barry, T.L., Gan, C., Wilkinson, C.M., Gibson, S.A., and Ewan, C.A. (2025). Carboniferous and Early Permian Magmatism in England. *Journal of Petrology*, **66**(8).

Shelton, K.L., Cavender, B.D., Perry, L.E., Schiffbauer, J.D., Appold, M.S., Burstein, I., and Fike, D.A. (2020). Stable isotope and fluid inclusion studies of early Zn-Cu-(Ni-Co)-rich ores, lower ore zone of Brushy Creek mine, Viburnum Trend MVT district, Missouri, U.S.A.: Products of multiple sulfur sources and metal-specific fluids. *Ore Geology Reviews*, **118**, 103358.

Skirrow, R.G. (2022). Iron oxide copper-gold (IOCG) deposits – A review (part 1): Settings, mineralogy, ore geochemistry and classification. *Ore Geology Reviews*, **140**, 104569.

Smith, K., Smith, N.J.P. and Holliday, D. (1985). The deep structure of Derbyshire. *Geological Journal*, **20**, 215–225.

Starkey, R.E. (2018). Minerals of the English Midlands. *British Mineralogy Publications*.

Sun, S.S., and McDonough, W.F. (1989). Chemical and isotopic systematics of oceanic basalts: implications for mantle composition and processes. *Geological Society, London, Special Publications,* **42**, 313-345.

Tang, Y., Sun, D., Gou, J., Ni, X., Zeng, X., Zhang, X., Liu, W., Liang, S., and Deng, C. (2025). Chalcopyrite geochemistry: Advancements and implications in ore deposit research. *Ore Geology Reviews,* **179**, 106528.

Timberlake, S. (2014). Prehistoric Copper Extraction in Britain: Ecton Hill, Staffordshire. *Proceedings of the Prehistoric Society*, **80**, 159-206.

Torremans, K., Kyne, R., Doyle, R., Guven, J.F., and Walsh, J.J. (2018). Controls on Metal Distribution at the Lisheen and Silvermines Deposits: Insights into Fluid Flow Pathways in Irish-Type Zn-Pb Deposits. *Economic Geology*, **113**(7), 1455-1477.

Upton, B.G.J., Stephenson, D., Smedley, P.M., Wallis, S.M., and Fitton, J.G. (2004). Carboniferous and Permian magmatism in Scotland. *Geological Society, London, Special Publications,* **223**, 195-218.

Wang, J., Chang, J., Li, C., Han, Z., Wang, T., and Han, H. (2020). Significance of Calcite Trace Elements Contents and C-O Isotopic Compositions for Ore-Forming Fluids and Gold Prospecting in the Zhesang Carlin-Like Gold Deposit of Southeastern Yunnan, China. *Minerals*, **10**(4), 338.

Wang, L., Qin, K., Song, G., Li, G. (2019). A review of intermediate sulfidation epithermal deposits and subclassification. *Ore Geology Reviews*, **107**, 434-456.

Watson, E.B. (2004). A conceptual model for near-surface kinetic controls on the trace-element and stable isotope composition of abiogenic calcite crystals. *Geochimica et Cosmochimica Acta*, **68**(7), 1473-1488.

Watson, J.J.W. (1860). Notes on the metalliferous saddles of Derbyshire and Staffordshire. *The Geologist*, **3**, 357-369.

Warrington, G. (2012). Mineralization in the Triassic rocks of the Cheshire Basin with particular reference to Alderley Edge, Cheshire, and Clive, Shropshire. *Proceedings of the Shropshire Geological Society*, **17**, 33-39.

Wei, C., Frenzel, M., Ye, L., de Oliveira, S.B., Danyushevsky, L., Huang, Z., and Gutzmer, J. (2025). Sphalerite Chemistry and Carbonate (C, O) Isotope Zonation in the Nayongzhi Mississippi Valley-Type Deposit, Southwest China. *Economic Geology*, **120**(7), 1751-1776.

Wilkinson, J.J. (2014). Sediment-Hosted Zinc-Lead Mineralization: Processes and Perspectives. *In* H.D. Holland, and K.K. Turekian (Eds.), *Treatise on Geochemistry (Second Edition)* (p. 219-249). Elsevier.

Wilkinson, J.J. (2023). Tracing metals from source to sink in Irish-type Zn-Pb(-Ba-Ag) deposits. *In* C.J. Andrew, M.W. Hitzman, and G. Stanley (Eds.), *Irish-type Deposits around the world* (p. 147-168). Irish Association for Economic Geology, Dublin.

Wilson, M., Neumann, E.-R., Davies, G.R., Timmerman, M.J., Heeremans, M., and Larsen, B.T. (2004) Permo-Carboniferous magmatism and rifting in Europe: introduction. *Geological Society, London, Special Publications*, **223**, 1-10.

Wilson, S.A., Ridley, W.I., and Koenig, A.E. (2002). Development of sulfide calibration standards for the laser ablation inductively-coupled plasma mass spectrometry technique. *Journal of Analytical Atomic Spectrometry*, **17**(4), 406-409.

Zhong, R., Brugger, J., Chen, Y., and Li, W. (2015). Contrasting regimes of Cu, Zn and Pb transport in ore-forming hydrothermal fluids. *Chemical Geology*, **395**, 154-164.

Appendix

Table A1: EPMA data for chalcopyrite from Ecton samples

Analysis #	S (wt. %)	Bi (wt. %)	Zn (wt. %)	Te (wt. %)	Pb (wt. %)	Sb (wt. %)	Fe (wt. %)	Co (wt. %)	Ni (wt. %)	Cu (wt. %)	Se (wt. %)	As (wt. %)	Cd (wt. %)
Sample 1													
Ccp 1	35.06	0.06		0.00	0.01	0.01	30.47	0.02		34.63			
Ccp 2	35.21	0.04					30.43	0.03		34.77			
Ccp 3	35.03	0.07					29.90	0.04		34.52			
Ccp 4	35.18						30.59	0.03		35.05			
Ccp 5	35.60	0.08	0.10				30.61	0.05		35.03			
Ccp 6	35.36	0.08				0.01	30.68	0.04		35.05			
Ccp 7	35.34			0.01			30.38	0.02		34.89			
Ccp 8	35.22	0.04					30.41	0.03		34.89			
Ccp 9	35.26	0.00				0.01	30.53	0.03		35.15			
Ccp 10	35.13	0.03					30.35	0.03		34.78			
Ccp 11	35.17	0.05	0.03	0.00			30.08	0.02		34.72			
Ccp 12	35.19			0.01			30.20	0.03		34.51			
Ccp 13	35.10						30.19	0.04		34.58		0.00	
Ccp 14	35.21	0.02					30.26	0.04		34.66			
Ccp 15	35.14	0.05				0.01	30.38	0.03		34.84			
Ccp 16	35.05	0.07		0.01		0.00	30.49	0.03		34.86			
Ccp 17	35.30	0.01	0.05			0.00	30.51	0.04		35.00			
Ccp 18	35.15						30.44	0.04		34.73			
Ccp 19	35.46	0.03				0.00	30.66	0.03		34.97			
Ccp 20	35.12	0.11				0.01	30.44	0.03		34.73		0.01	
Ccp 21	35.41	0.00					30.65	0.04		34.84			
Ccp 22	35.25	0.04					30.62	0.03		35.00			
Ccp 23	35.38	0.08	0.04	0.02			30.60	0.01		35.06			
Ccp 24	35.01						30.56	0.04		34.77			

Table A1 (con't): EPMA data for chalcopyrite from Ecton samples

Analysis #	S (wt. %)	Bi (wt. %)	Zn (wt. %)	Te (wt. %)	Pb (wt. %)	Sb (wt. %)	Fe (wt. %)	Co (wt. %)	Ni (wt. %)	Cu (wt. %)	Se (wt. %)	As (wt. %)	Cd (wt. %)
Sample 1													
Ccp 25	35.19	0.10		0.01			30.20	0.02		34.75			
Ccp 26	35.13	0.05	0.02				30.40	0.02		35.01			
Ccp 27	35.24		0.02			0.01	30.23	0.03		34.98			
Ccp 28	35.36	0.09		0.01		0.00	30.35	0.04		34.86			
Ccp 29	35.62	0.08					30.31	0.04		35.01			
Ccp 30	35.38						30.36	0.04		35.09			
Ccp 31	35.45	0.04					30.40	0.03		34.99			
Ccp 32	35.48	0.06		0.00	0.01	0.02	30.65	0.04		34.87			
Ccp 33	35.37	0.01					30.42	0.02		34.87			
Ccp 34	35.48	0.04	0.00	0.00			30.65	0.03		34.99			
Ccp 35	35.42	0.07		0.01		0.02	30.49	0.04		35.08			
Ccp 36	35.67					0.01	30.45	0.04		35.01			
Ccp 37	35.47	0.05	0.04				30.36	0.03		34.90			
Sample 2													
Ccp 1	35.54					0.01	30.49	0.04		35.15			
Ccp 2	35.46						30.48	0.03		35.05			
Ccp 3	35.38	0.12					30.51	0.02		34.89			
Ccp 4	35.52	0.00		0.00			30.61	0.03		34.98			
Ccp 5	35.10	0.01					30.61	0.04		34.73			
Ccp 6	35.54	0.04					30.51	0.03		34.96			
Ccp 7	35.63	0.08		0.02			30.47	0.03		34.99			
Ccp 8	35.51	0.01	0.06				30.60	0.04		35.01			
Ccp 9	35.79	0.07					30.51	0.04		34.98			
Ccp 10	35.66	0.02		0.01			30.27	0.03		34.76			
Ccp 11	34.34	0.02					17.36	0.02		21.74			
Ccp 12	35.66	0.03				0.01	30.52	0.03		35.16			
Ccp 13	35.62	0.05					30.55	0.03		35.06			
Ccp 14	35.65	0.02		0.00			30.66	0.04		35.12			

Table A1 (con't): EPMA data for chalcopyrite from Ecton samples

Analysis #	S (wt. %)	Bi (wt. %)	Zn (wt. %)	Te (wt. %)	Pb (wt. %)	Sb (wt. %)	Fe (wt. %)	Co (wt. %)	Ni (wt. %)	Cu (wt. %)	Se (wt. %)	As (wt. %)	Cd (wt. %)
Sample 2													
Ccp 15	35.45	0.05					29.50	0.03		34.32			
Ccp 16	35.54	0.04					30.58	0.03		34.92			
Ccp 17	35.91	0.06					30.31	0.04		34.76			
Ccp 18	35.52			0.00			30.22	0.02		34.79			
Ccp 19	35.43				0.03		30.39	0.03		34.84			
Ccp 20	35.49	0.05	0.02				30.50	0.04		34.63			
Ccp 21	35.42						30.37	0.03		34.97			
Ccp 22	35.54		0.04				30.30	0.03		34.71			
Ccp 23	35.52						30.65	0.04		34.98			
Ccp 24	35.64	0.10					30.30	0.04		34.88			
Ccp 25	35.76	0.05					30.55	0.03		34.89			

Table A2: EPMA data for marcasite from Ecton samples

Analysis #	S (wt. %)	Bi (wt. %)	Zn (wt. %)	Te (wt. %)	Pb (wt. %)	Sb (wt. %)	Fe (wt. %)	Co (wt. %)	Ni (wt. %)	Cu (wt. %)	Se (wt. %)	As (wt. %)	Cd (wt. %)
Sample 1													
Mrc 1	53.34	0.07		0.00			44.87	0.04		2.08		0.24	
Mrc 2	53.20	0.05				0.01	45.29	0.06	0.04	1.55		0.40	
Mrc 3	53.31	0.09	0.06				45.14	0.06		1.32		0.01	
Mrc 4	53.56		0.01				45.54	0.06		1.02			
Mrc 5	53.36	0.00	0.03				45.05	0.07		1.13			
Mrc 6	53.80	0.08	0.05				45.79	0.04		1.23		0.07	
Mrc 7	53.70	0.05		0.01		0.02	46.31	0.05		0.56		0.01	
Mrc 8	53.72					0.01	46.19	0.06	0.01	0.97		0.07	
Mrc 9	53.52	0.04		0.00			45.92	0.06		0.70		0.05	
Mrc 10	53.44	0.11					45.85	0.05	0.01	0.37		0.00	
Mrc 11	53.54	0.05				0.00	46.46	0.06		0.40		0.02	
Sample 2													
Mrc 1	53.59	0.06		0.01	0.09	0.02	45.85	0.05	0.56	0.16		0.04	
Mrc 2	53.31	0.00	0.03			0.02	45.96	0.06	0.15	0.27		0.12	
Mrc 3	53.89	0.06		0.00			46.30	0.06	0.07	0.07		0.44	
Mrc 4	53.63	0.05					46.11	0.05	0.12	0.40		0.10	
Mrc 5	53.13	0.11					44.33	0.12	0.82	1.48		0.82	
Mrc 6	53.14	0.06	0.02	0.00			44.87	0.18	0.71	0.61		0.15	
Mrc 7	53.85						46.12	0.06		0.65			
Mrc 8	53.37	0.00		0.02			45.39	0.06		0.50		0.02	
Mrc 9	52.92	0.03	0.01				44.70	0.09	0.22	1.40		0.95	
Mrc 10	53.98	0.02	0.01	0.01			45.99	0.07	0.01	0.47			
Mrc 11	53.37	0.03	0.04		0.01	0.02	45.82	0.06	0.09	0.22		0.11	
Mrc 12	53.45	0.03			0.15	0.03	46.26	0.05		0.45		0.04	
Mrc 13	53.34	0.10	0.02	0.02	0.04		44.47	0.20	1.43	1.31		0.43	
Mrc 14	53.74	0.07	0.02			0.00	45.77	0.11	0.72	0.48		0.31	

Table A2 (con't): EPMA data for marcasite from Ecton samples

Analysis #	S (wt. %)	Bi (wt. %)	Zn (wt. %)	Te (wt. %)	Pb (wt. %)	Sb (wt. %)	Fe (wt. %)	Co (wt. %)	Ni (wt. %)	Cu (wt. %)	Se (wt. %)	As (wt. %)	Cd (wt. %)
Sample 2													
Mrc 15	53.26	0.07		0.01		0.02	46.02	0.05	0.12	0.38		0.37	
Mrc 16	53.77	0.02				0.01	46.00	0.05	0.05	0.66		0.10	
Mrc 17	53.54	0.05	0.03			0.02	46.42	0.05		0.15			
Mrc 18	53.77	0.02					45.91	0.06	0.06	0.18		0.21	
Mrc 19	53.69	0.04				0.03	46.40	0.05	0.01	0.23		0.06	
Mrc 20	53.64	0.07			0.01	0.03	45.55	0.07	0.26	0.51		0.06	
Mrc 21	51.76	0.04		0.01			44.89	0.06		1.13		2.09	
Mrc 22	53.23	0.04	0.01				45.70	0.07	0.09	0.51		0.29	
Mrc 23	53.76	0.09					46.21	0.06	0.19	0.11			

Table A3: EPMA data for Ni-rich pyrite from Ecton samples

Analysis #	S (wt. %)	Bi (wt. %)	Zn (wt. %)	Te (wt. %)	Pb (wt. %)	Sb (wt. %)	Fe (wt. %)	Co (wt. %)	Ni (wt. %)	Cu (wt. %)	Se (wt. %)	As (wt. %)	Cd (wt. %)
Sample 2													
Ni-Py 1	53.51	0.11		0.00	0.07		42.42	0.50	4.44	1.84		0.57	
Ni-Py 2	53.46	0.02		0.00			33.85	1.87	15.42	0.58		0.45	
Ni-Py 3	52.78	0.10		0.02	0.00		30.40	1.99	12.94	0.63		0.44	
Ni-Py 4	53.72	0.08		0.01	0.02	0.01	37.67	0.93	10.60	0.53		0.45	
Ni-Py 5	53.31	0.06		0.01			28.17	2.96	18.66	0.18		0.63	
Ni-Py 6	53.22	0.01	0.02	0.03			33.98	1.10	9.58	1.40		0.41	

Table A4: EPMA data for pyrite from Ecton samples

Analysis #	S (wt. %)	Bi (wt. %)	Zn (wt. %)	Te (wt. %)	Pb (wt. %)	Sb (wt. %)	Fe (wt. %)	Co (wt. %)	Ni (wt. %)	Cu (wt. %)	Se (wt. %)	As (wt. %)	Cd (wt. %)
Sample 2													
Py 1	53.73			0.00		0.01	46.54	0.04		0.08			
Py 2	53.80					0.00	46.82	0.05	0.01	0.03			

Table A5: EPMA data for galena from Ecton samples

Analysis #	S (wt. %)	Bi (wt. %)	Zn (wt. %)	Te (wt. %)	Pb (wt. %)	Sb (wt. %)	Fe (wt. %)	Co (wt. %)	Ni (wt. %)	Cu (wt. %)	Se (wt. %)	As (wt. %)	Cd (wt. %)
Sample 1													
Gal 1	13.47	0.18		0.01	86.00	0.02	0.01		0.00				
Gal 2	13.49	0.22		0.05	85.38		0.02	0.00		0.00			
Sample 2													
Gal 1	13.69	0.12		0.02	87.03		0.31	0.00		0.34			
Gal 2	13.50	0.20			87.41		0.76	0.00		0.47			

Table A6: EPMA data for gersdorffite from Ecton samples

Analysis #	S (wt. %)	Bi (wt. %)	Zn (wt. %)	Te (wt. %)	Pb (wt. %)	Sb (wt. %)	Fe (wt. %)	Co (wt. %)	Ni (wt. %)	Cu (wt. %)	Se (wt. %)	As (wt. %)	Cd (wt. %)
Sample 2													
Grf 1	19.30			0.01		0.02	2.34	3.31	29.80	0.07	0.09	44.34	
Grf 2	19.88	0.03		0.01	0.01		2.04	4.69	27.18	0.14	0.04	42.51	
Grf 3	6.37				0.05	0.06	0.74	4.66	27.53	0.03		49.05	

Table A7: EPMA data for calcite from Ecton samples

Analysis #	SiO2 (wt. %)	Al2O3 (wt. %)	FeO (wt. %)	MnO (wt. %)	MgO (wt. %)	CaO (wt. %)	SrO (wt. %)	BaO (wt. %)	Na2O (wt. %)	K2O (wt. %)	P2O5 (wt. %)	SO3 (wt. %)	CO2 (wt. %)	O (wt. %)
Sample 1														
Cal 1	0.01			0.16	0.09	57.26				0.01	0.04	0.00	43.58	
Cal 2				0.16	0.04	57.68	0.02	0.01	0.01	0.01	0.02		43.48	
Cal 3	0.01		0.18	0.12	0.15	56.52	0.00		0.06	0.02			43.68	
Cal 4	0.02		0.36	0.12	0.19	56.59			0.03	0.02		0.01	43.61	
Cal 5	0.01		0.23	0.08	0.16	56.77	0.01		0.07	0.02	0.02		43.61	
Cal 6	0.01		0.02	0.13	0.21	56.27		0.01	0.01	0.02	0.02		43.79	0.00
Cal 7	0.01		0.26	0.10	0.15	56.20			0.07	0.02	0.04	0.01	43.73	
Cal 8			0.21	0.07	0.12	56.44		0.03	0.10	0.06			43.66	
Cal 9		0.00	0.04	0.27	0.10	56.83			0.08	0.05		0.09	43.60	
Cal 10	0.00		0.02	0.36	0.20	56.35			0.03	0.01	0.03	0.01	43.70	
Cal 11	0.02		0.01	0.17	0.19	56.30			0.07	0.05	0.02	0.02	43.75	
Cal 12				0.18	0.15	56.94		0.03		0.02	0.01		43.62	
Cal 13			0.15	0.10	0.14	56.60		0.01		0.02	0.01	0.00	43.69	
Cal 14	0.02		0.15	0.07	0.19	55.38		0.01	0.01	0.03	0.02	0.01	43.97	0.00
Cal 15	0.01		0.13	0.01	0.16	56.40			0.00	0.02			43.76	
Cal 16	0.02		0.29	0.12	0.18	56.44			0.00	0.04	0.04	0.01	43.67	
Cal 17	0.02	0.00	0.02	0.29	0.09	56.83	0.01	0.01	0.08	0.03	0.05	0.06	43.61	0.00
Cal 18				0.34	0.14	56.26		0.03	0.16	0.07	0.01	0.04	43.67	0.00
Cal 19	0.01			0.05	0.13	56.79				0.01	0.00		43.71	
Cal 20			0.15	0.08	0.15	56.54				0.01	0.03		43.71	
Cal 21			0.17	0.11	0.15	56.24		0.01	0.02	0.02			43.75	
Cal 22	0.01		0.17	0.12	0.14	56.13			0.01	0.02	0.01		43.78	0.00
Cal 23	0.00		0.46	0.19	0.19	56.39			0.05	0.03		0.01	43.60	
Cal 24	0.02		0.02	0.36	0.10	56.11			0.01	0.02	0.00		43.77	0.00
Cal 25	0.01		0.02	0.33	0.12	56.09				0.01	0.02		43.78	
Cal 26	0.00		0.01	0.30	0.24	55.72		0.05		0.01	0.04		43.85	0.00
Cal 27	0.00		0.01	0.08	0.18	56.55				0.02	0.02		43.75	
Cal 28	0.01		0.14	0.18	0.20	56.81				0.02	0.04		43.62	0.00

Table A7 (con't): EPMA data for calcite from Ecton samples

Analysis #	SiO2 (wt. %)	Al2O3 (wt. %)	FeO (wt. %)	MnO (wt. %)	MgO (wt. %)	CaO (wt. %)	SrO (wt. %)	BaO (wt. %)	Na2O (wt. %)	K2O (wt. %)	P2O5 (wt. %)	SO3 (wt. %)	CO2 (wt. %)	O (wt. %)
Sample 1														
Cal 29	0.01		0.23	0.24	0.13	55.83			0.01	0.02	0.01	0.03	43.80	0.00
Cal 30				0.31	0.24	55.15			0.30	0.09	0.03	0.02	43.89	
Cal 31				0.26	0.25	56.39				0.02			43.72	0.00
Cal 32			0.01	0.10	0.13	56.59				0.02	0.05		43.74	0.00
Cal 33	0.00			0.09	0.13	56.33				0.01	0.00	0.00	43.80	0.00
Cal 34			0.12	0.13	0.14	56.22		0.03		0.01	0.04	0.01	43.77	
Cal 35	0.02		0.12	0.11	0.15	56.09				0.03	0.04		43.81	0.00
Cal 36	0.01		0.14	0.15	0.18	56.32			0.03	0.01	0.03		43.73	0.00
Cal 37	0.01		0.13	0.12	0.15	56.48			0.01	0.03			43.71	
Cal 38	0.02		0.12	0.09	0.12	56.81			0.25	0.08			43.57	
Cal 39			0.10	0.10	0.13	56.39			0.00	0.02	0.02	0.01	43.75	
Cal 40			0.12	0.06	0.17	56.32				0.01			43.77	
Cal 41			0.14	0.09	0.14	56.82			0.01	0.02	0.00		43.64	
Cal 42			0.17	0.06	0.21	56.14		0.01		0.02	0.02		43.79	0.00
Cal 43	0.01		0.28	0.29	0.19	55.93				0.02		0.07	43.75	0.00
Cal 44	0.00			0.19	0.07	56.89			0.01	0.02			43.64	0.00
Cal 45				0.11	0.08	57.41	0.01		0.00	0.02			43.55	
Cal 46	0.01		0.01	0.02	0.10	56.79				0.01	0.03		43.73	0.00
Cal 47			0.10	0.17	0.14	55.98				0.02	0.01	0.00	43.82	
Cal 48			0.13	0.04	0.16	56.16				0.00			43.81	
Cal 49	0.01		0.15	0.04	0.16	55.78			0.01	0.02	0.05		43.89	
Cal 50			0.07	0.40	0.15	56.92			0.02	0.03	0.02	0.01	43.55	
Cal 51	0.01		0.01	0.19	0.10	56.56				0.01	0.07		43.72	
Cal 52	0.00		0.01	0.04	0.09	56.53		0.01		0.02	0.02	0.02	43.77	0.00
Cal 53	0.00		0.08	0.19	0.07	56.75		0.02		0.01	0.07	0.05	43.66	
Cal 54	0.01		0.37	0.13	0.14	55.56		0.02	0.00	0.01	0.01	0.01	43.85	
Cal 55	0.00		0.18	0.10	0.20	55.98		0.06		0.01	0.00		43.79	
Cal 56	0.02		0.14	0.08	0.19	56.10				0.02			43.81	

Table A7 (con't): EPMA data for calcite from Ecton samples

Analysis #	SiO2 (wt. %)	Al2O3 (wt. %)	FeO (wt. %)	MnO (wt. %)	MgO (wt. %)	CaO (wt. %)	SrO (wt. %)	BaO (wt. %)	Na2O (wt. %)	K2O (wt. %)	P2O5 (wt. %)	SO3 (wt. %)	CO2 (wt. %)	O (wt. %)
Sample 1														
Cal 57	0.02		0.11	0.15	0.14	56.47	0.04		0.20	0.07			43.63	
Cal 58	0.00		0.07	0.08	0.08	55.94	0.02	0.02		0.02			43.86	0.00
Cal 59	0.01		0.06	0.12	0.08	56.73				0.00	0.01		43.69	
Cal 60			0.09	0.09	0.15	56.61		0.06		0.01	0.02		43.69	0.00
Sample 2														
Cal 1		0.00	0.15	0.15	0.26	56.05				0.03	0.02		43.79	
Cal 2	0.00		0.09	0.13	0.17	56.00			0.03	0.05	0.02	0.02	43.82	
Cal 3			0.14	0.18	0.19	56.34			0.01	0.02			43.72	0.00
Cal 4	0.00		0.01	0.12	0.07	56.24	0.02	0.02	0.00	0.02	0.02		43.80	0.00
Cal 5	0.00		0.18	0.16	0.13	55.79			0.02	0.01	0.02	0.01	43.85	0.00
Cal 6	0.01		0.14	0.21	0.23	55.55		0.02		0.02	0.01		43.88	
Cal 7	0.01		0.17	0.19	0.24	55.38				0.02		0.01	43.92	
Cal 8	0.01		0.32	0.29	0.26	55.32			0.00	0.01	0.03	0.01	43.87	0.00
Cal 9	0.00		0.16	0.14	0.32	55.40				0.03	0.04	0.01	43.93	0.00
Cal 10	0.01		0.17	0.11	0.16	55.88				0.02	0.02	0.03	43.85	
Cal 11	0.02		0.01	0.14	0.07	55.86				0.03	0.02	0.05	43.90	0.00
Cal 12	0.02		0.23	0.10	0.17	55.59				0.02	0.02		43.89	0.00
Cal 13	0.01		0.14	0.12	0.21	55.71				0.02	0.03	0.01	43.89	0.00
Cal 14	0.01		0.14	0.16	0.29	56.25				0.02	0.00		43.74	
Cal 15	0.18	0.02	0.34	0.12	0.23	55.34			0.00	0.02	0.04	0.04	43.92	
Cal 16	0.01		0.18	0.21	0.31	55.50				0.01	0.02		43.89	0.00
Cal 17	0.01			0.14	0.08	57.01				0.01	0.01		43.64	
Cal 18	0.01		0.16	0.18	0.28	55.94				0.02	0.03		43.80	0.00
Cal 19	0.01		0.15	0.26	0.21	55.81				0.02	0.03		43.82	0.00
Cal 20	0.00		0.20	0.22	0.24	56.18				0.01	0.03	0.00	43.73	
Cal 21	0.00		0.12	0.22	0.23	55.78	0.02			0.01	0.06	0.03	43.84	0.00
Cal 22	0.01			0.12	0.09	56.53			0.00	0.02	0.01	0.01	43.75	0.00
Cal 23	0.01		0.15	0.08	0.17	55.83			0.00	0.02	0.05	0.00	43.87	

Table A7 (con't): EPMA data for calcite from Ecton samples

Analysis #	SiO2 (wt. %)	Al2O3 (wt. %)	FeO (wt. %)	MnO (wt. %)	MgO (wt. %)	CaO (wt. %)	SrO (wt. %)	BaO (wt. %)	Na2O (wt. %)	K2O (wt. %)	P2O5 (wt. %)	SO3 (wt. %)	CO2 (wt. %)	O (wt. %)
Sample 2														
Cal 24	0.04	0.01	0.13	0.16	0.19	55.33			0.00	0.02	0.05	0.00	43.97	0.00
Cal 25	0.01		0.12	0.12	0.28	55.68				0.02	0.04	0.01	43.89	
Cal 26	0.01			0.21	0.10	56.30	0.01			0.02	0.03	0.01	43.78	
Cal 27	0.00		0.10	0.17	0.21	55.72				0.03			43.87	
Cal 28	0.04		0.03	0.18	0.08	56.49			0.02	0.02	0.04	0.00	43.73	
Cal 29			0.10	0.17	0.15	56.58		0.07		0.02		0.01	43.65	0.00
Cal 30	0.01		0.14	0.09	0.12	55.92				0.01	0.00	0.00	43.85	
Cal 31	0.00		0.03	0.04	0.09	55.85		0.00		0.02	0.07	0.00	43.92	
Cal 32			0.16	0.15	0.27	56.30	0.00			0.03	0.03		43.72	0.00
Cal 33	0.01		0.19	0.13	0.14	55.46	0.02		0.01	0.02	0.04		43.92	
Cal 34	0.01		0.20	0.22	0.16	55.26				0.02		0.01	43.94	
Cal 35	0.02		0.15	0.21	0.12	55.97				0.01	0.02	0.01	43.81	
Cal 36	0.01		0.15	0.16	0.19	55.93				0.01		0.00	43.82	
Cal 37	0.00		0.17	0.21	0.14	56.15				0.02	0.06		43.76	
Cal 38			0.21	0.16	0.17	56.60				0.02	0.00		43.65	
Cal 39	0.02		0.18	0.22	0.22	56.07	0.01			0.01		0.01	43.76	
Cal 40	0.02		0.24	0.15	0.16	55.71			0.01	0.03	0.02	0.01	43.84	
Cal 41	0.01		0.19	0.14	0.21	56.29				0.01			43.73	0.00
Cal 42	0.02		0.13	0.15	0.21	56.08			0.00	0.03	0.02		43.79	0.00
Cal 43	0.01		0.12	0.04	0.16	56.02				0.00	0.01		43.86	
Cal 44			0.01	0.23	0.07	56.71		0.02		0.01			43.67	0.00
Cal 45	0.01		0.09	0.13	0.16	56.13				0.01	0.02		43.80	
Cal 46	0.02		0.22	0.20	0.20	56.00	0.01			0.02			43.77	
Cal 47			0.15	0.22	0.22	56.25				0.03	0.01		43.72	0.00
Cal 48	0.02		0.16	0.15	0.20	55.90		0.08		0.01	0.04	0.01	43.80	0.00
Cal 49	0.01		0.20	0.15	0.22	55.61			0.00	0.01	0.01		43.88	
Cal 50	0.01		0.19	0.24	0.22	55.34				0.01	0.02	0.02	43.92	0.00
Cal 51	0.01		0.18	0.20	0.19	56.32		0.02		0.02	0.03		43.70	0.00

Table A7 (con't): EPMA data for calcite from Ecton samples

Analysis #	SiO2 (wt. %)	Al2O3 (wt. %)	FeO (wt. %)	MnO (wt. %)	MgO (wt. %)	CaO (wt. %)	SrO (wt. %)	BaO (wt. %)	Na2O (wt. %)	K2O (wt. %)	P2O5 (wt. %)	SO3 (wt. %)	CO2 (wt. %)	O (wt. %)
Sample 2														
Cal 52	0.01		0.23	0.11	0.24	55.03			0.00	0.02			44.01	
Cal 53	0.01		0.20	0.18	0.21	55.70				0.03	0.03		43.85	0.00
Cal 54	0.01		0.17	0.18	0.21	55.50				0.03	0.00		43.90	
Cal 55	0.01		0.19	0.17	0.20	55.34		0.04		0.02	0.02	0.00	43.92	
Cal 56	0.01		0.20	0.20	0.22	55.88				0.01	0.01		43.81	0.00
Cal 57	0.02		0.15	0.15	0.16	56.58				0.02	0.02	0.00	43.68	
Cal 58			0.20	0.17	0.25	55.76				0.02	0.00	0.01	43.84	
Cal 59	0.04		0.19	0.20	0.19	56.28			0.03	0.03		0.00	43.70	
Cal 60	0.00		0.20	0.16	0.19	55.77	0.04	0.04	0.03	0.03			43.80	0.00

Table A8: EPMA data for baryte from Ecton samples

Analysis #	SiO2 (wt. %)	Al2O3 (wt. %)	FeO (wt. %)	MnO (wt. %)	MgO (wt. %)	CaO (wt. %)	SrO (wt. %)	BaO (wt. %)	Na2O (wt. %)	K2O (wt. %)	P2O5 (wt. %)	SO3 (wt. %)	CO2 (wt. %)	O (wt. %)
Sample 1														
Bar 1		0.07	0.07			1.18	5.98	59.21	0.09	0.04	0.02	35.56		0.00
Bar 2	0.00	0.06	0.20			0.75	5.59	59.06	0.08	0.04		35.23		
Bar 3		0.08	0.06			0.77	5.61	60.13	0.08	0.04		35.68		
Bar 4		0.05	0.06			1.15	5.54	59.50	0.06	0.04		35.52		0.00
Bar 5		0.02	0.07			0.84	7.27	57.46	0.04	0.00		35.56		0.00
Bar 6		0.06	0.09			0.42	6.10	58.99	0.06	0.06		35.62		
Bar 7		0.05	0.17			0.89	5.54	60.38	0.10	0.03		35.60		
Sample 2														
Bar 1	9.54	1.05	0.37		0.09	0.62	0.43	55.79	0.08	0.28	0.07	29.16		0.00

Table A9: LA-ICP-MS data for chalcopyrite from Ecton *Sample 1* (ppm)

	Sample 1										
	Ccp 1	Ccp 2	Ccp 3	Ccp 4	Ccp 5	Ccp 6	Ccp 7	Ccp 8	Ccp 9	Ccp 10	Ccp 11
Si	0	1,900	0	400	0	0	0	100	0	1500	0
S	360,000	370,000	370,000	367,000	380,000	400,000	390,000	400,000	390,000	400,000	410,000
Ca	35	0	34	6	3	19	0	0	9	12	8
Ti	1.2	1.3	1.5	1.5	1.2	1.6	1.6	1.2	1.5	1.3	1.0
V	0.02	0.03	0.00	0.00	0.01	0.00	0.01	0.05	0.01	0.00	0.01
Cr	0.17	0.10	0.00	0.23	0.15	0.18	0.00	0.00	0.19	0.14	0.00
Mn	0.0	1.3	0.0	0.5	0.00	0.2	0.00	0.3	0.00	1.5	0.00
Fe	280,000	270,000	280,000	270,000	270,000	250,000	260,000	250,000	260,000	260,000	250,000
Co	0.7	0.5	0.5	0.6	0.6	0.2	0.3	0.5	0.5	0.2	1.0
Ni	0.16	0.18	0.16	0.19	0.21	0.04	0.06	0.11	0.06	0.04	0.10
Cu	360,000	360,000	360,000	360,000	350,000	350,000	340,000	350,000	350,000	340,000	340,000
Zn	7	6	9	7	7	6	5	18	25	8	9
Ga	1.50	0.81	1.75	1.15	1.37	0.39	0.84	0.36	0.24	0.63	1.49
Ge	360	200	300	420	440	130	220	322	320	100	677.41
As	0.0	0.2	2.4	0.0	0.1	0.6	0.2	0.9	3.2	2.1	0.4
Se	6	4	9	8	8	13	14	6	4	13	4
Sr	0.00	0.01	0.01	0.00	0.00	0.00	0.00	0.01	0.01	0.00	0.02
Zr	0.01	0.01	0.01	0.00	0.01	0.00	0.01	0.00	0.01	0.01	0.01
Mo	0.03	0.00	0.03	0.02	0.03	0.01	0.03	0.05	0.01	0.03	0.05
Ag	4.8	5.3	4.1	4.7	4.6	3.7	4.0	3.2	2.7	2.9	4.1
Ag	4.9	5.5	4.0	4.7	4.7	3.7	4.1	3.2	2.5	3.0	4.2
Cd	0.03	0.20	0.03	0.06	0.14	0.18	0.08	0.18	0.21	0.23	0.21
In	0.4	0.3	1.0	0.4	0.5	0.3	0.4	1.0	1.0	0.7	0.4
Sn	0.8	0.4	1.0	1.0	0.8	1.8	1.6	2.0	1.1	1.6	0.5
Sb	0	0	8	1	0	4	0	5	13	2	1
Te	0.03	0.06		0.06	0.02	0.03		0.00	0.01	0.17	0.07
Te	0.02		0.09	0.00	0.11		0.00	0.00	0.27	0.18	0.00
Ba	0.01	0.01	0.01	0.01	0.00	0.02	0.01	0.01	0.01	0.01	0.01
La	0.00			0.00	0.00	0.00	0.00	0.00	0.00	0.00	0.00

Gd	0.02		0.00	0.01	0.01	0.00	0.01		0.00	0.00	0.01
Yb	0.00	0.00	0.00	0.00	0.00				0.00	0.01	0.00
Hf	0.00	0.00	0.00	0.01	0.00			0.00			0.00
Ta		0.00	0.00		0.00	0.00	0.00	0.00	0.00		
W	0.01	0.01			0.01	0.01	0.01	0.01	0.01	0.01	0.01
Re		0.00			0.08	0.00	0.00		0.00		
Au	0.00	0.00	0.01	0.01	0.01	0.00	0.00	0.00	0.01	0.00	0.00
Tl	0.04	0.19	0.02	0.04	0.03	0.05	0.03	0.10	0.08	0.09	0.15
Pb	0.3	1.0	0.4	0.4	0.4	0.8	0.2	4.7	1.6	0.8	0.9
Bi			0.00	0.00	0.00		0.01	0.00	0.00	0.00	

Table A9 (con't): LA-ICP-MS data for chalcopyrite from Ecton *Sample 1* (ppm)

	Sample 1										
	Ccp 12	Ccp 13	Ccp 14	Ccp 15	Ccp 16	Ccp 17	Ccp 18	Ccp 19	Ccp 20	Ccp 21	Ccp 22
Si	900	600	400	0	0	1,100	400	0	1,400	0	300
S	400,000	430,000	410,000	400,000	420,000	390,000	410,000	400,000	390,000	400,000	400,000
Ca	32	0	52	47	63	27	26	7	33	0	33
Ti	1.2	1.5	1.4	1.1	1.1	1.3	1.1	1.1	1.1	1.0	1.1
V	0.00	0.00	0.03	0.00	0.00	0.28	0.00	0.89	0.01	0.00	0.00
Cr	0.25	0.00	0.06	0.12	0.43	0.70	0.00	0.00	0.05	0.34	0.28
Mn	0.9	0.4	0.8	0.0	0.0	1.5	0.7	0.0	2.0	0.0	0.7
Fe	250,000	240,000	250,000	260,000	250,000	260,000	250,000	260,000	260,000	260,000	260,000
Co	0.8	0.5	0.5	0.2	0.5	0.5	0.5	0.2	0.7	0.4	0.6
Ni	0.15	0.53	0.25	0.21	0.19	0.21	0.14	0.00	0.00	0.18	0.19
Cu	350,000	330,000	340,000	340,000	330,000	340,000	330,000	340,000	350,000	350,000	340,000
Zn	10	10	7	8	16	13	7	11	8	25	19
Ga	1.68	0.29	1.02	0.63	0.17	0.50	0.61	0.46	1.08	0.31	0.29
Ge	600	300	500	100	300	300	400	100	500	300	400
As	9.0	10.8	2.1	0.7	2.1	1.0	0.5	0.2	0.2	3.8	10.3

Se	6	4	7	12	7	9	12	15	6	8	7
Sr	0.01	0.01	0.00	0.00	0.01	0.01	0.01	0.00	0.01	0.00	0.00
Zr	0.01	0.01	0.01	0.01	0.01	0.01	0.00	0.01	0.00	0.01	0.01
Mo	0.04	0.05	0.05	0.04	0.03	0.04	0.03	0.04	0.05	0.05	0.02
Ag	2.2	7.2	4.5	3.9	3.7	6.1	2.2	2.9	5.5	4.1	4.0
Ag	2.2	6.9	4.6	3.9	3.8	6.0	2.3	2.9	5.3	4.1	4.0
Cd	0.04	0.21	0.16	0.19	0.20	0.04	0.08	38.32	0.09	0.15	0.14
In	0.8	0.4	0.4	0.8	0.8	0.9	0.6	2.3	0.4	0.8	1.0
Sn	1.8	1.8	1.1	0.9	0.8	3.3	3.0	1.2	1.5	1.4	1.5
Sb	23	2	5	3	8	7	2	2	1	12	34
Te	0.11	0.02	0.06	0.07	0.11	0.02	0.02	0.03	0.03	0.01	0.06
Te	0.09	0.09	0.00	0.16	0.17	0.00	0.18	0.26	0.00	0.10	0.41
Ba	0.00		0.01		0.01	0.01	0.01	0.01		0.01	
La	0.00	0.00		0.00	0.00	0.00	0.00	0.00	0.00		0.00
Gd	0.01		0.01	0.01	0.00	0.01	0.01	0.02	0.01	0.00	
Yb						0.01	0.01	0.01	0.00		
Hf	0.00		0.00		0.01		0.01	0.00	0.00	0.00	0.00
Ta	0.00	0.00	0.00		0.00		0.00	0.00	0.00		0.00
W	0.00	0.01		0.01	0.01		0.01	0.00		0.00	0.01
Re			0.00			0.00	0.00		0.00		
Au		0.00	0.00	0.00	0.01	0.00	0.01	0.00	0.00	0.00	0.00
Tl	0.06	0.19	0.05	0.13	0.14	0.21	0.03	0.12	0.05	0.11	0.13
Pb	0.9	0.7	0.6	0.9	1.4	2.0	1.4	1.0	0.4	1.8	4.1
Bi	0.00		0.00		0.00		0.00		0.01	0.01	0.00

Table A10: LA-ICP-MS data for chalcopyrite from Ecton *Sample 2* (ppm)

	Sample 2									
	Ccp 1	Ccp 2	Ccp 3	Ccp 4	Ccp 5	Ccp 6	Ccp 7	Ccp 8	Ccp 9	Ccp 10
Si	1,900	0	0	300	0	100	500	400	0	0
S	360,000	370,000	360,000	370,000	360,000	360,000	390,000	370,000	370,000	360,000
Ca	130	24	1	20	0	31	41	37	51	17
Ti	0.8	1.8	0.9	1.1	1.0	1.1	0.9	1.4	1.3	0.6
V	0.00	0.01	0.00	0.01	0.00	0.00	0.04	0.00	0.00	0.00
Cr	0.29	0.16	0.00	0.32	0.03	0.28	0.00	0.38	0.41	0.20
Mn	1.9	0.00	0.00	0.1	0.00	0.00	0.2	0.3	0.00	0.00
Fe	280,000	280,000	280,000	280,000	280,000	280,000	280,000	280,000	280,000	280,000
Co	0.6	0.1	0.6	0.3	0.2	0.1	0.4	0.2	0.4	0.2
Ni	0.98	0.24	0.02	0.24	0.08	1.01	0.04	0.09	0.48	0.11
Cu	360,000	350,000	360,000	350,000	360,000	360,000	330,000	340,000	350,000	360,000
Zn	11	8	6	8	12	14	16	17	19	16
Ga	0.36	0.84	2.10	1.14	0.29	0.07	0.42	0.09	0.23	0.18
Ge	200	0	200	100	100	0	100	0	100	100
As	6.6	0.5	0.0	1.4	0.2	0.1	1.9	1.7	0.3	0.1
Se	10	18	5	15	5	3	5	4	3	5
Sr	0.01	0.01	0.01	0.02	0.00	0.05	0.01	0.01	0.02	0.00
Zr	0.01	0.01	0.02	0.01	0.01	0.00	0.01	0.00	0.00	0.01
Mo	0.27	0.03	0.05	0.03	0.04	0.02	0.05	0.03	0.06	0.02
Ag	0.5	3.2	1.0	0.9	0.5	2.3	0.6	0.7	0.4	0.7
Ag	0.5	3.0	1.0	0.9	0.4	2.3	0.6	0.8	0.4	0.8
Cd	0.24	0.24	0.20	0.19	0.86	0.31	0.36	0.66	0.24	0.14
In	0.8	1.8	0.5	1.6	1.3	0.6	1.3	1.1	1.1	1.3
Sn	1.0	0.7	0.5	1.8	0.2	0.4	0.4	0.7	0.3	0.1
Sb	13	8	0	8	2	0	10	0	3	1
Te	0.03	0.05	0.06	0.04	0.00	0.00	0.00	0.00	0.04	0.11
Te	0.14	0.00	0.13	0.16	0.00	0.00	0.21	0.13	0.00	0.06
Ba	0.01	0.03	0.06	0.08	0.01	0.01	0.03	0.03	0.01	0.00
La		0.00				0.00	0.00	0.00	0.00	0.00

Gd	(0.00)	0.00	0.01	0.03	0.03	0.00	0.01	0.02	0.02	0.01
Yb	0.01		0.00	-	0.00	0.00	0.00	0.00		
Hf			0.00	0.00		0.00	0.00		0.00	0.00
Ta				0.00						0.00
W		0.01	0.01	0.01	0.01	0.00	0.00	0.01	0.01	0.01
Re		0.00		0.00		0.01		0.00		0.00
Au		0.01		0.01			0.00	0.01		0.00
Tl	0.03	0.13	0.09	0.04	0.08	0.03	0.04	0.03	0.10	0.03
Pb	3.3	11.2	0.5	12.4	0.6	0.7	5.9	0.2	0.7	1.8
Bi	0.00	0.00		0.00		0.00	0.00	0.00		

Table A10 (con't): LA-ICP-MS data for chalcopyrite from Ecton *Sample 2* (ppm)

	Sample 2					
	Ccp 11	Ccp 12	Ccp 13	Ccp 14	Ccp 15	Ccp 16
Si	0	400	500	2,100	1,200	700
S	360,000	360,000	360,000	370,000	370,000	370,000
Ca	122	0	0	54	34	0
Ti	0.7	0.7	1.0	0.9	0.7	0.4
V	0.02	0.03	0.00	0.00	0.00	0.01
Cr	0.19	0.00	0.00	0.23	0.41	0.25
Mn	0.0	0.7	0.4	3.7	2.2	0.9
Fe	280,000	280,000	280,000	270,000	280,000	280,000
Co	0.5	0.5	0.1	1.3	1.7	0.8
Ni	0.03	0.10	0.00	0.50	0.11	0.07
Cu	360,000	360,000	360,000	360,000	350,000	350,000
Zn	21	6	28	13	6	6
Ga	0.25	1.27	0.12	0.09	0.08	0.06
Ge	100	200	0	200	200	100
As	3.6	4.1	0.3	0.7	0.3	0.5
Se	4	5	6	8	6	7
Sr	0.00	0.00	0.01	0.02	0.01	0.54

Zr	0.00	0.00	0.00	0.01	0.00	0.00
Mo	0.06	0.06	0.03	0.03	0.01	0.00
Ag	0.6	0.8	0.9	2.1	1.2	0.7
Ag	0.5	0.8	1.0	2.0	1.2	0.8
Cd	0.18	0.21	0.14	0.38	0.03	0.17
In	1.4	0.9	1.0	0.7	0.9	0.9
Sn	0.9	1.4	1.2	0.0	0.2	0.1
Sb	29	8	1	41	9	45
Te	0.06	0.15	0.04	0.04	0.07	0.06
Te	0.00	0.00	0.00	0.28	0.00	0.00
Ba	0.00		0.01	0.02		
La	0.00	0.00	0.00	0.00	0.00	
Gd	0.00	0.00	0.01	0.01	0.00	0.00
Yb	0.01	0.01	0.00	0.00	0.00	
Hf	0.01	0.01	0.00		0.00	
Ta	0.00	0.00	0.00		0.00	
W	0.01	0.01	0.01	0.00	0.01	0.00
Re			0.00	0.00	0.00	
Au	0.00	0.00	0.00	0.00	0.00	0.00
Tl	0.03	0.12	0.07	0.49	0.45	0.58
Pb	2.8	0.9	2.7	34.9	1.9	32.5
Bi	0.00	0.00	0.00	0.00	0.00	0.01

Table A11: LA-ICP-MS data for marcasite from Ecton *Sample 2* (ppm)

	Sample 2								
	Mrc 1	Mrc 2	Mrc 3	Mrc 4	Mrc 5	Mrc 6	Mrc 7	Mrc 8	Mrc 9
Si	0	0	0	0	0	0	0	40	0
S	530,000	490,000	530,000	540,000	550,000	550,000	530,000	530,000	530,000
Ca	22	62	15	121	2	7	41	33	20
Ti	2.2	1.6	1.9	1.7	1.7	1.5	1.6	1.5	1.6
V	0.00	0.03	0.02	0.00	0.00	0.01	0.00	0.01	0.02
Cr	0.00	0.25	0.00	0.00	0.07	0.16	0.01	0.11	0.12
Mn	0.0	0.0	0.0	0.3	0.0	0.0	0.1	0.1	0.0
Fe	460,000	510,000	450,000	450,000	440,000	450,000	450,000	460,000	460,000
Co	67	140	11	12	180	13	170	120	350
Ni	2000	2,800	170	670	3,100	390	2,700	1,600	2,200
Cu	3,900	3,400	11,000	1,100	5,900	1,900	8,000	7,000	3,000
Zn	2	3	1	1	4	0	1	2	0
Ga	0.02	0.01	0.01	0.00	0.01	0.01	0.03	0.05	0.01
Ge	0.06	7	0.1	0.1	0	1.1	12	43	1.4
As	2,800	900	1,900	2,600	3,400	1,300	700	500	400
Se	1	7	1	1	1	21	5	12	15
Sr	0.03	0.17	0.02	0.08	0.04	0.22	0.14	0.13	0.18
Zr	0.00	0.00	0.00	0.01	0.00	0.00	0.01	0.00	0.01
Mo	0.05	0.94	0.04	0.02	0.07	1.29	1.52	0.72	0.28
Ag	13	65	29	4	32	14	14	9	51
Ag	12	61	28	4	33	14	14	10	51
Cd	0.02	0.62	0.35	0.05	0.13	0.14	0.23	0.12	0.05
In	0.01	0.23	0.33	0.01	0.02	0.18	0.49	0.55	0.02
Sn	0.00	0.71	0.50	0.01	0.00	1.15	0.67	0.93	0.27
Sb	18	290	400	11	41	110	190	230	170
Te	0.01	0.03	0.03	0.04	0.05	0.04	0.01	0.02	0.01
Te	0.00	0.00	0.00		0.00	0.01	0.01	0.04	0.00
Ba	0.02	0.04	0.06	0.01	0.02	0.00	0.01	0.01	0.00
La	0.00	0.00	0.00	0.00	0.00	0.00	0.00	0.00	0.00

Gd	0.01	0.01	0.00	0.01	0.01	0.00	0.01	0.01	0.00
Yb			0.00	0.00	0.00			0.00	
Hf			0.00	0.00	0.00		0.00	0.00	
Ta					0.00		0.00	0.00	
W	0.00		0.01	0.01	0.00		0.00	0.00	0.00
Re			0.00			0.00	0.00	0.00	
Au	0.01		(0.00)	0.00	0.00	0.00	0.00	0.00	
Tl	1.3	9.9	34	0.4	4.1	1.8	4.6	4.2	1.7
Pb	140	1,200	50	70	350	280	940	590	730
Bi		0.00	0.00	0.00	0.00	0.00	0.00	0.01	0.01

Table A11 (con't): LA-ICP-MS data for marcasite from Ecton *Sample 2* (ppm)

	Sample 2							
	Mrc 10	Mrc 11	Mrc 12	Mrc 13	Mrc 14	Mrc 15	Mrc 16	Mrc 17
Si	0	0	100	0	100	0	0	0
S	530,000	540,000	550,000	540,000	550,000	530,000	530,000	540,000
Ca	7	39	23	24	13	2	11	0
Ti	1.6	1.6	1.7	1.9	2.1	1.4	1.5	1.6
V	0.00		0.01	0.04	0.02	0.00	0.01	
Cr	0.02	0.20	0.14	0.13	0.23	0.10	0.14	0.08
Mn	0.0	0.1	0.2	0.0	0.4	0.1	0.1	0.0
Fe	460,000	450,000	450,000	460,000	440,000	460,000	460,000	450,000
Co	12	22	20	22	190	70	170	31
Ni	400	300	300	800	2,700	1,600	2,700	2,500
Cu	2,400	6,200	600	2,200	1,900	2,500	3,000	2,900
Zn	0	1	1	1	1	1	1	150
Ga	0.01	0.01	0.00	0.01	0.01	0.01	0.01	0.01
Ge	2	1	14	3	2	3	5	2
As	3,300	1,300	1,200	2,300	3,700	2,900	2,600	3,300
Se	15	35	11	16	6	29	11	7
Sr	0.09	0.11	0.07	0.11	0.11	0.09	0.17	0.10

Zr	0.00	0.00	0.00	0.00	0.00	0.00	0.00	0.00
Mo	0.40	0.65	0.45	0.82	1.57	0.13	0.83	1.25
Ag	12	41	5	27	26	27	39	33
Ag	11	44	4	25	25	27	38	34
Cd	0.12	0.20	0.07	0.26	0.22	0.13	0.45	1.6
In	0.20	0.37	0.05	0.14	0.14	0.76	0.37	0.14
Sn	1.2	0.70	0.67	0.26	0.42	1.3	1.2	0.64
Sb	84	73	40	150	140	140	240	240
Te	0.02	0.00	0.00	0.02	0.08		0.01	0.03
Te	0.00	0.00	0.00	0.07		0.00	0.02	0.00
Ba	0.04	0.03	0.04	0.03	0.02	0.01	0.01	0.01
La	0.00	0.00	0.00	0.00	0.00	0.00	0.00	0.00
Gd	0.01	0.00	0.01	0.01	0.00	0.00	0.00	0.00
Yb	0.00	0.00		0.00	0.00	0.00	0.00	0.00
Hf	0.00	0.00	0.00		0.00	0.00	0.00	0.00
Ta	0.00		0.00	0.00	0.00			
W	0.00	0.00	0.00	0.00	0.00	0.00	0.00	
Re		0.00		0.00	0.00	0.00		
Au	0.00	0.00	0.00	0.00	0.00	(0.00)	0.00	0.00
Tl	2.0	4.3	0.6	3.7	5.0	3.6	7.1	4.1
Pb	230	720	110	520	480	500	790	680
Bi	0.00	0.01	0.00	0.00	0.00	0.00	0.00	0.01

Table A11 (con't): LA-ICP-MS data for marcasite from Ecton *Sample 2* (ppm)

	Sample 2							
	Mrc 18	Mrc 19	Mrc 20	Mrc 21	Mrc 22	Mrc 23	Mrc 24	Mrc 25
Si	300	0	100	0	100	0	500	0
S	520,000	530,000	540,000	530,000	530,000	490,000	510,000	530,000
Ca	1	31	8	8	0	11	6	37
Ti	1.6	1.3	1.4	1.4	1.3	1.1	1.2	1.2
V		0.00	0.01	0.00	0.00	0.14	0.01	0.01

Cr	0.14	0.02	0.06	0.00	0.00	0.09	0.12	0.24
Mn	0.7	0.0	0.5	0.0	0.4	0.0	1.3	0.0
Fe	470,000	460,000	460,000	460,000	460,000	500,000	480,000	460,000
Co	41	110	4	10	21	260	120	310
Ni	3,400	4,700	500	1,100	2,800	4,200	2,000	4,100
Cu	3,100	4,200	1,400	1,300	2,900	3,000	6,800	4,700
Zn	1	1	0	0	1	41	2	1
Ga	0.00		0.01	0.01	0.01	0.01	0.01	0.01
Ge	2	0.3	9	5	0.7	3	0.1	2
As	3,800	3,800	1,000	3,800	3,100	1,500	2,700	1,700
Se	5	6	7	4	2	12	0	10
Sr	0.09	0.09	0.05	0.08	0.12	0.38	0.03	0.77
Zr	0.00	0.00	0.00	0.00	0.00	0.00	0.00	0.00
Mo	0.59	0.93	0.24	0.41	0.47	5.0	0.03	0.29
Ag	34	38	17	11	48	43	23	59
Ag	31	39	16	12	46	44	24	63
Cd	0.21	0.29	0.25	0.13	0.70	1.6	0.06	0.37
In	0.13	0.10	0.29	0.09	0.15	0.25	0.01	0.28
Sn	0.92	0.46	1.00	0.23	0.15	0.76	0.01	0.93
Sb	220	160	65	75	350	230	29	200
Te	0.03	0.07	0.02	0.01	0.04	0.00	0.01	0.01
Te	0.07	0.03	0.00	0.03	0.00	0.00	0.00	0.00
Ba	0.00	0.01	0.00	0.01	0.01	0.01	0.01	0.03
La	0.00	0.00	0.00	0.00	0.00	0.00	0.00	0.00
Gd	0.00	0.00		0.01		0.01	0.00	0.00
Yb	0.00	0.00	0.00	0.00			0.00	0.00
Hf		0.00			0.00		0.00	
Ta	0.00			0.00	0.00	0.00		0.00
W	0.00		0.00	0.00	0.00		0.00	
Re			0.00	0.00	0.00			
Au	0.00	0.00	0.00	0.00	0.00			
Tl	4.9	3.7	2.4	1.8	7.4	6.5	3.4	5.7

Pb	690	640	340	240	1,100	700	250	1,000
Bi	0.00	0.00	0.00	0.00	0.00	0.01	0.00	0.00

Table A12: LA-ICP-MS data for pyrite varieties from Ecton *Sample 2* (ppm)

	Sample 2						
	Ni-Py 1	Ni-Py 2	Ni-Py 3	Ni-Py 4	Py-1 1	Py-1 2	Py-2 1
Si	900	0	0	300	0	0	700
S	460,000	480,000	480,000	520,000	540,000	550,000	520,000
Ca	34	23	32	44	0	1	12
Ti	2.0	1.0	0.7	1.2	1.5	1.3	1.1
V	0.02	0.00	0.00	0.03	0.00	0.01	0.08
Cr	0.02	0.00	0.35	0.24	0.06	0.12	0.14
Mn	1.5	0.1	0.0	0.7	0.0	0.0	1.3
Fe	320,000	380,000	430,000	310,000	460,000	450,000	460,000
Co	25,300	16,400	7,000	20,900	0.24	0.47	2.8
Ni	180,000	110,000	70,000	140,000	2	13	500
Cu	4,900	11,100	11,600	6,300	400	300	22,300
Zn	1.09	0.25	0.00	0.29	10.5	4.4	0.8
Ga	0.01	0.00		0.01	0.04	0.07	0.01
Ge	2.85	1.70	0.12	3.48	44	31	3
As	6,214	5,454	3,183	4,266	1	5	138
Se	463	273	8	530	8	9	5
Sr	0.18	0.06	0.51	0.37	0.02	0.02	0.03
Zr	0.02	0.00	0.00	0.01	0.00	0.00	0.00
Mo	0.28	0.11	0.05	0.11	0.02	0.04	0.13
Ag	33	42	50	36	1.3	1.3	7.2
Ag	34	44	51	35	1.4	1.4	7.5
Cd	0.03	0.05	0.09	0.15	0.07	0.11	0.19
In	0.02	0.02	0.01	0.01	0.89	0.94	0.97
Sn	0.01	0.00	0.01	0.01	0.62	0.62	0.01
Sb	35	53	67	50	4.4	2.7	59

Te	0.00	0.02	0.03	0.04	0.03	0.02	0.03
Te	0.00	0.05	0.03	0.02	0.00	0.02	0.00
Ba		0.01	0.02	0.01	0.01	0.00	0.00
La		0.00	0.00	0.00	0.00	0.00	0.00
Gd		0.01		0.01	0.01		0.01
Yb		0.00		0.00	0.00	0.00	
Hf		0.00			0.00	0.00	
Ta						0.00	
W	0.00	0.00	0.00	0.01	0.00	0.00	0.00
Re	0.01	0.01	0.00	0.00	0.00	0.00	0.00
Au	0.00	0.00	0.00	0.00	0.00	0.00	(0.00)
Tl	5.6	5.9	6.4	6.5	0.2	0.5	8.0
Pb	271	462	600	352	6	8	83
Bi	0.02	0.01	0.00	0.02		0.00	

Table A13: Stable isotope analysis on Ecton chalcopyrite

Analysis #	Weight (mg)	$\delta^{34}S$	Error (-0.3)	Error (+0.3)	%S
Sample 1					
1	0.085	**-15.27**	-15.57	-14.97	34.6
2	0.087	**-15.05**	-15.35	-14.75	25.1
3	0.091	**-15.52**	-15.82	-15.22	36.8
4	0.095	**-15.56**	-15.86	-15.26	37.5
5	0.095	**-15.57**	-15.87	-15.27	29.1
6	0.085	**-14.94**	-15.24	-14.64	22.4
Sample 2					
1	0.086	**-16.76**	-17.06	-16.46	32.2
2	0.091	**-16.66**	-16.96	-16.36	33.3
3	0.086	**-16.13**	-16.43	-15.83	36.2
4	0.093	**-16.56**	-16.86	-16.26	36.3
5	0.088	**-17.00**	-17.30	-16.70	36.3
6	0.088	**-16.84**	-17.14	-16.54	35.1

Table A14: LA-ICP-MS data for calcite from Ecton *Sample 1,* line traverse 1 (ppm)

	Sample 1										
	Cal 1	Cal 2	Cal 3	Cal 4	Cal 5	Cal 6	Cal 7	Cal 8	Cal 9	Cal 10	Cal 11
Mg^{25}	820	820	810	630	1080	1040	1060	1100	750	1140	1370
Si^{29}	3210	3150	3240	3210	3180	3140	3250	3250	3160	3180	3190
S^{34}	390	330	330	340	270	310	290	270	280	260	310
Mn^{55}	740	820	950	840	1280	1490	1560	1750	1670	2430	3050
Fe^{57}	195	196	196	196	193	194	197	192	193	193	193
Co^{59}	0.13	0.14	0.17	0.15	0.15	0.16	0.14	0.16	0.14	0.16	0.14
Ni^{60}	0.15	0.21	0.17	0.14	0.20	0.17	0.17	0.17	0.19	0.14	0.16
Cu^{65}	0.18	0.22	0.22	0.18	0.27	0.28	0.24	0.35	0.46	0.24	0.21
Zn^{66}		0.10		0.12	0.11	0.16	0.14	0.22	0.33		

Ge^{72}											
As^{75}	0.28	0.24	0.26	0.28	0.29	0.31	0.34	0.24	0.32	0.26	0.27
Sr^{88}	152	127	159	197	115	141	166	142	201	120	100
Y^{89}	12.6	11.8	12.9	12.0	7.1	6.4	6.2	5.8	5.3	4.5	4.2
Ag^{107}											
Ba^{137}			0.03	0.04			0.05	0.02	0.06		0.03
La^{139}	2.93	2.66	2.48	2.45	1.43	1.92	1.08	1.00	0.71	0.80	0.78
Ce^{140}	6.00	5.81	5.65	5.00	3.06	3.18	2.03	1.82	1.34	1.34	1.16
Pr^{141}	0.77	0.73	0.77	0.67	0.40	0.38	0.26	0.22	0.18	0.17	0.16
Nd^{146}	3.09	3.03	3.06	2.78	1.65	1.66	1.16	0.98	0.78	0.74	0.66
Sm^{147}	0.93	0.79	0.76	0.82	0.43	0.45	0.39	0.35	0.21	0.21	0.17
Eu^{151}	0.24	0.24	0.24	0.22	0.14	0.11	0.12	0.09	0.08	0.06	0.05
Gd^{157}	1.17	1.17	1.26	1.10	0.65	0.55	0.56	0.46	0.41	0.35	0.36
Tb^{159}	0.22	0.20	0.19	0.19	0.10	0.10	0.10	0.08	0.06	0.07	0.06
Dy^{163}	1.34	1.26	1.43	1.29	0.79	0.64	0.63	0.52	0.51	0.43	0.35
Ho^{165}	0.32	0.28	0.31	0.28	0.17	0.15	0.13	0.12	0.11	0.09	0.09
Er^{167}	0.87	0.73	0.85	0.83	0.47	0.45	0.37	0.34	0.29	0.29	0.25
Tm^{169}	0.13	0.10	0.12	0.11	0.07	0.05	0.06	0.04	0.04	0.04	0.03
Yb^{173}	0.87	0.71	0.75	0.72	0.53	0.35	0.34	0.31	0.28	0.22	0.22
Lu^{175}	0.12	0.10	0.11	0.11	0.07	0.06	0.05	0.04	0.03	0.03	0.03
Pb^{204}											
Pb^{206}	0.19	0.17	0.25	0.09	0.14		0.05	0.07			
Pb^{207}						0.05				0.03	
Pb^{208}											
Th^{232}	0.01	0.01	0.01	0.02	0.07	0.02	0.01	0.01		0.01	0.01
U^{238}	8.13	8.83	8.56	4.21	7.15	0.90	1.04	0.60	0.48	0.31	0.17

Table A14 (con't): LA-ICP-MS data for calcite from Ecton *Sample 1,* line traverse 1 (ppm)

	Sample 1										
	Cal 12	Cal 13	Cal 14	Cal 15	Cal 16	Cal 17	Cal 18	Cal 19	Cal 20	Cal 21	Cal 22
Mg^{25}	950	860	910	820	920	1260	1250	740	860	750	880
Si^{29}	3150	3110	3100	3100	3150	3080	2990	3050	3100	3200	3050
S^{34}	300	330	330	360	300	240	350	450	440	480	430
Mn^{55}	2420	2340	2590	2080	2110	3250	3090	2230	1970	1740	2310
Fe^{57}	192	192	192	195	233	230	211	253	457	596	418
Co^{59}	0.14	0.15	0.14	0.14	0.16	0.12	0.14	0.15	0.16	0.15	0.14
Ni^{60}	0.16	0.18	0.19	0.16	0.13	0.12	0.17	0.17	0.16	0.12	0.15
Cu^{65}	0.21	0.19	0.17	0.18	0.20	0.21	0.24	0.22	0.22	0.16	0.20
Zn^{66}		0.08	0.14	0.08	0.10		0.32	0.46	0.26	0.25	0.35
Ge^{72}											
As^{75}	0.25	0.32	0.40	0.43	0.27	0.27	0.32	0.31	0.38	0.33	0.32
Sr^{88}	156	191	169	225	180	61	169	303	270	292	236
Y^{89}	5.0	5.3	4.5	4.3	3.6	2.3	2.7	4.3	8.4	8.7	6.6
Ag^{107}											
Ba^{137}	0.04	0.05		0.04			0.09	0.23	0.16	0.20	0.12
La^{139}	1.33	1.30	1.84	0.92	0.84	0.43	0.55	0.54	1.42	1.27	1.57
Ce^{140}	2.07	2.13	2.68	1.65	1.57	0.59	0.75	0.91	2.44	2.31	2.50
Pr^{141}	0.27	0.28	0.33	0.23	0.20	0.08	0.10	0.12	0.32	0.32	0.29
Nd^{146}	1.01	1.13	1.43	0.98	0.91	0.34	0.40	0.60	1.59	1.50	1.47
Sm^{147}	0.31	0.28	0.33	0.26	0.26	0.07	0.09	0.17	0.42	0.40	0.39
Eu^{151}	0.09	0.11	0.08	0.09	0.08	0.03	0.03	0.05	0.12	0.11	0.11
Gd^{157}	0.41	0.49	0.42	0.43	0.42	0.15	0.21	0.31	0.63	0.65	0.61
Tb^{159}	0.07	0.09	0.07	0.06	0.06	0.03	0.03	0.04	0.10	0.11	0.09
Dy^{163}	0.52	0.52	0.43	0.47	0.38	0.17	0.22	0.30	0.68	0.77	0.50
Ho^{165}	0.11	0.12	0.11	0.11	0.07	0.04	0.05	0.09	0.16	0.18	0.13
Er^{167}	0.29	0.30	0.26	0.25	0.19	0.13	0.15	0.16	0.47	0.42	0.30
Tm^{169}	0.03	0.04	0.04	0.03	0.02	0.02	0.02	0.02	0.05	0.04	0.04
Yb^{173}	0.27	0.22	0.18	0.21	0.13	0.09	0.07	0.08	0.21	0.24	0.20

Lu^{175}	0.04	0.04	0.03	0.03	0.02	0.01	0.01	0.02	0.02	0.04	0.03
Pb^{204}											
Pb^{206}				0.05						0.12	
Pb^{207}									0.08	0.11	0.07
Pb^{208}									0.08	0.12	0.06
Th^{232}	0.01	0.01									
U^{238}	0.18	0.21	0.17	0.32	0.26	0.16	0.27	0.46	0.13	0.11	0.10

Table A14 (con't): LA-ICP-MS data for calcite from Ecton *Sample 1,* line traverse 1 (ppm)

	Sample 1										
	Cal 23	Cal 24	Cal 25	Cal 26	Cal 27	Cal 28	Cal 29	Cal 30	Cal 31	Cal 32	Cal 33
Mg^{25}	800	1000	970	1010	1010	1000	1000	990	1040	1040	1020
Si^{29}	3020	3050	2940	2940	2970	2890	2830	2760	2840	2880	2920
S^{34}	450	320	190	190	170	190	180	180	190	170	210
Mn^{55}	2050	1850	700	790	770	740	720	690	790	810	840
Fe^{57}	253	578	575	617	579	544	497	500	514	509	492
Co^{59}	0.14	0.20	0.15	0.15	0.16	0.15	0.13	0.14	0.14	0.15	0.14
Ni^{60}	0.14	0.19	0.16	0.16	0.34	0.19	0.19	0.23	0.22	0.14	0.13
Cu^{65}	0.19	0.80	0.25	0.15	1.82	0.18	0.17	0.21	0.16	0.16	0.19
Zn^{66}	0.11	0.23	0.11	0.07	0.38		0.08	0.41	0.07	0.07	0.08
Ge^{72}											
As^{75}	0.36	0.43	0.29	0.23	0.73	0.35	0.29	0.28	0.31	0.28	0.32
Sr^{88}	284	126	69	70	71	67	66	66	65	65	64
Y^{89}	7.1	4.0	0.2	0.3	0.7	0.3	0.3	0.3	0.3	0.3	0.3
Ag^{107}											
Ba^{137}	0.13	0.14									
La^{139}	1.36	3.43	0.01		0.10	0.01	0.01	0.00	0.00		0.01
Ce^{140}	2.32	7.79	0.02	0.02	0.26	0.02	0.02	0.02	0.02	0.02	0.01
Pr^{141}	0.29	1.05	0.00	0.01	0.04	0.00			0.00	0.01	

Nd^{146}	1.45	4.39	0.04		0.15	0.02	0.04	0.03	0.02	0.03	0.03
Sm^{147}	0.40	0.69			0.07	0.02					
Eu^{151}	0.12	0.17		0.01	0.01	0.01					
Gd^{157}	0.70	0.69		0.03	0.05	0.02		0.03	0.02		0.02
Tb^{159}	0.10	0.08	0.01	0.01	0.01	0.00			0.01	0.01	0.00
Dy^{163}	0.63	0.42	0.03	0.03	0.06	0.03	0.04	0.04	0.03	0.05	0.03
Ho^{165}	0.13	0.08		0.01	0.03	0.00	0.01	0.01	0.01	0.01	0.01
Er^{167}	0.35	0.22	0.02	0.04	0.07	0.03	0.03	0.02	0.02	0.02	0.01
Tm^{169}	0.03	0.02	0.01	0.00	0.01		0.00	0.00		0.00	
Yb^{173}	0.13	0.12		0.03	0.04	0.04	0.04		0.03	0.02	0.04
Lu^{175}	0.02	0.02			0.01	0.01			0.00	0.01	
Pb^{204}											
Pb^{206}	0.09										
Pb^{207}	0.04				0.05						
Pb^{208}	0.06										
Th^{232}		0.02									
U^{238}	0.13	0.07									

Table A14 (con't): LA-ICP-MS data for calcite from Ecton *Sample 1,* line traverse 1 (ppm)

	Sample 1										
	Cal 34	Cal 35	Cal 36	Cal 37	Cal 38	Cal 39	Cal 40	Cal 41	Cal 42	Cal 43	Cal 44
Mg^{25}	1030	1060	1070	1020	1020	1020	1020	1000	1010	1000	1020
Si^{29}	2820	2780	2870	2820	2760	2810	2830	2970	2860	2870	2880
S^{34}	190	180	190	200	180	180	190	210	190	180	180
Mn^{55}	900	980	990	770	770	760	760	760	760	760	760
Fe^{57}	475	462	464	450	446	450	447	446	442	442	448
Co^{59}	0.13	0.14	0.14	0.15	0.12	0.13	0.21	0.13	0.13	0.15	0.13
Ni^{60}	0.12	0.17	0.18	0.10	0.18	0.18	0.42	0.19	0.20	0.18	0.14
Cu^{65}	0.18	0.21	0.24	0.13	0.24	0.23	1.27	0.24	0.22	0.19	0.24

Zn^{66}		0.46	0.43	0.11	0.18	0.12	0.30	0.10	0.15	0.22	0.12
Ge^{72}				0.26	0.26	0.23	0.25	0.33	0.30	0.36	0.27
As^{75}	0.32	0.40	0.31	0.48	0.58	0.43	1.06	0.44	0.54	0.43	0.46
Sr^{88}	64	64	72	138	138	139	139	142	141	142	142
Y^{89}	0.3	0.4	5.6	44	45	45	45	45	45	45	45
Ag^{107}								0.01			
Ba^{137}							0.02				
La^{139}	0.01	0.02	2.1	17.1	17.4	17.2	17.4	17.5	17.4	17.5	17.5
Ce^{140}	0.01	0.07	5.0	40.6	40.6	40.5	40.5	41.1	40.9	41.1	41.2
Pr^{141}		0.02	0.7	5.9	5.9	6.0	5.9	6.0	6.0	6.0	6.1
Nd^{146}	0.02	0.06	3.1	24.7	24.3	25.0	24.6	24.9	25.1	25.0	25.3
Sm^{147}		0.05	0.8	6.1	6.2	6.4	6.1	6.3	6.3	6.2	6.1
Eu^{151}			0.2	1.5	1.6	1.6	1.6	1.6	1.6	1.6	1.6
Gd^{157}	0.03	0.06	0.9	6.7	6.9	7.0	6.8	7.2	6.9	7.1	6.9
Tb^{159}	0.01	0.01	0.1	1.0	1.0	1.0	1.0	1.0	1.0	1.0	1.0
Dy^{163}	0.03	0.07	0.7	5.7	5.6	5.4	5.5	5.9	5.9	5.8	5.7
Ho^{165}	0.01	0.02	0.1	1.1	1.1	1.1	1.2	1.2	1.1	1.1	1.1
Er^{167}	0.02	0.04	0.4	2.9	2.8	2.7	3.0	3.0	2.8	2.9	2.8
Tm^{169}		0.00	0.05	0.4	0.4	0.4	0.3	0.4	0.3	0.4	0.4
Yb^{173}		0.04	0.3	2.3	2.3	2.2	2.2	2.2	2.4	2.2	2.3
Lu^{175}		0.01	0.05	0.3	0.3	0.3	0.4	0.2	0.3	0.3	0.3
Pb^{204}											
Pb^{206}				0.06	0.05	0.10	0.07	0.06		0.06	0.08
Pb^{207}					0.06	0.08	0.06		0.10	0.06	
Pb^{208}				0.08	0.06	0.09	0.08	0.06	0.06	0.05	0.05
Th^{232}				0.01	0.02	0.02	0.02	0.03	0.03	0.02	0.03
U^{238}											

Table A14 (con't): LA-ICP-MS data for calcite from Ecton *Sample 1,* line traverse 1 (ppm)

	Sample 1								
	Cal 45	Cal 46	Cal 47	Cal 48	Cal 49	Cal 50	Cal 51	Cal 52	Cal 53
Mg^{25}	1030	1020	1020	1010	1010	1020	1000	980	1000
Si^{29}	2880	2750	2780	2720	2700	2730	2720	2720	2720
S^{34}	160	171	180	160	190	200	200	200	180
Mn^{55}	770	770	760	750	760	760	760	740	760
Fe^{57}	451	449	450	445	446	446	446	436	445
Co^{59}	0.14	0.15	0.16	0.15	0.13	0.15	0.15	0.15	0.14
Ni^{60}	0.16	0.15	0.21	0.19	0.19	0.13	0.11	0.17	0.15
Cu^{65}	0.22	0.22	0.28	0.15	0.17	0.21	0.19	0.15	0.18
Zn^{66}	0.09		0.22	0.12	0.13	0.19	0.12		
Ge^{72}	0.24	0.26	0.20	0.29	0.27	0.34	0.24	0.36	0.30
As^{75}	0.45	0.44	0.49	0.56	0.45	0.50	0.41	0.46	0.43
Sr^{88}	137	136	140	146	141	140	143	158	141
Y^{89}	44.2	44.3	44.9	45.9	45.3	44.9	45.3	46.2	44.7
Ag^{107}									
Ba^{137}				0.04	0.02			0.04	
La^{139}	17.0	17.1	17.5	17.9	17.6	17.5	17.5	17.9	17.0
Ce^{140}	40.2	39.7	40.1	42.2	41.7	41.2	41.2	42.3	40.9
Pr^{141}	5.8	5.9	6.0	6.2	5.9	6.0	6.1	6.3	6.0
Nd^{146}	24.1	23.9	24.8	25.0	25.0	25.2	25.1	25.9	24.9
Sm^{147}	6.1	6.1	6.3	6.6	6.2	6.2	6.3	6.4	6.3
Eu^{151}	1.5	1.6	1.6	1.7	1.6	1.6	1.6	1.7	1.6
Gd^{157}	7.0	6.9	6.9	7.1	7.1	7.1	7.0	7.3	6.9
Tb^{159}	1.0	1.0	1.0	1.0	1.0	1.0	1.0	1.0	1.0
Dy^{163}	5.7	5.5	5.7	6.0	5.7	5.8	5.8	5.9	5.6
Ho^{165}	1.1	1.1	1.1	1.1	1.1	1.1	1.1	1.1	1.1
Er^{167}	2.9	2.9	2.9	2.8	2.9	2.9	2.7	2.8	2.8
Tm^{169}	0.35	0.34	0.38	0.36	0.36	0.35	0.35	0.35	0.35
Yb^{173}	2.3	2.1	2.3	2.4	2.2	2.3	2.3	2.4	2.3

Lu^{175}	0.35	0.32	0.33	0.34	0.31	0.32	0.31	0.34	0.33
Pb^{204}									
Pb^{206}			0.05	0.09				0.07	
Pb^{207}		0.08	0.06	0.09	0.07	0.08	0.10	0.06	0.08
Pb^{208}	0.04	0.07	0.06	0.06	0.07	0.06	0.07	0.05	0.07
Th^{232}	0.02	0.02	0.02	0.02	0.02	0.02	0.02	0.02	0.02
U^{238}									

Table A14 (con't): LA-ICP-MS data for calcite from Ecton *Sample 1,* line traverse 1 (ppm)

	Sample 1							
	Cal 54	Cal 55	Cal 56	Cal 57	Cal 58	Cal 59	Cal 60	Cal 61
Mg^{25}	1000	1000	990	980	1000	970	940	940
Si^{29}	2670	2630	2580	2610	2630	2610	2630	2720
S^{34}	210	190	180	180	180	150	170	200
Mn^{55}	760	750	740	750	740	730	710	710
Fe^{57}	446	428	436	436	437	440	429	425
Co^{59}	0.13	0.15	0.13	0.14	0.15	0.14	0.16	0.13
Ni^{60}	0.17	0.13	0.16	0.14	0.17	0.14	0.18	0.18
Cu^{65}	0.15	0.16	0.24	0.20	0.15	0.13	0.17	0.12
Zn^{66}	0.11		0.16			0.09		0.07
Ge^{72}	0.24	0.30	0.28	0.27	0.29	0.29	0.28	0.26
As^{75}	0.44	0.54	0.49	0.42	0.45	0.49	0.55	0.50
Sr^{88}	139	142	150	146	146	161	172	173
Y^{89}	43.9	44.4	45.1	44.9	44.8	46.1	46.7	46.9
Ag^{107}						0.01		
Ba^{137}		0.05				0.05	0.02	
La^{139}	17.2	17.6	18.0	17.9	17.9	18.3	18.9	18.6
Ce^{140}	40.4	41.1	42.0	42.0	41.7	43.5	43.7	44.1
Pr^{141}	5.9	6.0	6.2	6.1	6.0	6.4	6.4	6.5

Nd^{146}	24.3	25.0	25.3	25.2	25.6	26.2	27.0	27.0
Sm^{147}	5.9	6.2	6.3	6.1	6.2	6.5	6.8	6.7
Eu^{151}	1.5	1.6	1.6	1.6	1.7	1.7	1.7	1.8
Gd^{157}	7.0	6.8	7.1	7.1	6.9	7.4	7.5	7.4
Tb^{159}	1.0	1.0	1.0	1.0	1.0	1.0	1.1	1.0
Dy^{163}	5.6	5.7	5.8	5.9	5.8	6.0	6.0	5.9
Ho^{165}	1.1	1.1	1.2	1.1	1.1	1.2	1.6	1.2
Er^{167}	2.7	2.7	2.9	3.0	2.8	2.9	2.8	2.9
Tm^{169}	0.3	0.4	0.3	0.4	0.4	0.4	0.4	0.3
Yb^{173}	2.1	2.2	2.2	2.2	2.3	2.3	2.4	2.3
Lu^{175}	0.3	0.3	0.3	0.3	0.3	0.3	0.3	0.3
Pb^{204}								
Pb^{206}		0.07	0.08	0.10	0.09	0.10	0.12	0.10
Pb^{207}	0.08	0.06	0.06	0.07	0.06	0.08	0.07	0.08
Pb^{208}	0.08	0.07	0.07	0.08	0.04	0.08	0.08	0.08
Th^{232}	0.02	0.03	0.02	0.02	0.02	0.02	0.02	0.02
U^{238}								

Table A15 (con't): LA-ICP-MS data for calcite from Ecton *Sample 1,* line traverse 2 (ppm)

	Sample 1										
	Cal 1	Cal 2	Cal 3	Cal 4	Cal 5	Cal 6	Cal 7	Cal 8	Cal 9	Cal 10	Cal 11
Mg^{25}	880	1050	900	910	1140	1290	1310	1090	1050	940	850
Si^{29}	2200	2200	2260	2160	2170	2100	2050	2090	2130	2190	2000
S^{34}	180	170	160	180	180	200	210	230	230	260	200
Mn^{55}	780	820	880	870	940	950	1040	920	930	790	830
Fe^{57}	174	172	173	173	173	174	174	172	174	174	176
Co^{59}	0.14	0.14	0.14	0.13	0.14	0.12	0.14	0.13	0.13	0.14	0.15
Ni^{60}	0.14	0.19	0.18	0.21	0.16	0.12	0.11	0.16	0.28	0.43	0.46
Cu^{65}	0.16	0.19	0.20	0.21	0.16	0.11	0.17	0.17	0.36	0.65	0.67

Zn^{66}	0.07	0.16	0.41	0.36	0.36	0.12	0.15	0.47	0.95	1.84	1.68
Ge^{72}											
As^{75}	0.25	0.33	0.24	0.21	0.29	0.29	0.27	0.23	0.24	0.36	0.28
Sr^{88}	405	279	261	341	125	108	98	129	96	121	118
Y^{89}	4.1	3.9	2.7	3.8	6.2	8.5	6.8	9.4	8.0	9.9	11.1
Ag^{107}											
Ba^{137}	0.02		0.03					0.03		0.07	0.03
La^{139}	0.48	0.38	0.17	0.27	0.61	1.32	1.07	1.58	1.67	2.26	2.47
Ce^{140}	1.10	0.93	0.40	0.63	1.45	2.76	2.22	3.13	3.60	4.60	5.48
Pr^{141}	0.17	0.15	0.08	0.11	0.20	0.37	0.30	0.40	0.47	0.60	0.73
Nd^{146}	0.71	0.64	0.42	0.56	0.87	1.64	1.22	1.67	1.88	2.42	2.94
Sm^{147}	0.20	0.21	0.14	0.18	0.28	0.55	0.35	0.53	0.52	0.73	0.83
Eu^{151}	0.08	0.07	0.03	0.06	0.10	0.14	0.10	0.17	0.16	0.18	0.24
Gd^{157}	0.37	0.31	0.21	0.28	0.54	0.66	0.58	0.73	0.75	0.82	1.08
Tb^{159}	0.05	0.05	0.04	0.05	0.10	0.13	0.09	0.13	0.13	0.15	0.22
Dy^{163}	0.41	0.39	0.23	0.35	0.65	0.90	0.70	1.04	0.90	1.09	1.27
Ho^{165}	0.08	0.08	0.05	0.08	0.16	0.19	0.17	0.23	0.18	0.23	0.27
Er^{167}	0.22	0.24	0.17	0.23	0.40	0.56	0.50	0.64	0.59	0.67	0.73
Tm^{169}	0.03	0.03	0.02	0.03	0.05	0.07	0.07	0.08	0.08	0.08	0.09
Yb^{173}	0.19	0.20	0.13	0.17	0.34	0.49	0.37	0.59	0.58	0.64	0.65
Lu^{175}	0.03	0.03	0.01	0.02	0.05	0.06	0.06	0.08	0.09	0.09	0.08
Pb^{204}											
Pb^{206}	0.46	0.51	0.68	0.39	0.10	0.14	0.14	0.10	0.25	0.21	0.28
Pb^{207}			0.05								
Pb^{208}											
Th^{232}			0.01				0.03	0.02	0.08	0.06	0.02
U^{238}	27.2	24.8	34.6	21.7	6.2	5.4	6.4	4.1	10.2	10.8	11.6

Table A15 (con't): LA-ICP-MS data for calcite from Ecton *Sample 1,* line traverse 2 (ppm)

	Sample 1										
	Cal 12	Cal 13	Cal 14	Cal 15	Cal 16	Cal 17	Cal 18	Cal 19	Cal 20	Cal 21	Cal 22
Mg^{25}	890	850	1000	740	760	930	890	1160	1120	1040	1070
Si^{29}	2170	2130	2080	2140	2140	2130	2270	2230	2180	2140	2070
S^{34}	230	210	220	270	270	250	260	200	230	250	260
Mn^{55}	1090	1140	1390	1150	1230	1450	1560	2340	2410	2490	2560
Fe^{57}	173	175	174	173	174	176	173	173	174	173	172
Co^{59}	0.14	0.14	0.14	0.13	0.13	0.15	0.12	0.12	0.13	0.12	0.14
Ni^{60}	0.15	0.12	0.17	0.17	0.15	0.13	0.10	0.14	0.15	0.20	0.18
Cu^{65}	0.15	0.18	0.14	0.16	0.16	0.16	0.22	0.16	0.18	0.22	0.20
Zn^{66}	0.11		0.11		0.17		0.15	0.10	0.33	0.47	0.20
Ge^{72}											
As^{75}	0.25	0.25	0.36	0.18	0.25	0.31	0.25	0.32	0.31	0.23	0.26
Sr^{88}	144	137	151	220	220	174	176	112	118	106	132
Y^{89}	10.2	8.0	6.1	8.4	6.9	5.6	6.3	3.7	4.8	4.8	5.1
Ag^{107}											
Ba^{137}		0.05	0.02	0.07	0.06	0.04	0.04		0.02		0.02
La^{139}	1.95	1.72	1.20	1.69	1.21	1.07	1.02	0.46	0.93	1.71	1.23
Ce^{140}	4.34	3.67	2.46	3.34	2.42	2.16	2.04	0.82	1.50	2.31	1.85
Pr^{141}	0.60	0.48	0.33	0.45	0.35	0.30	0.27	0.11	0.19	0.27	0.27
Nd^{146}	2.32	1.83	1.37	1.70	1.33	1.26	1.21	0.46	0.88	1.10	1.01
Sm^{147}	0.68	0.55	0.37	0.51	0.37	0.32	0.32	0.18	0.24	0.23	0.25
Eu^{151}	0.19	0.14	0.09	0.18	0.12	0.11	0.09	0.05	0.07	0.09	0.08
Gd^{157}	0.90	0.75	0.56	0.68	0.55	0.52	0.51	0.26	0.38	0.48	0.37
Tb^{159}	0.15	0.12	0.10	0.12	0.10	0.08	0.09	0.05	0.07	0.06	0.07
Dy^{163}	1.07	0.82	0.58	0.82	0.70	0.54	0.67	0.34	0.44	0.41	0.48
Ho^{165}	0.23	0.21	0.14	0.18	0.16	0.13	0.13	0.08	0.10	0.10	0.10
Er^{167}	0.67	0.58	0.37	0.49	0.35	0.33	0.43	0.24	0.28	0.28	0.29
Tm^{169}	0.09	0.07	0.05	0.07	0.07	0.06	0.05	0.03	0.04	0.04	0.04
Yb^{173}	0.59	0.49	0.30	0.44	0.39	0.39	0.34	0.18	0.24	0.27	0.21
Lu^{175}	0.09	0.07	0.05	0.07	0.05	0.05	0.05	0.02	0.03	0.04	0.03

Pb^{204}											
Pb^{206}	0.18	0.19			0.07			0.04			
Pb^{207}											
Pb^{208}											
Th^{232}	0.02	0.06	0.02	0.01	0.01	0.03	0.02		0.01	0.01	0.01
U^{238}	7.0	8.8	1.3	1.6	1.6	1.6	0.8	0.4	0.3	0.2	0.2

Table A15 (con't): LA-ICP-MS data for calcite from Ecton *Sample 1,* line traverse 2 (ppm)

	Sample 1										
	Cal 23	Cal 24	Cal 25	Cal 26	Cal 27	Cal 28	Cal 29	Cal 30	Cal 31	Cal 32	Cal 33
Mg^{25}	1070	1070	1070	1020	960	860	870	1350	680	550	570
Si^{29}	2150	2140	2100	2080	2050	2110	2140	2130	2220	2100	2130
S^{34}	270	280	260	270	281	330	360	380	470	460	480
Mn^{55}	2680	2880	2680	2490	2350	2180	2430	3320	2150	1780	1610
Fe^{57}	172	173	203	230	183	235	183	206	289	304	548
Co^{59}	0.13	0.13	0.11	0.12	0.13	0.12	0.12	0.14	0.17	0.14	0.13
Ni^{60}	0.18	0.17	0.15	0.17	0.10	0.17	0.13	0.35	0.51	0.25	0.25
Cu^{65}	0.21	0.23	0.21	0.17	0.19	0.16	0.18	0.78	1.32	0.48	0.63
Zn^{66}	0.28	0.53	0.12		0.07	0.08	0.07	2.37	3.02	0.77	1.00
Ge^{72}											
As^{75}	0.27	0.33	0.32	0.32	0.29	0.31	0.27	0.27	0.25	0.24	0.26
Sr^{88}	130	134	121	82	151	163	189	143	310	331	324
Y^{89}	4.9	4.6	4.0	3.1	3.5	3.9	3.3	2.5	6.1	8.0	9.7
Ag^{107}				0.01							
Ba^{137}		0.05	0.03		0.02	0.05		0.16	0.32	0.20	0.18
La^{139}	1.57	1.82	1.89	2.31	1.50	1.67	0.96	0.66	0.88	1.00	1.23
Ce^{140}	2.37	2.65	2.54	3.17	2.16	2.18	1.45	0.88	1.46	1.88	2.45
Pr^{141}	0.27	0.32	0.29	0.34	0.25	0.25	0.17	0.10	0.20	0.23	0.32
Nd^{146}	1.17	1.36	1.29	1.51	1.05	1.07	0.81	0.49	0.92	1.06	1.55

Sm^{147}	0.26	0.33	0.27	0.31	0.27	0.23	0.20	0.08	0.19	0.36	0.37
Eu^{151}	0.08	0.07	0.07	0.07	0.06	0.06	0.04	0.04	0.09	0.11	0.12
Gd^{157}	0.48	0.46	0.47	0.34	0.36	0.42	0.25	0.22	0.51	0.62	0.75
Tb^{159}	0.07	0.07	0.06	0.06	0.05	0.05	0.04	0.02	0.07	0.09	0.12
Dy^{163}	0.47	0.44	0.35	0.30	0.34	0.29	0.30	0.20	0.42	0.71	0.81
Ho^{165}	0.11	0.10	0.08	0.07	0.08	0.08	0.06	0.04	0.11	0.14	0.17
Er^{167}	0.33	0.27	0.23	0.18	0.16	0.15	0.17	0.11	0.27	0.36	0.45
Tm^{169}	0.03	0.03	0.03	0.02	0.02	0.02	0.02	0.01	0.03	0.04	0.05
Yb^{173}	0.22	0.22	0.17	0.13	0.12	0.10	0.09	0.07	0.14	0.20	0.28
Lu^{175}	0.04	0.04	0.03	0.02	0.02	0.02	0.01	0.01	0.01	0.02	0.04
Pb^{204}											
Pb^{206}								0.05	0.12	0.06	0.15
Pb^{207}									0.08	0.06	0.10
Pb^{208}								0.03	0.11	0.07	0.15
Th^{232}	0.01	0.01		0.00							
U^{238}	0.2	0.1	0.2	0.1	0.2	0.3	0.6	0.2	0.1	0.1	0.1

Table A15 (con't): LA-ICP-MS data for calcite from Ecton *Sample 1,* line traverse 2 (ppm)

	Sample 1										
	Cal 34	Cal 35	Cal 36	Cal 37	Cal 38	Cal 39	Cal 40	Cal 41	Cal 42	Cal 43	Cal 44
Mg^{25}	760	1150	980	1180	1030	1090	1140	1230	1010	1010	1010
Si^{29}	2060	1960	2120	2150	2200	2140	2070	2090	2090	2140	2090
S^{34}	440	440	150	150	170	160	170	180	160	170	150
Mn^{55}	2320	2890	1400	1560	700	670	800	830	790	790	750
Fe^{57}	493	273	1066	764	590	635	660	684	642	624	605
Co^{59}	0.15	0.13	0.14	0.13	0.12	0.13	0.13	0.13	0.12	0.12	0.12
Ni^{60}	0.31	0.20	0.17	0.24	0.18	0.12	0.30	0.22	0.17	0.19	0.16
Cu^{65}	0.72	0.44	0.15	0.30	0.19	0.15	1.35	1.02	0.16	0.49	0.14
Zn^{66}	1.21	0.48	0.16	0.33	0.11		1.70	0.89		0.50	0.06

Ge^{72}											
As^{75}	0.21	0.32	0.25	0.28	0.28	0.32	0.33	0.29	0.29	0.19	0.23
Sr^{88}	205	131	63	57	69	69	67	69	67	67	64
Y^{89}	6.3	5.8	0.6	0.4	0.2	0.2	0.3	0.4	0.3	0.3	0.3
Ag^{107}		0.01									
Ba^{137}	0.07	0.03			0.02		0.05			0.03	
La^{139}	3.40	5.38	0.02	0.06			0.01	0.02	0.01	0.01	0.01
Ce^{140}	5.07	7.61	0.07	0.17	0.01	0.02	0.03	0.05	0.02	0.03	0.03
Pr^{141}	0.63	0.89	0.01	0.02	0.00	0.00	0.00	0.01	0.01	0.01	0.00
Nd^{146}	2.91	3.96	0.07	0.09			0.03	0.04	0.03	0.02	0.02
Sm^{147}	0.54	0.73	0.03	0.04							0.02
Eu^{151}	0.14	0.18	0.01			0.01	0.01	0.01		0.01	0.01
Gd^{157}	0.73	0.97	0.04	0.02	0.02		0.05	0.06			0.03
Tb^{159}	0.10	0.10	0.01	0.00		0.00		0.01		0.01	
Dy^{163}	0.52	0.50	0.06	0.05	0.02	0.03	0.04	0.05	0.04	0.05	0.06
Ho^{165}	0.11	0.10	0.02	0.01	0.01	0.01	0.01	0.01	0.01	0.01	0.01
Er^{167}	0.31	0.26	0.05			0.02	0.04	0.06	0.04	0.03	0.04
Tm^{169}	0.04	0.03	0.01		0.00	0.00	0.01	0.01	0.01	0.01	0.00
Yb^{173}	0.16	0.11	0.04				0.04	0.04	0.03	0.02	0.05
Lu^{175}	0.03	0.02	0.01	0.00	0.01		0.01	0.01		0.00	
Pb^{204}											
Pb^{206}	0.06			0.05						0.04	
Pb^{207}	0.07										
Pb^{208}	0.09		0.03	0.03			0.03				
Th^{232}		0.01									
U^{238}	0.1	0.0									

Table A15 (con't): LA-ICP-MS data for calcite from Ecton *Sample 1,* line traverse 2 (ppm)

	Sample 1										
	Cal 45	Cal 46	Cal 47	Cal 48	Cal 49	Cal 50	Cal 51	Cal 52	Cal 53	Cal 54	Cal 55
Mg^{25}	1030	1070	1110	1100	1040	1040	1000	1030	1050	1030	1050
Si^{29}	2020	2040	2070	2130	2140	2120	2050	2060	2040	2040	1980
S^{34}	150	150	120	190	170	170	160	150	170	170	140
Mn^{55}	750	790	790	800	800	800	760	680	790	770	750
Fe^{57}	603	608	630	604	598	608	599	565	524	527	517
Co^{59}	0.13	0.13	0.14	0.12	0.13	0.10	0.11	0.14	0.11	0.11	0.12
Ni^{60}	0.14	0.17	0.14	0.15	0.12	0.14	0.16	0.15	0.16	0.13	0.12
Cu^{65}	0.13	0.14	0.28	0.36	0.19	0.24	0.41	0.38	0.20	0.28	0.17
Zn^{66}			0.24	0.76	0.11	0.15	0.33	0.31	0.21	0.32	0.08
Ge^{72}											
As^{75}	0.26	0.27	0.21	0.28	0.27	0.27	0.29	0.27	0.24	0.33	0.24
Sr^{88}	64	65	67	67	65	63	63	63	62	63	62
Y^{89}	0.4	0.3	0.3	0.3	0.3	0.5	0.3	0.4	0.3	0.3	0.3
Ag^{107}											
Ba^{137}											
La^{139}	0.02	0.01	0.01	0.01	0.02	0.41	0.01	0.03	0.01	0.01	0.01
Ce^{140}	0.04	0.03	0.03	0.02	0.04	0.69	0.04	0.05	0.03	0.03	0.02
Pr^{141}	0.01	0.01	0.00	0.00	0.01	0.11	0.01	0.01	0.01	0.01	0.01
Nd^{146}	0.05			0.03	0.04	0.39	0.03	0.07	0.04	0.02	0.03
Sm^{147}			0.02	0.03	0.03	0.08	0.02		0.02	0.03	
Eu^{151}	0.01	0.01		0.01		0.02		0.00	0.01		
Gd^{157}	0.04	0.02	0.03			0.07		0.04	0.03		
Tb^{159}	0.01	0.00	0.01	0.01	0.01	0.01	0.01	0.01	0.01	0.00	0.00
Dy^{163}	0.06	0.04	0.02	0.06	0.03	0.07	0.04	0.05	0.03	0.01	0.03
Ho^{165}	0.01	0.01	0.01	0.01	0.01	0.01	0.01	0.01	0.01	0.01	0.01
Er^{167}	0.03	0.04	0.02	0.03	0.04	0.06	0.02	0.03	0.04	0.02	0.01
Tm^{169}	0.01	0.01		0.01	0.01	0.01	0.01			0.00	0.00
Yb^{173}		0.03	0.03	0.04	0.03	0.05	0.03	0.03	0.03		

Lu^{175}	0.01	0.01			0.01	0.01	0.01	0.01	0.00	0.00
Pb^{204}										
Pb^{206}										
Pb^{207}							0.03			
Pb^{208}				0.06			0.03			
Th^{232}										0.01
U^{238}										

Table A15 (con't): LA-ICP-MS data for calcite from Ecton *Sample 1,* line traverse 2 (ppm)

	Sample 1									
	Cal 56	Cal 57	Cal 58	Cal 59	Cal 60	Cal 61	Cal 62	Cal 63	Cal 64	Cal 65
Mg^{25}	1050	1070	1070	1060	1060	1070	1080	1100	1110	1010
Si^{29}	1990	2010	2150	2100	1950	2040	2060	2060	2010	2080
S^{34}	150	150	180	150	140	140	150	150	150	140
Mn^{55}	730	760	760	740	770	760	760	710	700	660
Fe^{57}	519	505	521	525	545	546	543	537	538	518
Co^{59}	0.13	0.12	0.11	0.13	0.13	0.12	0.12	0.13	0.13	0.13
Ni^{60}	0.11	0.12	0.19	0.17	0.20	0.15	0.16	0.10	0.13	0.15
Cu^{65}	0.15	0.18	0.21	0.17	0.40	0.12	0.12	0.16	0.19	0.15
Zn^{66}	0.07	0.07			0.34		0.07	0.06	0.09	
Ge^{72}										
As^{75}	0.26	0.27	0.25	0.31	0.25	0.25	0.20	0.29	0.18	0.21
Sr^{88}	64	62	63	63	63	64	63	61	62	63
Y^{89}	0.3	0.3	0.3	0.3	0.4	0.4	0.4	0.4	0.4	0.4
Ag^{107}										
Ba^{137}					0.13					0.00
La^{139}	0.01	0.01	0.01	0.01	0.01	0.01	0.01	0.02	0.02	0.01
Ce^{140}	0.03	0.04	0.04	0.03	0.04	0.05	0.04	0.06	0.05	0.04
Pr^{141}	0.00	0.01	0.01	0.01	0.01	0.01	0.01	0.01	0.01	0.01

Nd^{146}	0.04	0.04	0.03		0.03	0.04	0.06	0.06	0.07	0.04
Sm^{147}					0.04			0.02	0.03	
Eu^{151}		0.00	0.01	0.00	0.00	0.01	0.01		0.01	0.01
Gd^{157}		0.03	0.03	0.02	0.03	0.04	0.03	0.05	0.05	0.03
Tb^{159}		0.01	0.01	0.01	0.01		0.01	0.01	0.01	0.01
Dy^{163}	0.05	0.04	0.05	0.03	0.04	0.03	0.05	0.05	0.06	0.05
Ho^{165}	0.01	0.01	0.01	0.01	0.01	0.01	0.01	0.01	0.02	0.01
Er^{167}	0.02	0.03	0.04	0.03	0.04	0.02	0.04	0.04	0.03	0.03
Tm^{169}			0.01		0.00	0.01	0.00	0.01	0.01	0.00
Yb^{173}	0.03			0.03		0.04		0.04	0.03	0.05
Lu^{175}	0.01	0.01	0.00	0.01		0.01	0.01	0.01	0.01	0.01
Pb^{204}										
Pb^{206}										
Pb^{207}										
Pb^{208}										
Th^{232}										
U^{238}										

Table A16: LA-ICP-MS data for calcite from Ecton *Sample 2,* line traverse 1 (ppm)

	Sample 2										
	Cal 1	Cal 2	Cal 3	Cal 4	Cal 5	Cal 6	Cal 7	Cal 8	Cal 9	Cal 10	Cal 11
Mg^{25}	820	2030	1210	920	850	800	820	810	890	950	1440
Si^{29}	2620	2600	2610	2580	2500	2400	2500	2480	2450	2450	2430
S^{34}	3370	180	170	160	180	180	170	160	160	190	210
Mn^{55}	1040	2620	1250	770	680	710	660	660	690	760	1090
Fe^{57}	400	300	670	580	600	550	540	550	550	520	550
Co^{59}	0.34	0.15	0.14	0.13	0.17	0.18	0.16	0.19	0.17	0.21	0.12
Ni^{60}	1.06	0.16	0.15	0.16	0.33	0.34	0.22	0.26	0.15	0.41	0.16
Cu^{65}	1000	0.45	0.34	0.21	0.54	0.49	0.45	1.22	0.25	1.33	0.32

Zn^{66}	200	0.20	0.16	0.20	3.12	8.71	8.26	15.93	0.53	0.45	0.18
Ge^{72}	2.90										
As^{75}	0.97	0.23	0.24	0.30	0.31	0.29	0.32	0.39	0.33	0.75	0.32
Sr^{88}	281	70	60	61	65	57	67	64	61	58	62
Y^{89}	0.3	1.0	0.4	0.2	0.1	0.2	5.3	10.0	9.0	0.1	0.2
Ag^{107}	0.05										
Ba^{137}	0.04						0.02				
La^{139}	0.05	0.10	0.10	0.01		0.01	0.71	1.22	1.81	0.01	0.01
Ce^{140}	0.09	0.15	0.16	0.01	0.01	0.02	1.95	3.58	4.41	0.04	0.02
Pr^{141}	0.01	0.02	0.02			0.00	0.30	0.58	0.68	0.00	0.01
Nd^{146}	0.06	0.11	0.11	0.02		0.03	1.38	2.78	3.14		0.02
Sm^{147}		0.04	0.03				0.47	0.81	0.91	0.02	
Eu^{151}		0.01	0.01				0.11	0.22	0.22		
Gd^{157}	0.01	0.06	0.05			0.02	0.64	1.18	0.97		
Tb^{159}		0.01	0.00	0.00		0.01	0.10	0.19	0.17		0.00
Dy^{163}	0.02	0.10	0.05	0.03	0.02	0.03	0.61	1.28	1.13		0.02
Ho^{165}	0.01	0.02	0.01	0.01	0.00	0.01	0.14	0.25	0.22	0.00	0.01
Er^{167}	0.02	0.06	0.03	0.01			0.49	0.78	0.65	0.01	0.03
Tm^{169}	0.00	0.01	0.00		0.00		0.06	0.12	0.09		
Yb^{173}	0.03	0.05	0.03	0.04	0.02	0.03	0.55	0.96	0.68		
Lu^{175}	0.01	0.01	0.00	0.00	0.01		0.08	0.15	0.11		0.01
Pb^{204}	8										
Pb^{206}	8				0.08	0.10	0.06	0.11	0.05		
Pb^{207}	7		0.09		0.08	0.08	0.05	0.11			
Pb^{208}	7				0.09	0.10	0.06	0.10	0.03		
Th^{232}	0.01						0.00		0.01	0.00	
U^{238}	0.88	0.03	0.01		0.01	0.02	0.01	0.01	0.01		

Table A15 (con't): LA-ICP-MS data for calcite from Ecton *Sample 2,* line traverse 1 (ppm)

Sample 2

	Cal 12	Cal 13	Cal 14	Cal 15	Cal 16	Cal 17	Cal 18	Cal 19	Cal 20	Cal 21	Cal 22
Mg^{25}	1680	1690	1890	1790	1740	1460	1390	1390	1510	1450	1540
Si^{29}	2510	2430	2430	2430	2470	2370	2360	2380	2470	2360	2390
S^{34}	190	170	150	180	160	160	180	170	190	170	160
Mn^{55}	1240	1280	1380	1360	1220	950	910	910	1030	970	1000
Fe^{57}	530	540	550	540	520	460	450	440	470	470	470
Co^{59}	0.13	0.13	0.14	0.14	0.17	0.13	0.13	0.15	0.13	0.13	0.14
Ni^{60}	0.19	0.16	0.15	0.14	0.19	0.13	0.19	0.17	0.14	0.18	0.16
Cu^{65}	0.19	0.38	0.31	0.22	0.97	0.22	0.25	0.19	0.27	0.27	0.23
Zn^{66}	0.12	0.38	0.23		0.26	0.34	0.44	0.14	0.11	0.11	0.13
Ge^{72}											
As^{75}	0.22	0.35	0.34	0.31	0.49	0.34	0.25	0.27	0.26	0.24	0.34
Sr^{88}	64	58	61	59	66	70	69	69	70	70	69
Y^{89}	0.3	0.2	0.2	0.2	1.3	3.1	3.4	3.4	2.8	3.3	3.5
Ag^{107}											
Ba^{137}									0.02		0.02
La^{139}	0.02	0.01	0.00	0.00	0.03	0.04	0.03	0.04	0.08	0.04	0.03
Ce^{140}	0.04	0.02	0.01	0.02	0.05	0.08	0.09	0.11	0.15	0.10	0.10
Pr^{141}	0.01	0.00		0.00	0.02	0.02	0.03	0.02	0.04	0.02	0.03
Nd^{146}	0.05				0.06	0.10	0.10	0.15	0.18	0.18	0.15
Sm^{147}		0.01					0.06	0.06	0.04	0.07	0.07
Eu^{151}	0.00		0.01			0.01	0.02	0.02	0.02	0.03	0.01
Gd^{157}					0.06	0.13	0.14	0.14	0.13	0.16	0.17
Tb^{159}					0.01	0.04	0.04	0.04	0.03	0.04	0.04
Dy^{163}	0.02	0.03	0.02		0.15	0.32	0.28	0.30	0.28	0.30	0.28
Ho^{165}	0.01	0.01		0.01	0.04	0.08	0.09	0.11	0.08	0.08	0.10
Er^{167}	0.02	0.02		0.03	0.11	0.31	0.29	0.30	0.24	0.28	0.30
Tm^{169}	0.01			0.00	0.02	0.04	0.04	0.05	0.04	0.05	0.05
Yb^{173}		0.03		0.02	0.15	0.27	0.28	0.30	0.29	0.28	0.34
Lu^{175}	0.00		0.00		0.02	0.05	0.05	0.04	0.04	0.04	0.04

Pb^{204}											
Pb^{206}											
Pb^{207}						0.03	0.04		0.05		
Pb^{208}	0.03	0.02	0.03	0.04		0.04	0.04	0.03			
Th^{232}							0.01		0.00		
U^{238}	0.00										

Table A15 (con't): LA-ICP-MS data for calcite from Ecton *Sample 2,* line traverse 1 (ppm)

	Sample 2										
	Cal 23	Cal 24	Cal 25	Cal 26	Cal 27	Cal 28	Cal 29	Cal 30	Cal 31	Cal 32	Cal 33
Mg^{25}	1570	1520	1510	1590	1530	1410	1890	1870	1860	1890	1890
Si^{29}	2370	2390	2290	2320	2240	2280	2310	2300	2280	2290	2200
S^{34}	170	170	180	160	160	160	170	190	200	170	170
Mn^{55}	1020	1000	1000	1070	1000	900	1340	1390	1350	1340	1340
Fe^{57}	470	480	470	490	480	450	560	570	570	570	570
Co^{59}	0.14	0.13	0.15	0.14	0.20	0.12	0.15	0.13	0.14	0.12	0.14
Ni^{60}	0.14	0.15	0.14	0.13	0.26	0.16	0.15	0.13	0.15	0.17	0.18
Cu^{65}	0.27	0.23	0.30	0.23	1.02	0.17	0.48	0.19	0.24	0.22	0.29
Zn^{66}	0.20	0.17	0.28	0.23	0.36	0.12	0.25	0.27	0.11	0.33	0.18
Ge^{72}											
As^{75}	0.23	0.24	0.27	0.22	0.50	0.27	0.31	0.33	0.25	0.36	0.25
Sr^{88}	70	69	70	71	72	72	67	67	68	72	73
Y^{89}	3.4	3.2	3.0	2.5	2.9	3.4	0.7	0.3	0.4	0.4	0.4
Ag^{107}				0.00							
Ba^{137}			0.02		0.02		0.04				
La^{139}	0.07	0.03	0.03	0.04	0.05	0.04	0.03	0.02	0.01	0.01	0.01
Ce^{140}	0.16	0.09	0.09	0.08	0.12	0.12	0.06	0.04	0.03	0.03	0.03
Pr^{141}	0.03	0.02	0.02	0.02	0.02	0.03	0.01	0.01	0.01	0.01	0.01
Nd^{146}	0.17	0.11	0.10	0.12	0.11	0.15	0.04	0.04	0.02	0.04	0.03

Sm^{147}	0.07	0.07	0.05	0.07	0.07	0.10			0.03		0.02
Eu^{151}	0.02	0.02	0.02	0.02	0.01	0.02	0.01				
Gd^{157}	0.15	0.11	0.14	0.07	0.13	0.14	0.04		0.03		
Tb^{159}	0.03	0.04	0.04	0.02	0.03	0.04	0.01	0.00	0.00	0.00	
Dy^{163}	0.32	0.27	0.30	0.23	0.26	0.32	0.07	0.05	0.04	0.04	0.03
Ho^{165}	0.09	0.08	0.08	0.05	0.07	0.08	0.02	0.01	0.02	0.01	0.01
Er^{167}	0.27	0.31	0.27	0.22	0.25	0.28	0.06	0.04	0.03	0.04	0.03
Tm^{169}	0.05	0.04	0.04	0.04	0.04	0.05	0.01	0.00	0.01	0.01	0.01
Yb^{173}	0.26	0.26	0.27	0.27	0.26	0.28	0.10	0.04	0.03		0.06
Lu^{175}	0.05	0.05	0.05	0.05	0.04	0.04	0.01	0.00	0.01	0.00	0.01
Pb^{204}											
Pb^{206}											
Pb^{207}				0.06	0.05						
Pb^{208}					0.03					0.03	
Th^{232}		0.00	0.00								
U^{238}											

Table A15 (con't): LA-ICP-MS data for calcite from Ecton *Sample 2,* line traverse 1 (ppm)

	Sample 2								
	Cal 34	Cal 35	Cal 36	Cal 37	Cal 38	Cal 39	Cal 40	Cal 41	Cal 42
Mg^{25}	1880	1860	1860	1910	1920	1890	1900	1800	1820
Si^{29}	2220	2220	2230	2210	2200	2170	2280	2200	2270
S^{34}	150	150	180	160	160	160	170	170	180
Mn^{55}	1320	1310	1290	1350	1350	1330	1350	1350	1330
Fe^{57}	560	560	550	570	570	570	570	570	560
Co^{59}	0.14	0.15	0.16	0.13	0.13	0.14	0.14	0.14	0.14
Ni^{60}	0.15	0.16	0.11	0.13	0.13	0.22	0.18	0.16	0.18
Cu^{65}	0.19	0.17	0.21	0.22	0.22	0.18	0.21	0.17	0.22
Zn^{66}	0.19	0.09	0.15		0.27	0.63	0.26	0.16	0.10

Ge^{72}									
As^{75}	0.30	0.26	0.28	0.20	0.21	0.30	0.32	0.28	0.23
Sr^{88}	75	75	75	72	73	72	72	69	71
Y^{89}	0.4	0.5	0.5	0.4	0.3	0.4	0.3	0.3	0.3
Ag^{107}	0.01								
Ba^{137}			0.00						
La^{139}	0.04	0.01	0.03	0.01	0.01	0.01	0.01	0.01	0.02
Ce^{140}	0.08	0.04	0.07	0.03	0.03	0.04	0.02	0.02	0.03
Pr^{141}	0.02	0.01	0.01	0.01	0.01	0.01	0.01	0.00	0.01
Nd^{146}	0.09	0.07	0.07	0.04	0.04	0.03		0.01	0.04
Sm^{147}	0.02		0.01	0.03	0.01				
Eu^{151}			0.01	0.01					0.00
Gd^{157}	0.04	0.02		0.02	0.02	0.04		0.02	0.02
Tb^{159}	0.00	0.01	0.01	0.01	0.01	0.00		0.00	0.00
Dy^{163}	0.05	0.05	0.06	0.02	0.04	0.02	0.04	0.05	0.04
Ho^{165}	0.01	0.01	0.02	0.01	0.01	0.01	0.01	0.01	0.01
Er^{167}	0.03	0.04	0.05	0.06	0.03	0.04	0.04	0.01	0.02
Tm^{169}	0.00	0.01	0.01	0.00	0.01	0.01	0.01	0.00	0.01
Yb^{173}	0.04	0.04	0.06	0.07	0.04	0.03	0.04	0.04	0.05
Lu^{175}		0.01	0.01	0.01	0.01	0.01	0.01	0.01	0.01
Pb^{204}									
Pb^{206}					0.04			0.05	
Pb^{207}						0.05			
Pb^{208}									
Th^{232}									0.00
U^{238}									